Validation of Point and Pressure Loading Models for Simply Supported Composite Sandwich Beams

by

Bryan K Wright

A thesis submitted in conformity with the requirements
for the degree of Masters of Applied Science
Graduate Department of Aerospace Engineering
University of Toronto

© Copyright 2012 by Bryan K Wright

Abstract

Validation of Point and Pressure Loading Models for Simply Supported Composite Sandwich Beams

Bryan K Wright
Masters of Applied Science
Graduate Department of Aerospace Engineering
University of Toronto
2012

Stiffness and strength models are derived for simply supported composite sandwich panels comprised of fibre-reinforced face sheets and polymer cores subject to symmetric four point bending and uniformly distributed loading. Optimal trajectories for minimum mass design are calculated using the models and situated on failure mechanism maps. A stiffness constraint is also derived to omit beam designs of excessive compliance. Analytical models are validated through an extensive series of experiments, considering beams comprised of GFRP face sheets with ROHACELL 51-IG and extruded polystyrene (EPS) polymer cores. An alternate loading fixture is used to simulate uniform pressure loads. In general, experiments are able to validate most analytical expressions for a range of experimental conditions. Though the predictions worked well with most beam cases, analytical models were noted to become unreliable for short or slender beams.

Acknowledgements

I first wish to express my esteemed gratitude to my thesis advisor Dr. Craig A. Steeves, for his support and guidance throughout the duration of this master's project. It was a privilege to work with him and I wish him the best in his future pursuits. I also with to thank my RAC Advisors, Dr. David W. Zingg, Dr. Philippe Lavoie, Dr. Prasanth B. Nair and Dr. Alis Ekmekci for their constructive feedback during the following project, and my second reader, Dr. Adam Steinberg, for taking the time to review my thesis. I also wish to thank Jennifer Higgs for helping edit my thesis.

To my family, a special thank you must go out to my parents for their never-ending support. They have always been my teachers, role models and friends. I cannot express how fortunate I am to be their son. I also wish to thank my sister Erin, for her support and wish her the best in her teaching career.

I wish to thank my colleagues within the Multifunctional Structures Lab of University of Toronto Institute for Aerospace Studies: Dane Haystead, Richard Lee, Collins Ogunpide and John Chu, in addition to all my friends within UTIAS community. I also cannot forgot my friends within Shorinji Kan Jiu Jitsu for keeping me in the game all this time, even after the bruises.

I wish to thank Lilex Industries for machining the whippletree testing future for the following project.

Last, and certainly not least, I would like to thank my grandfather John "Jack" Keenan, my inspiration into pursuing a career in engineering.

Bryan Keenan Wright
University of Toronto Institute for Aerospace Studies

Contents

Nomenclature

Key Parameters

Variable	Parameter	Unit
P	Load	N
w	Pressure	kPa
M	Mass	kg
x	Position along beam	mm
$y(x)$	Deflection, wrt x	mm
$P/\delta, w/\delta$	Stiffness	N/mm, kPa/mm
δ	Midspan deflection	mm
$(EI)_{eq}$	Equvalent bending stiffness	Nmm^2
$(AG)_{eq}$	Equivalent shear stiffness	N
$\hat{P}$	Load Index	-
$\hat{w}$	Pressure Index	-
$\hat{M}$	Mass Index	-
$\hat{P}/\hat{\delta},\ \hat{w}/\hat{\delta}$	Stiffness Index	-
$\hat{\delta}$	Deflection Ratio	-

Beam Parameters

Variable	Parameter	Unit
t	Face sheet thickness	mm
c	Core thickness	mm
L	Beam length	mm
b	Beam width	mm
d	Distance between face sheet centroids (t+c)	mm
H	Beam overhang	mm

Material Properties

Variable	Parameter	Unit
E_f	Face sheet elastic modulus	GPa
σ_f	Face sheet compressive strength	MPa
ρ_f	Face sheet density	kg/m^3
E_c	Core elastic modulus	MPa
σ_c	Core compressive strength	kPa
G_c	Core shear modulus	MPa
τ_y	Core shear yield stress	kPa
τ_c	Core shear strength	kPa
ρ_c	Core density	kg/m^3

Non-Dimensional Ratios

$\bar{t} = \frac{t}{c}$	$\bar{c} = \frac{c}{L}$
$\bar{a} = \frac{a}{L}$	
$\hat{P} = \frac{P\phi}{\sigma_f bL}$	$\hat{w} = \frac{w}{\sigma_f}$
$\hat{\delta} = \frac{\delta}{L}$	$\hat{M} = \frac{M\psi}{\rho_f bL^2}$
$\phi = \frac{\sigma_f}{\sigma_{GFRP}}$	$\psi = \frac{\rho_f}{\rho_{GFRP}}$
$\bar{E}_f = \frac{E_f\phi}{\sigma_f}$	$\bar{E}_c = \frac{E_c\phi}{\sigma_f}$
$\bar{G} = \frac{G_c\phi}{\tau_c}$	$\bar{\tau} = \frac{\tau_c\phi}{\sigma_f}$
$\bar{\sigma} = \frac{\sigma_c\phi}{\sigma_f}$	$\bar{\rho} = \frac{\rho_c\psi}{\rho_f}$

Chapter 1

Introduction

Composite materials have become a dominant choice in lightweight structural design due to a high stiffness to weight ratio. One variation is the composite sandwich panel: a structure comprised of two thin stiff face sheets around a low density core material. Composite sandwich panels can be tailored to satisfy any strength requirement or weight limitation, based on the vast array of materials available. Such examples include metallic or fibre-reinforced face sheets and foam, truss or honeycomb cores.

Though composite materials in general have the potential to replace traditional structural materials (such as homogenous metallic beams or panels), predicting stiffness and strength behaviour using traditional beam theory is complicated by their complex geometry. As such, only a select number of material configurations have been investigated for an even smaller number of loading cases. Without the understanding of how each material and loading case works, optimal structural configurations cannot be determined unless a prohibitive number of experiments are conducted.

1.1 Summary of Previous Work

Notable early work in sandwich beam theory includes Allen [1], Plantema [29] and Zenkert [43], each considering the simplified model of an arbitrary face sheet and core material deflecting under various applied loads. Subsequent work by Gibson [14] examines metal and polymer foam cores while Ashby *et al.* [3] focuses on metal foams.

Composite sandwich structures have been primarily studied for simply supported three point bending. Relevant works in three point bending include Steeves and Fleck [36, 37, 38], who determine analytical expressions for the stiffness and strength for simply supported composite sandwich beams comprised fibre-reinforced face sheets and polymer foam cores. Analytical models are validated through experiments then compared to finite element simulation results. Rizov [30, 31] compares 2D and 3D finite element models to experiments for beams comprised of GFRP face sheets and Divinycell foam core. Sadighi *et al.*[13], Gdoutos *et al.*[32], and Lim *et al.*[25] investigate simply supported three point bending for GFRP/PVC and GFRP/polyurethane beams, while Chiras *et al.* [8] investigates three point bending on metal truss cores.

Only recently have different load cases been investigated, including simply supported four point bending and concentrated punch loading. Works in four point bending include Gibson [15], deriving expressions for midspan deflection for beams comprised of CFRP and GFRP face sheets to polymethacrylimide (PMI) foam core. Other works include Chen *et al.* [7] for metal face sheets and cores, Casari *et al.* [6] for Novel K-Cor Structures and Madhi *et al.* [27] for GFRP/NOMEX honeycomb cores. Tagarielli and Fleck [39] validated strength expressions for concentrated punch loading for both simply supported and clamped beams.

Another case is uniformly distributed loading, whereby the structure is subject to a pressure, such as air or water. Though experiments has been completed for uniformly distributed loading, no attempt has been made to propose analytical models for strength and stiffness. From previous literature, the only noted testing method for pressure loads has been the implementation of airbags, shown by White [42] on wood pallets and Islam [21] on composite beams.

Introduced by Gibson and Ashby [14], failure mechanism mapping considers a design space of geometric variables that define a structure. For a fixed set of material properties, a design space of dimensionless structural parameters can be divided into regions, where in each region a single failure mechanism dominates. The result is a visual representation of all competing failure mechanisms for a structure. By comparing load to mass gradients, minimum mass trajectories for optimal beam design configurations are determined. Previous literature on failure mechanism mapping include Steeves and Fleck [36, 37, 38], Kazemahvazi *et al.* [24] for metallic core composite sandwich beams under shear loading and Mohan *et al.* [28] for CFRP/aluminum foam core beams subject to simply supported three point bending. Recent work by Steeves [35] accounts for mass and stiffness limits for simply supported three point bending.

1.2 Project Scope

The following master's thesis investigates symmetric four point bending and uniform loading cases for simply supported composite sandwich beams comprised of fibre reinforced face sheets and polymer foam cores. The study encompasses the following two primary objectives:

- To define and validate analytical models of stiffness and strength
- To determine the optimal beam design trajectories considering for minimum mass

Extensive research has already been completed for three point bending, and thus, is used as a reference model for sandwich beam theory. Analytical models for four point bending and uniformly distributed loading are validated through a series of experiments.

Chapter 2

Background

2.1 Review of Sandwich Beam Mechanics

Consider Figure 2.1, a simply supported composite sandwich beam comprised of two thin stiff face sheets and a low density core. Let L be the beam length, and H be the overhang. Remaining beam geometry includes face sheet thickness t, core thickness c, beam width b and distance between face sheet centroids d ($d = c + t$). Relevant material properties for the face sheets are density ρ_f, elastic modulus E_f and compressive strength σ_f. Relevant material properties for the core are density ρ_c, elastic modulus E_c, compressive strength σ_c, shear modulus G_c and shear strength τ_c.

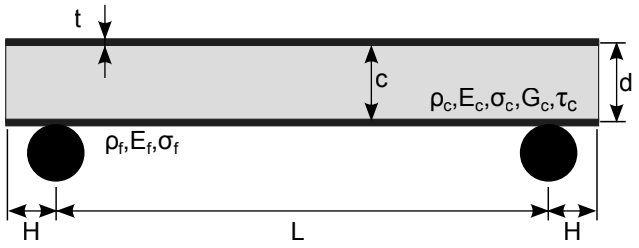

Figure 2.1: Geometry of a simply supported composite sandwich beam

For sandwich beam theory, two key design objectives must be addressed: stiffness and strength. Stiffness, or rigidity, is the measure of resistance a structure to deformation. Strength is the peak load a structure can withstand before failure. Multiple works have already validated stiffness and strength expressions for simply supported three point bending, considering different face and core materials [3, 36, 32, 39].

For three point bending, consider a transverse load P that is applied to the midspan of the beam, seen in Figure 2.2.

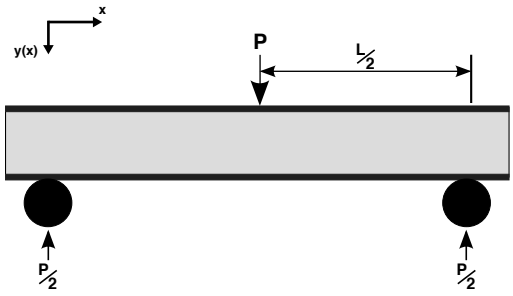

Figure 2.2: A simply supported composite sandwich beam subject to three point bending

The corresponding shear force and bending moment diagrams for three point bending are shown in Figure 2.3.

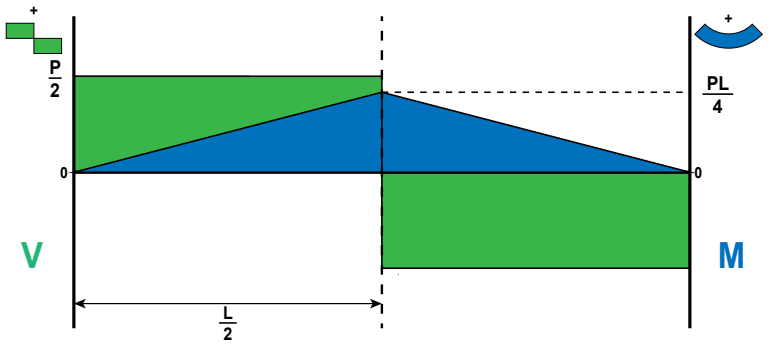

Figure 2.3: Shear and bending moment diagrams for a simply supported composite sandwich subject to three point bending

2.1.1 Stiffness

Composite sandwich beam stiffness relates P, the applied load to δ, the midspan deflection. An expression for beam stiffness is derived by evaluating both bending and shear effects of deflection. For three point bending,

$$\delta = \delta_{bending} + \delta_{shear} = \frac{PL^3}{48(EI)_{eq}} + \frac{PL}{4(AG)_{eq}}. \tag{2.1}$$

where $(EI)_{eq}$ and $(AG)_{eq}$ are the equivalent bending stiffness and shear stiffness terms for a beam. Therefore, the stiffness of a simply supported composite sandwich beam when subject to three point bending is

$$\frac{P}{\delta} = \left[\frac{48(EI)_{eq}(AG)_{eq}}{12(EI)_{eq} + (AG)_{eq}L^2}\right]. \tag{2.2}$$

For composite sandwich structures, $(EI)_{eq}$ is

$$(EI)_{eq} = E_f \frac{bt^3}{6} + E_c \frac{bc^3}{12} + E_f \frac{btd^2}{2}. \tag{2.3}$$

From Equation (2.3), the first two terms define the individual contributions of the face sheets and core; the third term is a relationship for the bending axis of the face sheets with respect to the neutral axis of the beam.

The equivalent shear stiffness equation, $(AG)_{eq}$, is:

$$(AG)_{eq} = \frac{bG_c d^2}{c}. \tag{2.4}$$

Figure 2.4 compares the cross-sectional axial and shear stress profiles for a sandwich beam subject to bending:

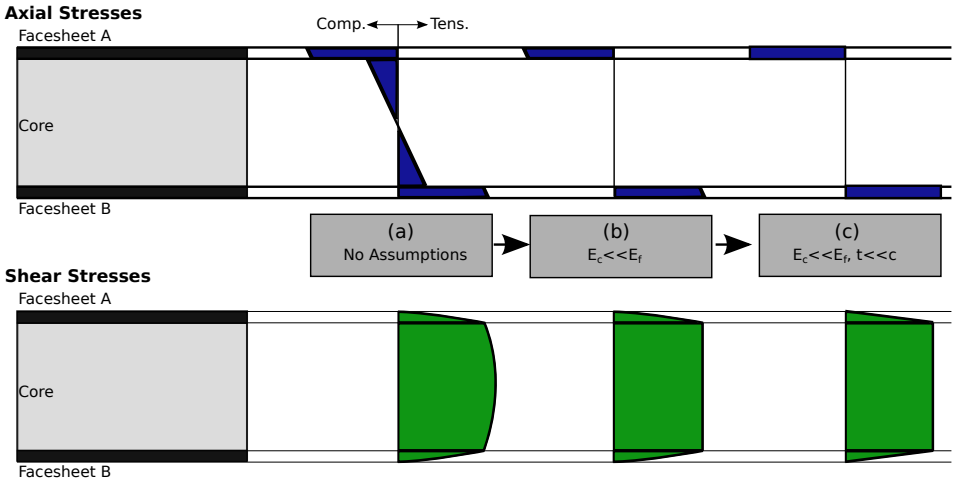

Figure 2.4: Axial and shear stress profiles of composite sandwich beams subject to bending

In sandwich beam design, elastic and shear moduli of the core are small compared to the face sheet ($E_c << E_f$, $G_c << G_f$). Therefore, it is assumed core shear stress is constant and core axial stress is negligible (seen in Figure 2.4(b)). Second, face sheets are very thin compared to the core, $t << c$. Assuming $d \approx c$, axial stress within each face is constant, and shear stress in the face sheet is linear (seen in Figure 2.4(c)). Using the above assumptions, the bending stiffness equation becomes

$$(EI)_{eq} \approx E_f \frac{btd^2}{2}, \tag{2.5}$$

and shear stiffness becomes

$$(AG)_{eq} \approx bdG_c. \tag{2.6}$$

2.1.2 Strength

Failure occurs when a critical stress in the core or face sheet is exceeded. In all cases, the corresponding peak load of the beam is a function of the component material properties and geometry. The weakest mechanism is considered the active failure mechanism for a given configuration. Figure 2.5 lists the failure mechanisms applicable to sandwich beams.

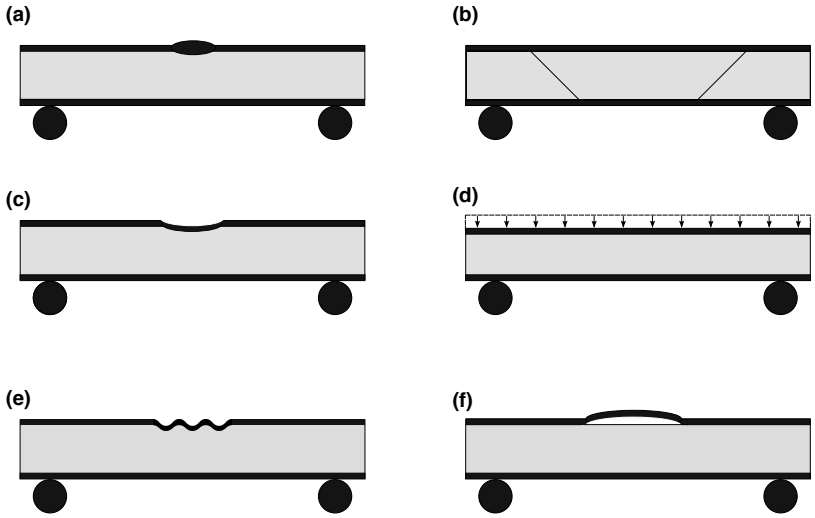

Figure 2.5: Failure mechanisms for sandwich beams, (a) face yield, (b) core shear, (c) indentation, (d) core crushing, (e) face wrinkling, (f) adhesion failure

Face Yield and Microbuckling

Face yield occurs when the tensile or compressive strength of the face material is exceeded. For fibre-reinforced face sheets, microbuckling is the associated compressive face failure, whereby the material fails through kink band formation [26, 5]. For fibre-reinforced polymer face sheets, the compressive strength is significantly lower than the tensile strength, hence only microbuckling is considered. Steeves and Fleck [36] express the microbuckling failure load equation for simply supported three point bending as

$$P_{MB} = \frac{4btd\sigma_f}{L}. \tag{2.7}$$

The use of the face sheet compressive strength to predict microbuckling failure requires caution. Though the face sheet failure is from an axial stress, the compressive strength only applies to a pure uniaxial compressive load. Prior to microbuckling, the face sheet material is subject to a multiaxial stress state. As a result, the actual material strength may be higher than predicted [36].

Core Shear

Core shear failure occurs when the shear strength of the core material is exceeded. In response to core shear, the face sheet either develops plastic hinges (common for metallic face sheets) [1] or elastically deforms [36]. Early models for core shear only consider the shear effects of core [1, 29],

$$P_{CS} = 2bd\tau_c. \tag{2.8}$$

More recent works consider the face sheet as an additional stiffening property [8]. The failure load expression is derived using Timoshenko beam theory, where for three point bending

$$P'_{CS} = 2bd\tau_c + 8E_f b\left(\frac{t}{L}\right)^3 \delta. \tag{2.9}$$

Noted in Tagarielli and Fleck, simply supported beams of elastic-plastic cores are shown to yield higher failure threshold if they are designed with considerable overhang [39]. To compensate, an overhang factor may be applied

$$P''_{CS} = P_{CS}\left(\frac{(L+2H)}{L}\right). \tag{2.10}$$

As the strengthening term of Equation (2.9) is negligible for cases of small beam deflections before failure, the following study considers the model in Equation (2.8); the additional overhang factor only applies to beams comprising elastic-plastic cores.

Core Crushing

Core crushing occurs when the transverse applied load exceeds the compressive strength of the core, over the entire length of the beam

$$P_{CC} = \sigma_c bL. \tag{2.11}$$

Indentation

Indentation is an interaction failure between the face sheet and core. At a critical load, the face sheet collapses into the core material within a localized region of length 2λ. Figure 2.6 illustrates the occurrence of indentation failure for a composite sandwich beam.

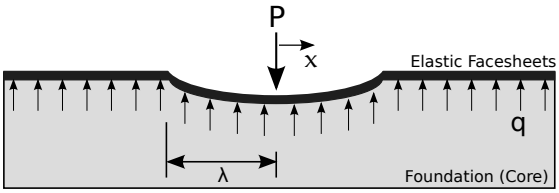

Figure 2.6: Indentation failure region for a simply-supported composite sandwich beam subject to three point bending

For ductile face sheets, such as metals, indentation is caused by the formation of plastic hinges on the top face sheet [2, 39]. For elastic face sheets, such as polymers, the top face elastically buckles into the core at a critical load [16].

The core, however, may be treated one of three ways: rigid-ideally plastic, elastic-ideally plastic and purely elastic. Rigid-ideally plastic cores collapse when the core compressive strength is exceeded [36, 33]. For an elastic-ideally plastic core, core indentation is initially assumed elastic until the load surpasses a yield point. The result is a two-phase indent of the core: elastic indentation surrounding an inner region of plastic collapse [36, 33, 13]. If the core is assumed purely elastic, the face sheet still buckles, but no plastic collapse is evident [16, 33]. For the simply supported three point bending expression derived by Steeves and Fleck, elastic face sheets and a rigid-ideally plastic core are considered [36, 37]:

$$P_I = bt\left(\frac{\pi^2 dE_f\sigma_c^2}{3L}\right)^{1/3} \tag{2.12}$$

Face Wrinkling

Face wrinkling is a material-specific failure mechanism whereby a face sheet buckles within the cell size of the core material. The following failure is common in honeycomb or lattice core composite sandwich materials but does not apply for polymer foams.

Adhesion Failure/Buckling-Induced Delamination:

Commonly referred to as debonding, decohesion or delamination, adhesion failure is the separation of the face sheet and core. Hutchinson and Suo detail various occurrences of adhesion failure and growth [22]. In addition to flat surfaces, interest has been also taken to curved substrates including Hutchinson [19], Clausen *et al.* with cornered composite materials [23] and Sorensen on spherical structures [34].

Buckling-induced delamiation is the adhesion failure applicable to sandwich beams subject to bending, whereby the localized separation of the face and core is generally attributed to compliant face sheets and weak adhesive strength. Though delamination has been well documented in terms of a crack (or blister) growth [22, 40, 11, 12], few attempts have been made to predict initial buckling load.

Adhesion failure rarely occurs because the strength of standard adhesives generally exceeds the strength of the core material. If in the event adhesion failure occurs, it is more due to an underlying fabrication fault than material selection.

2.2 Modelling Techniques - Failure Mechanism Map

Introduced by Gibson and Ashby [14], the failure mechanism map considers a design space of geometric variables that define a structure. For a fixed set of material properties, the design space can be divided into regions, where in each region a single failure mechanism exists. The result is a visual representation of all competing failure mechanisms for a structure in terms of peak load and mass gradient plots. Steeves and Fleck [36, 37, 38], Tagarielli and Fleck [39], Chen *et al.* [7], Mohan *et al.* [28] and Kazemahvazi *et al.* [24] adapt this method to illustrate failure for various composite sandwich beams.

The following study compares two face sheet materials, carbon fibre reinforced polymer (CFRP) and E-glass fibre reinforced polymer (GFRP). Two different core materials are also considered: Evonik Industires ROHACELL industrial grade (IG) polymethacrylimide (PMI) foam and Foamular C-300 extruded polystyrene (EPS) insulation foam.

The associated material properties are listed in Tables 2.1 and 2.2. While technical data for GFRP, CFRP, ROHACELL 51-IG and 110-IG are provided by online sources [36, 9, 20], a complete set of material properties for EPS are not available through online sources. As such, compression and shear tests are conducted to determine material properties of EPS and are noted in Chapter 3.

Table 2.1: Face sheet material properties

	Density, ρ_f (kg/m^3)	Elastic Modulus, E_f(GPa)	Compressive Strength, σ_f (MPa)
E-Glass Fibre Reinforced Polymer (GFRP)	1770	30	350
Carbon Fibre Reinforced Polymer (CFRP)	1600	70	570

Table 2.2: Core material properties

	Density, ρ_c (kg/m^3)	Elastic Modulus, E_c (MPa)	Compressive Strength, σ_c (MPa)	Shear Modulus, G_c (MPa)	Shear Yield, τ_y (MPa)	Shear Strength, τ_c (MPa)
EPS	28.94	13.41	0.423	6.75	0.282	0.357
ROHACELL 51-IG	52	70	0.9	19	-	0.8
ROHACELL 110-IG	110	160	3	50	-	2.4

Considering a design space of non-dimensional parameters $\bar{t} = t/c$ and $\bar{c} = c/L$, failure mechanism equations are expressed in non-dimensional terms using

$$\hat{P} = \frac{P\phi}{\sigma_f b L}, \tag{2.13}$$

while beam mass is expressed as

$$\hat{M} = \frac{M\psi}{\rho_f b L^2}. \tag{2.14}$$

All material properties are expressed as:

$$\begin{array}{lll} \bar{E}_f = \frac{E_f\phi}{\sigma_f}, & \bar{E}_c = \frac{E_c\phi}{\sigma_f}, & \bar{G} = \frac{G_c\phi}{\sigma_f}, \\ \bar{\sigma} = \frac{\sigma_c\phi}{\sigma_f}, & \bar{\tau} = \frac{\tau_y\phi}{\sigma_f}, & \bar{\tau} = \frac{\tau_c\phi}{\sigma_f}, \\ \bar{\rho} = \frac{\rho_c\psi}{\rho_f}, & \phi = \frac{\sigma_f}{\sigma_{GFRP}}, & \psi = \frac{\rho_f}{\rho_{GFRP}}. \end{array}$$

For comparative purposes, ψ and ϕ are added to relate CFRP to GFRP. Converting the mass and peak load equations for three point bending to non-dimensional terms yields

$$\hat{P}_{MB} = 4\bar{t}(\bar{t}+1)\bar{c}^2\phi, \tag{2.15}$$

$$\hat{P}_{CS} = 2\bar{\tau}(\bar{t}+1)\bar{c}, \tag{2.16}$$

$$\hat{P}_I = \left(\frac{\pi^2\bar{\sigma}^2\bar{E}_f}{3}\right)^{1/3}\bar{t}(\bar{t}+1)^{1/3}\bar{c}^{4/3}, \tag{2.17}$$

and

$$\hat{M} = (2\bar{t}+\bar{\rho}\psi)\bar{c}. \tag{2.18}$$

For the design space of $(0 \leq \bar{c} \leq 0.3)$ and $(0 \leq \bar{t} \leq 0.25)$, Figures 2.7-2.10 are the failure mechanism maps considering the following beam material combinations:

- GFRP and ROHACELL 51-IG
- GFRP and extruded polystyrene (EPS)
- GFRP and ROHACELL 110-IG
- CFRP and ROHACELL 51-IG

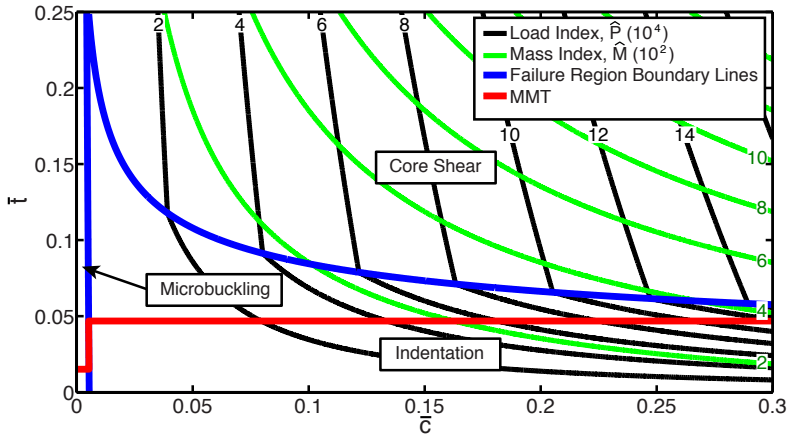

Figure 2.7: Failure mechanism map for a simply supported composite sandwich beam subject to three point bending, GFRP face sheets and ROHACELL 51-IG foam core, comparing non-dimensional contour plots of load and mass, dividing regions of active failure mechanism and predicting minimum mass trajectory (in red)

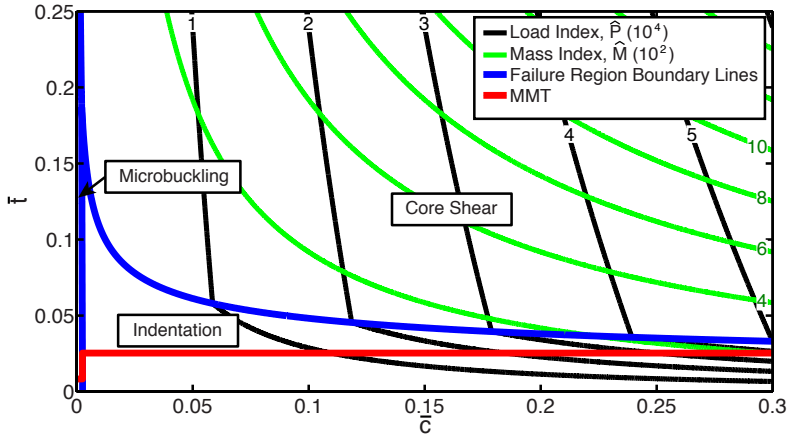

Figure 2.8: Failure mechanism map for a simply supported composite sandwich beam subject to three point bending, GFRP face sheets and extruded polystyrene (EPS) foam core, comparing non-dimensional contour plots of load and mass, dividing regions of active failure mechanism and predicting minimum mass trajectory (in red)

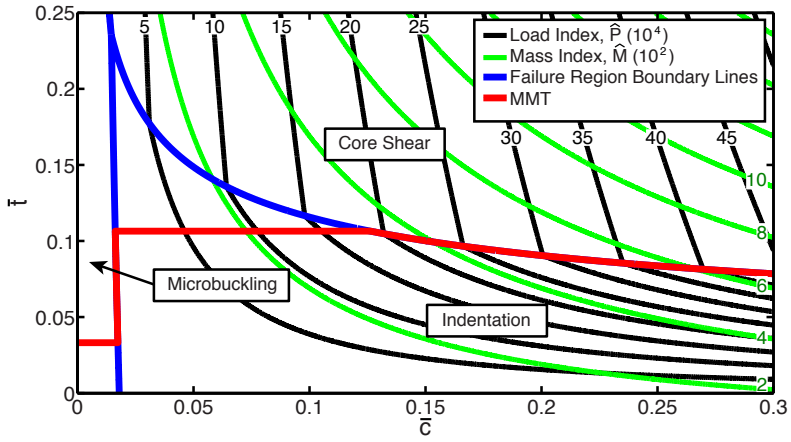

Figure 2.9: Failure mechanism map for a simply supported composite sandwich beam subject to three point bending, GFRP face sheets and ROHACELL 110-IG foam core, comparing non-dimensional contour plots of load and mass, dividing regions of active failure mechanism and predicting minimum mass trajectory (in red)

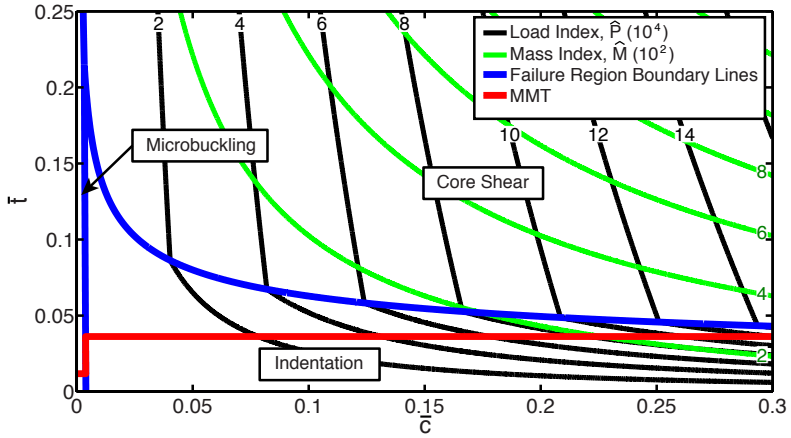

Figure 2.10: Failure mechanism map for a simply supported composite sandwich beam subject to three point bending, CFRP face sheets and ROHACELL 51-IG foam core, comparing non-dimensional contour plots of load and mass, dividing regions of active failure mechanism and predicting minimum mass trajectory (in red)

For each face and core, the three competing failure mechanisms exist within a defined failure region. For simply supported three point bending, microbuckling failure is predicted to exist for long beams of thin cores, indentation for beams of thick cores and thin faces, and core shear for short beams of thick faces.

As ROHACELL is stronger than EPS foam, ROHACELL beams are less prone to core shear or indentation, and is represented by a larger microbuckling failure region. However, GFRP/EPS beams are more prone to indentation due to the core shear strength being relatively higher than the compressive strength.

As CFRP is stronger, stiffer and lighter than GFRP, CFRP-constructed beams are less prone to microbuckling and indentation, seen in Figures 2.7 and 2.10.

To define the boundaries between each failure mechanism, load index equations may be combined to form critical relationships between $\bar{t}$ and $\bar{c}$.

First, lines define the boundaries of two active failure mechanisms. For a known $\bar{c}$ a corresponding $\bar{t}$ may be determined using the equations listed below:

i) Microbuckling/Core Shear

$$\bar{t} = \frac{\bar{\tau}}{2\bar{c}\phi} \tag{2.19}$$

ii) Core Shear/Indentation

$$\frac{(\bar{t}+1)^2}{\bar{t}^3} = \frac{\bar{E}_f \bar{c}}{24}\frac{(\pi\bar{\sigma})^2}{\bar{\tau}^3} \tag{2.20}$$

iii) Indentation/Microbuckling

$$\bar{t} = \frac{\pi\bar{\sigma}}{\bar{c}}\left(\frac{\bar{E}_f}{192\phi^3}\right)^{1/2} - 1. \tag{2.21}$$

The boundary point $(\bar{c}^*, \bar{t}^*)$ is material-specific design point where all three failure mechanisms intersect:

iv) Microbuckling/Core Shear/Indentation

$$\frac{\bar{t}}{(\bar{t}+1)} = \frac{\bar{\tau}}{\pi\bar{\sigma}}\left(\frac{48}{\bar{E}_f\phi}\right)^{1/2} \tag{2.22}$$

$$\bar{c}(\bar{c}+1) = \left[\frac{\pi^2\bar{\sigma}^2\bar{E}_f\phi}{192} - \left(\frac{\bar{\tau}\phi}{2}\right)^2\right]. \tag{2.23}$$

Denoted in red in Figures 2.7-2.10, the minimum mass trajectory represents the optimal beam set for a given load and material composition, considering mass reduction for a given strength. Within each failure region, the minimum mass trajectory is defined by the set of design space points where mass and load index gradients are parallel. All other points may exist along failure region boundary lines. For three point bending, locus points exist in both microbuckling and indentation failure regions; for the remaining domain of $\hat{P}$, the minimum mass trajectory exists along the microbuckling/indentation and core shear/indentation boundary lines.

2.3 Modelling Techniques - Minimum Mass Trajectory Line Plots

In addition to failure mechanism mapping, the minimum mass trajectory may be plotted with respect to the load index $\hat{P}$. The three design parameters considered are mass index $\hat{M}$, $\bar{t}$ and $\bar{c}$. Figure 2.11 compares the optimal mass index to load index for the four considered beam designs. For the first figure, $\hat{M} - \hat{P}$ lines represent the optimal beams that exist within the design space of $(0 \leq \bar{c} \leq 0.3)$ and $(0 \leq \bar{t} \leq 0.25)$. An accompanying figure highlights the finer details of each minimum mass trajectory for a small $\hat{P}$.

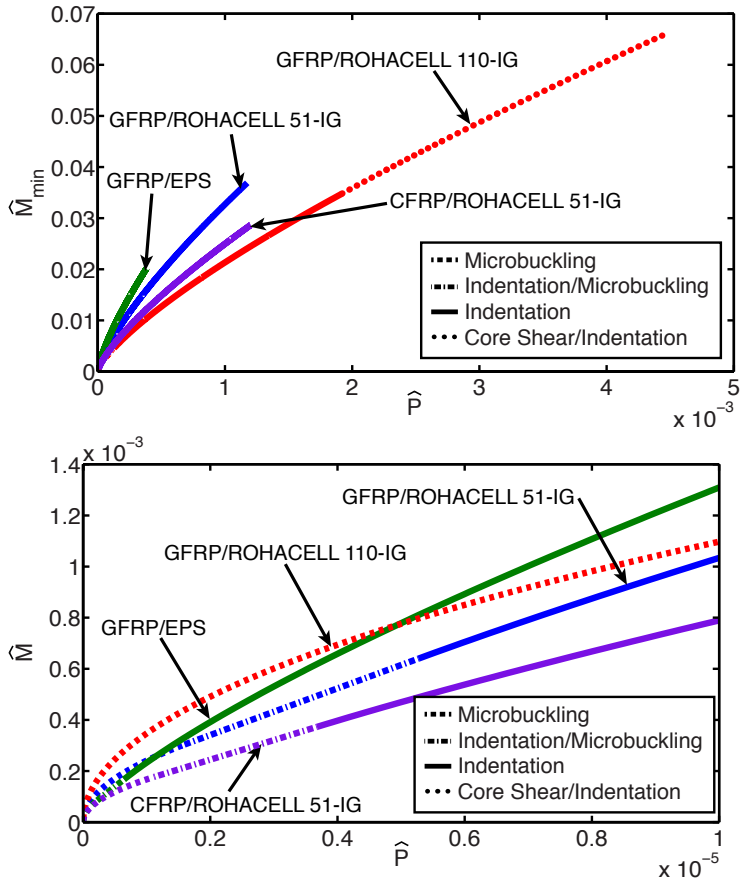

Figure 2.11: Plot of minimum mass trajectory in terms of mass index to load index for simply supported composite beams subject to three point bending - within the chosen design space (top), for a small $\hat{P}$ (bottom)

Designing beams comprised of either stiffer face sheets or stronger cores allows for a significantly higher load capacity. Stronger materials increase beam strength, but often at the cost of a greater mass. As CFRP is stiffer, stronger and lighter than GFRP, its $\hat{M} - \hat{P}$ curve has a smaller minimum mass index for a larger domain of $\hat{P}$ to GFRP beams.

Alternatively, Figures 2.12-2.13 plot beam geometry ratios $\bar{t}$ and $\bar{c}$ with respect to load index $\hat{P}$.

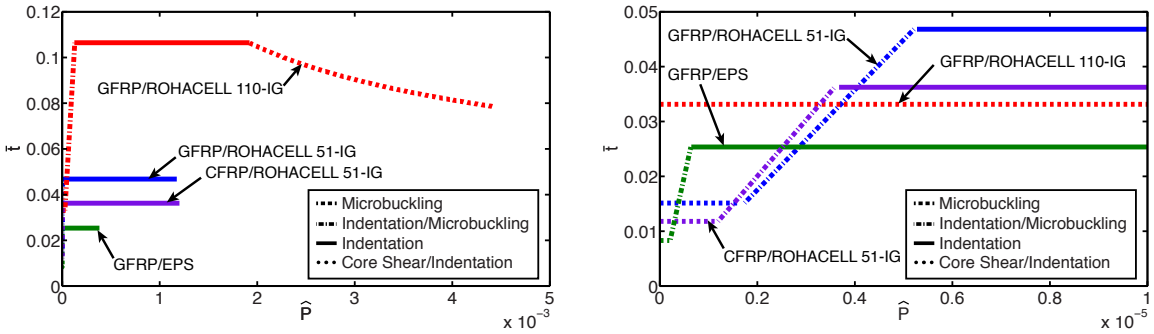

Figure 2.12: Plot of minimum mass trajectory in terms of $\bar{t}$ to load index for simply supported composite beams subject to three point bending - within the chosen design space (left), for a small $\hat{P}$ (right)

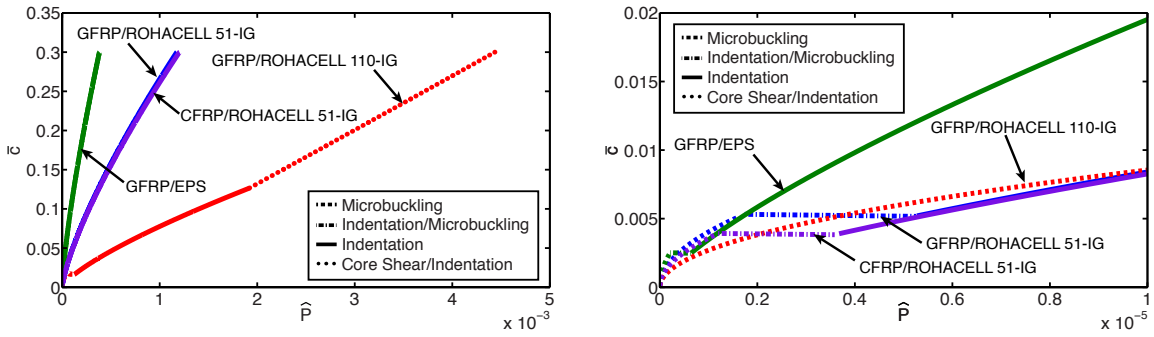

Figure 2.13: Plot of minimum mass trajectory in terms of beam geometry to load index for simply supported composite beams subject to three point bending - within the chosen design space (left), for a small $\hat{P}$ (right)

For both microbuckling and indentation failure regions, optimal beam designs are defined by a critical $\bar{t}$. For microbuckling,

$$\bar{t}_{MMT} = \frac{\bar{\rho}}{2\psi(1-\bar{\rho})}; \tag{2.24}$$

therefore, the corresponding $\bar{c}$ and mass index are

$$\bar{c}_{MMT} = \frac{(1-\bar{\rho})\hat{P}^{1/2}}{\sqrt{\phi\bar{\rho}(2-\bar{\rho})}} \tag{2.25}$$

$$\hat{M}_{MMT} = \sqrt{\frac{\bar{\rho}(2-\bar{\rho})^2\hat{P}}{\phi(2\psi-\psi\bar{\rho}+\bar{\rho})}}. \tag{2.26}$$

Similarily, for indentation

$$\bar{t}_{MMT} = \frac{3\bar{\rho}}{2\psi(1-\bar{\rho})}, \tag{2.27}$$

where corresponding $\bar{c}$ and mass index are

$$\bar{c}_{MMT} = 2(1-2\bar{\rho})\left[\frac{\bar{\rho}\hat{P}^3}{9\bar{\rho}^3(2-\bar{\rho})\pi^2\bar{\sigma}^2\bar{E}_f}\right]^{1/4} \tag{2.28}$$

$$\hat{M}_{MMT} = \frac{4(2-\bar{\rho})}{(\bar{\rho}(3-4\psi)+2\psi)^{1/4}}\left[\frac{\bar{\rho}\hat{P}^3}{9\pi^2\bar{\sigma}^2\bar{E}_f}\right]^{1/4}. \tag{2.29}$$

For all remaining $\hat{P}$, beam geometry ratios $\bar{t}$ and $\bar{c}$ are governed by the previously listed boundary line expressions. The resultant mass index for the indentation/microbuckling boundary line is

$$\hat{M}_{MMT} = \frac{\pi\bar{\sigma}\bar{\rho}}{8\phi^3}\left(\frac{\bar{E}_f}{3}\right)^{1/2} + \frac{2(2\psi-\bar{\rho})}{\pi\bar{\sigma}}\left(\frac{3}{\bar{E}_f}\right)^{1/2}\hat{P} \tag{2.30}$$

while for the core shear/indentation boundary line

$$\hat{M}_{MMT} = \left(\frac{\bar{\tau}^4(2\psi-\bar{\rho})+(\pi\bar{\sigma})^2\bar{E}_f\bar{\rho}\hat{P}}{2(48^2)\bar{\tau}^9}\right)(\pi\bar{\sigma})^2\bar{E}_f\hat{P}^2. \tag{2.31}$$

In summary, using the simply supported three point bending case as reference, sandwich beam theory has been reviewed. Expressions for both composite sandwich beam stiffness and strength are derived and, through the use of failure mechanism mapping, optimal beam designs are determined.

Chapter 3

Analysis

For following section, two load cases are analyzed: four-point bending and uniformly distributed loading. Similar to the approach taken in Chapter 2, the objective is to derive a set of expressions predicting both stiffness and strength and minimum mass trajectories are determined.

3.1 Case A: Simply-Supported, Symmetric Four Point Bending

Consider the simply-supported composite sandwich beam in Figure 3.1: two loads of equal magnitude ($P/2$) are applied the beam, at an equal distance a apart from one another.

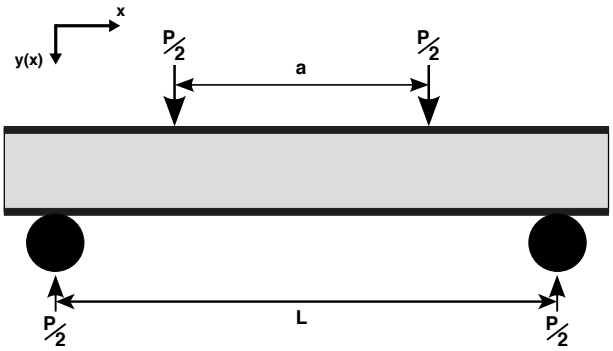

Figure 3.1: A simply supported composite sandwich beam subject to four point bending

Figure 3.2 compares shear and bending moment diagrams.

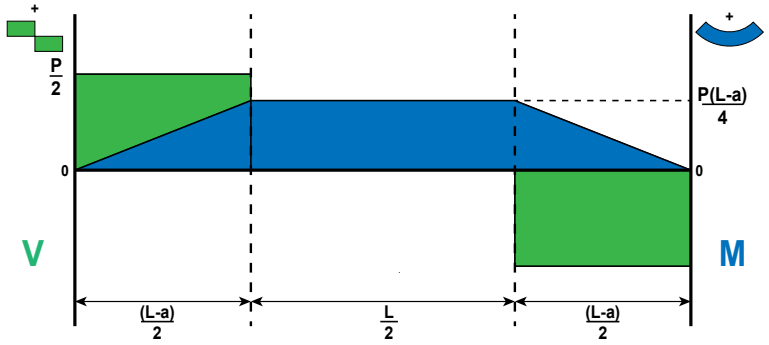

Figure 3.2: Shear and bending moment diagrams for a simply supported composite sandwich subject to four point bending

Although similar to three point bending, four point bending introduces a region of zero shear stress and constant bending moment between the applied point loads. While asymmetric variants of four point bending exist, only the symmetric case is considered here.

3.1.1 Stiffness

Recalling Chapter 2, deflection is predicted by combining bending and shear components:

$$\delta = \delta_b + \delta_s \tag{3.1}$$

For the bending component of deflection, four point bending considers two regions:

- Outer region A: side support to the point load $(0 < x < (L-a)/2)$
- Inner region B: point load to the midspan $((L-a)/2 < x < L/2)$

Seen in Figure 3.2, the maximum bending moment present is $M = P(L-a)/4$ at a distance $(L-a)/2$ from the edge. Considering Euler-Bernoulli beam theory,

$$EI\frac{d^2y(x)}{dx^2} = -M = -\frac{P(L-a)}{4}; \tag{3.2}$$

where y(x) refers to the deflection. Similarly, the maximum shear force present on the outer regions of the beam is $P/2$, thus

$$EI\frac{d^3y(x)}{dx^3} = V = -\frac{P}{2}. \tag{3.3}$$

By integrating Equation (3.2) and (3.3)

$$y(x)|_A = -\frac{P}{12EI}x^3 + \frac{C_1}{2}x^2 + C_2x + C_3, \tag{3.4}$$

where $y(x)|_A$ is the deflection equation for the outer region, and for the inner region

$$y(x)|_B = -\frac{P}{8EI}\left(x - \frac{(L-a)}{2}\right)^2 + D_1\left(x - \frac{(L-a)}{2}\right) + D_2. \tag{3.5}$$

To solve the above set of equations, the following boundary conditions are set:

- No deflection at the ends, $y(0) = 0$
- Midspan slope is zero (symmetry), $dy(L/2)/dx = 0$
- Bending moment at the ends are zero, $d^2y(0)/dx^2 = 0$
- Slope is continuous at $x = (L-a)/2, \quad dy/dx|_A = dy/dx|_B$
- Deflection is continuous at $x = (L-a)/2, \quad y|_A = y|_B$

Solving for $y(x)$,

$$y(x)|_A = \frac{Px}{48EI}[3(L-a)(L+a) - 4x^2] \tag{3.6}$$

for the outer region and

$$y(x)|_B = \frac{P(L-a)}{96EI}[12x(L-x) - (L-a)^2] \tag{3.7}$$

for the inner region respectively.

From here, the bending contribution of deflection may be estimated from two key nodes: at one of the two point loads

$$\delta_{bP} = y\Big|_A\left(\frac{(L-a)}{2}\right) = \frac{P(L-a)^2(L+2a)}{48EI}, \tag{3.8}$$

and at the midspan

$$\delta_{bM} = y\Big|_B\left(\frac{L}{2}\right) = \frac{P(L-a)}{96EI}[3L^2 - (L-a)^2]. \tag{3.9}$$

In Figure 3.2, the maximum shear is $P/2$. For both the point load roller and the midspan, the shear contribution to deflection is

$$\delta_s = \frac{P(L-a)}{4AG}. \tag{3.10}$$

Therefore, the deflection at the point loads is

$$\delta_{bP} = \frac{P(L-a)^2(L+2a)}{48EI} + \frac{P(L-a)}{4AG}, \tag{3.11}$$

while for the midspan

$$\delta = \frac{P(L-a)}{96EI}[3L^2 - (L-a)^2] + \frac{P(L-a)}{4AG}. \tag{3.12}$$

Rewriting Equation (3.12), the stiffness of a simply supported composite sandwich beam subject to four point bending is

$$\frac{P}{\delta} = \left[\frac{96(EI)_{eq}(AG)_{eq}}{(L-a)(24(EI)_{eq} + (AG)_{eq}(3L^3 - (L-a)^2))}\right]. \tag{3.13}$$

Although deflection at the point loads may be required for certain experiment setups, only midspan deflection is considered beyond this point.

3.1.2 Strength

With four point bending, the same set of failure mechanisms seen in three point bending exist: microbuckling, core shear and indentation.

Failure Mechanism #1: Microbuckling

Figure 3.3 depicts the cross-section of a composite beam with neutral axis NA:

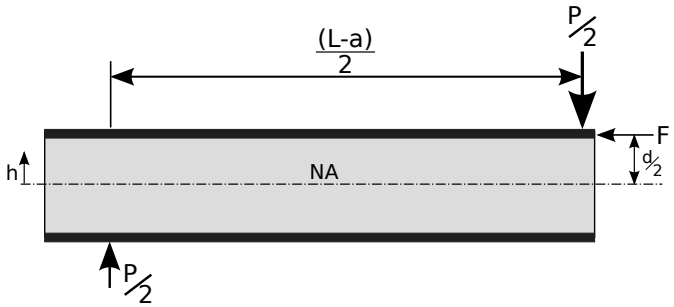

Figure 3.3: Cross section of simply-supported composite sandwich beam under buckling load F, with neutral axis NA

The applied buckling load F is derived from the bending moment stress equation

$$\sigma_f = \frac{Mh}{I}; \tag{3.14}$$

where for a composite sandwich beam, the displacement h from the neutral axis is $h = d/2$. In terms of the equivalent bending stiffness:

$$\sigma_f = \frac{Md}{2}\frac{E_f}{(EI)_{eq}}. \tag{3.15}$$

where from Chapter 2, $(EI)_{eq} = E_f btd^2/2$. For $M = P/(L-a)$,

$$\sigma_f = \left(\frac{P(L-a)}{4}\right)\left(\frac{d}{2}\right)E_f\left(\frac{2}{E_f btd^2}\right). \tag{3.16}$$

Therefore, the load at microbuckling failure is

$$P_{MB} = \frac{4btd\sigma_f}{(L-a)}. \tag{3.17}$$

To recall, the microbuckling equation for three point bending is $P_{MB} = 4btd\sigma_f/L$. With the only difference being a reduction of bending moment arm from $L/2$ to $(L-a)/2$, four point bending is presumed to have a higher microbuckling failure load than three point bending.

Failure Mechanism #2: Core Shear

To solve for core shear, work done by Allen [1] is considered. For composite materials,

$$\tau = \frac{Vs}{(EI)_{eq}b}\Sigma SE, \tag{3.18}$$

where τ is the shear stress, s first moment of area, and I and second moment of inertia. Considering only the core, the expression for ΣSE is

$$\Sigma SE = \frac{E_f btd}{2} + \frac{E_c b}{2}\left(\frac{c}{2} - z\right)\left(\frac{c}{2} + z\right). \tag{3.19}$$

The resulting expression for τ becomes:

$$\tau = \frac{V}{(EI)_{eq)}}\left[\frac{E_f td}{2} + \frac{E_c}{2}\left(\frac{c^2}{4} - z^2\right)\right]. \tag{3.20}$$

From here, the same two assumptions from Chapter 2 are considered: assuming the core is compliant compared to the face sheets ($E_f >> E_c$), and the face sheet thickness is negligible to the core $t >> c$. Replacing $(EI)_{eq}$ yields

$$\tau = \frac{V}{bd}. \tag{3.21}$$

Due to shear being independent of beam length, the shear force applied to the beam for both three and four point bending cases is $V = P/2$. Therefore, core shear failure for both three and four point bending is defined by

$$P_{CS} = 2b\tau_c d, \tag{3.22}$$

where overhang factor $(L + 2H)/L$ is applied to beams comprised of elastic-plastic cores.

Failure Mechanism #3: Indentation

Following the three point bending model in Chapter 2, work by Hetenyi is recalled, considering an infinitely long elastic beam resting on a rigid-ideally plastic material, subject to an applied load $P/2$ [16]. For a composite sandwich beam, the model describes the interaction between the top face sheet and core. Taking an infinitely small section of the top face sheet generates the free body diagram seen in Figure 3.4.

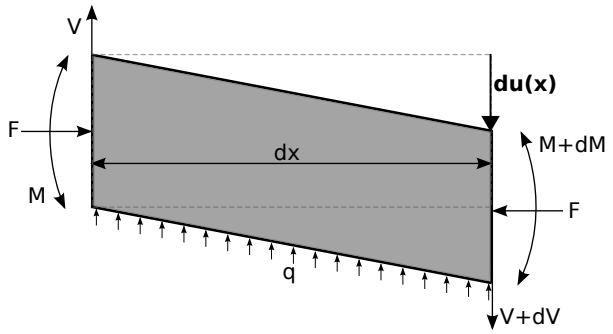

Figure 3.4: Free body diagram for an infinitely small section of a simply supported elastic beam

For four point bending, two separate instances of core indentation occur simultaneously. Assuming symmetry, consider a half-length model of the beam where core indentation occurs a distance $(L - a)/2$ from the edge.

Taking moments around the left side of the elastic beam element, equilibrium is

$$M - (M + dM) + (V + dV)dx - qbdx^2 + F\frac{du}{dx}dx = 0, \tag{3.23}$$

where M represents the bending moments, V the shear forces and F the buckling load across the element. The term $u(x)$ is the indentation of the point load roller into the core foundation. Dividing the expression by dx yields

$$\frac{dM}{dx} + (V + dV) - qbdx + F\frac{du}{dx} = 0, \tag{3.24}$$

where the reaction q is $qb = \frac{dV}{dx} = \sigma_c b$.

Differentiating Equation (3.24) yields the following non-homogenous ordinary differential equation for u(x):

$$\frac{d^4u}{dx^4} + \frac{F}{EI}\frac{d^2u}{dx^2} = \frac{\sigma_c b}{EI}; \tag{3.25}$$

Solving for u(x) yields:

$$u(x) = A_1 cos(kx) + A_2 sin(kx) + A_3 x + A_4 - \frac{\sigma_c b x^2}{2F}, \tag{3.26}$$

where

$$k^2 = \sqrt{\frac{F}{EI}}. \tag{3.27}$$

Considering the indentation has finite length λ, the following boundary conditions are set:

- $du(0)/dx = 0$
- $d^3u/dx^3(0) = P/2EI$
- $u(\lambda) = 0$
- $du(\lambda)/dx = 0$
- $d^2u(\lambda)/dx^2 = 0$

Solving for the constants:

$$A_1 = \frac{2d}{(L-a)k}\frac{(1 - cos\mu - \mu sin\mu)}{(sin\mu - \mu cos\mu)}, \tag{3.28}$$

$$A_2 = \frac{-2d}{(L-a)K}, \tag{3.29}$$

$$A_3 = \frac{2d}{(L-a)}, \tag{3.30}$$

$$A_4 = \frac{2d}{(L-a)K}\left(\frac{1 - cos\mu - \mu sin\mu}{sin\mu - \mu cos\mu}\right) + \frac{d\mu^2}{(L-a)k}\left(\frac{1 + cos\mu}{sin\mu - \mu cos\mu}\right), \tag{3.31}$$

where $\mu = \lambda/k$. As $du(0)/dP =$,

$$P = bt\left[\frac{4dE_f\sigma_c^2}{3(L-a)}\left(\frac{sin\mu - \mu cos\mu}{1 - cos\mu}\right)^2\right]^{1/3} \tag{3.32}$$

and

$$u(0) = \frac{4d}{(L-a)k}\left(\frac{1 - cos\mu - \mu sin\mu}{sin\mu - \mu cos\mu}\right) + \frac{d\mu^2}{(L-a)k}\left(\frac{1 + cos\mu}{sin\mu - \mu cos\mu}\right). \tag{3.33}$$

Assuming load P is maximum when $\mu \approx \pi$,

$$P_{max} = bt\left(\frac{\pi^2 dE_f\sigma_c^2}{3(L-a)}\right)^{1/3}. \tag{3.34}$$

Accounting for two separate instances of indentation on the beam, the failure expression becomes

$$P_I = 2bt\left(\frac{\pi^2 dE_f\sigma_c^2}{3(L-a)}\right)^{1/3}. \tag{3.35}$$

3.1.3 Failure Mechanism Mapping

To transform the above failure load expressions into non-dimensional terms, the same relationships listed in Chapter 2 are recalled here. To account for the load spacing term a, dimensionless parameter $\bar{a} = a/L$ is introduced. The resulting non-dimensional expressions for four point bending are

$$\hat{P}_{MB} = \frac{4\bar{t}(\bar{t}+1)\bar{c}^2\phi}{(1-\bar{a})}, \tag{3.36}$$

$$\hat{P}_{CS} = 2\bar{\tau}(\bar{t}+1)\bar{c}, \tag{3.37}$$

$$\hat{P}_I = 2\left(\frac{\pi^2\bar{\sigma}^2\bar{E}}{3(1-\bar{a})}\right)^{1/3}\bar{t}(\bar{t}+1)^{1/3}\bar{c}^{4/3}, \tag{3.38}$$

where the same expression for the mass index is used from Chapter 2 for three point bending:

$$\hat{M} = \frac{M}{\rho_{GFRP}bL^2} = (2\bar{t}+\bar{\rho}\psi)\bar{c}. \tag{3.39}$$

Figures 3.5-3.8 are the various failure mechanism maps for four point bending, assuming the same four material combinations in Chapter 2. All plots assume a constant $\bar{a} = a/L = 0.2$.

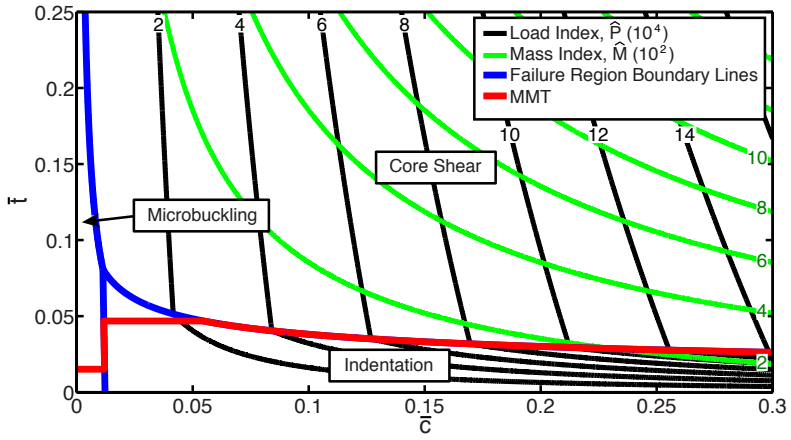

Figure 3.5: Failure mechanism map for a simply supported composite sandwich beam subject to four point bending, GFRP face sheets and ROHACELL 51-IG foam core, comparing non-dimensional contour plots of load and mass, dividing regions of active failure mechanism and predicting minimum mass trajectory (in red), $\bar{a} = 0.2$

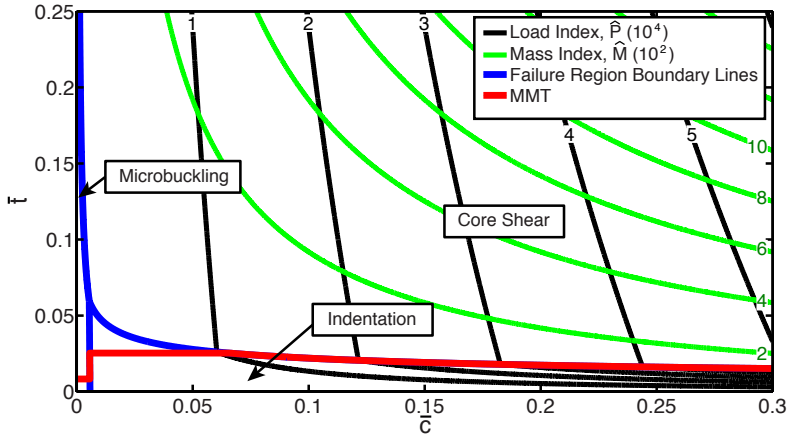

Figure 3.6: Failure mechanism map for a simply supported composite sandwich beam subject to four point bending, GFRP face sheets and extruded polystyrene (EPS) foam core, comparing non-dimensional contour plots of load and mass, dividing regions of active failure mechanism and predicting minimum mass trajectory (in red), $\bar{a} = 0.2$

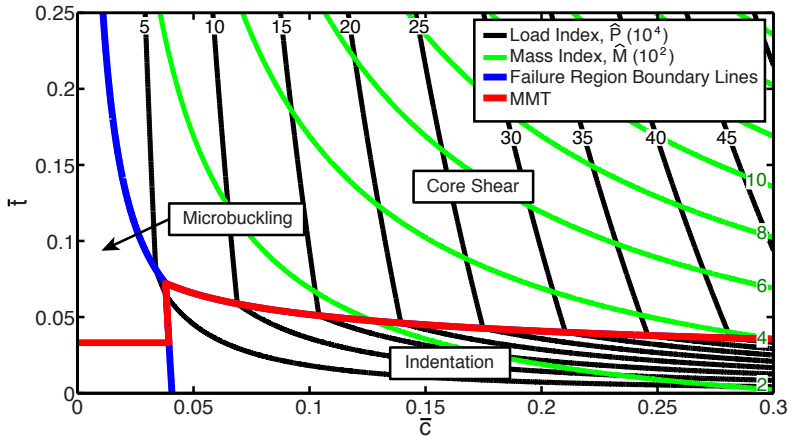

Figure 3.7: Failure mechanism map for a simply supported composite sandwich beam subject to four point bending, GFRP face sheets and ROHACELL 110-IG foam core, comparing non-dimensional contour plots of load and mass, dividing regions of active failure mechanism and predicting minimum mass trajectory (in red), $\bar{a} = 0.2$

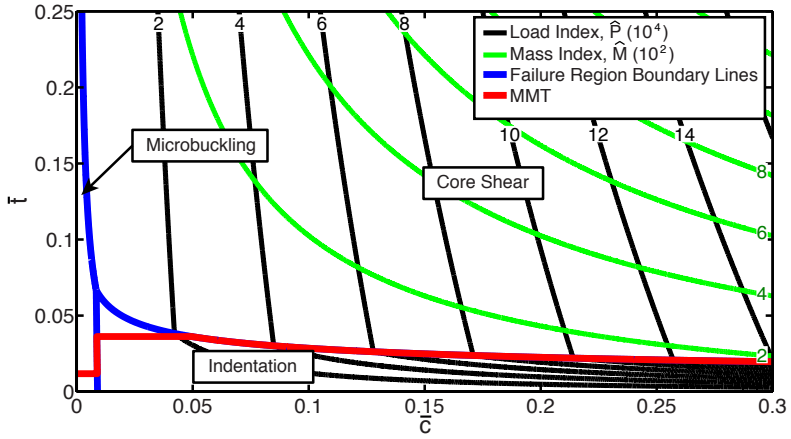

Figure 3.8: Failure mechanism map for a simply supported composite sandwich beam subject to four point bending, CFRP face sheets and ROHACELL 51-IG foam core, comparing non-dimensional contour plots of load and mass, dividing regions of active failure mechanism and predicting minimum mass trajectory (in red), $\bar{a} = 0.2$

The corresponding boundary lines between each failure region are defined by ($\bar{c}$,$\bar{t}$):

i) Microbuckling/Core Shear

$$\bar{t} = \frac{\bar{\tau}(1-\bar{a})}{2\bar{c}\phi} \tag{3.40}$$

ii) Core Shear/Indentation

$$\frac{\bar{t}^3}{(\bar{t}+1)^2} = \frac{\bar{E}_f \pi^2 \bar{\sigma}^2 \bar{c}}{3(1-\bar{a})\bar{\tau}^3} \tag{3.41}$$

iii) Indentation/Microbuckling

$$\bar{t}^* = \left(\frac{\bar{E}_f}{24\phi^3}\right)^{1/2}\left(\frac{\bar{\sigma}\pi(1-\bar{a})}{\bar{c}}\right) - 1 \tag{3.42}$$

iv) Microbuckling/Core Shear/Indentation

$$\frac{\bar{t}}{(\bar{t}+1)} = \frac{\bar{\tau}}{\pi\bar{\sigma}}\left(\frac{6\phi}{\bar{E}_f}\right)^{1/2} \tag{3.43}$$

$$\bar{c}^2 + \frac{\bar{\tau}(1-a)}{2\phi}\bar{c}^* - \frac{\bar{E}_f(\bar{\sigma}\pi(1-\bar{a}))^2}{12\phi^3} = 0 \tag{3.44}$$

Compared to three point bending, an increase in the required load for both microbuckling and indentation forces core shear to become the more dominant failure mechanism. As was the case for three point bending, it is not possible for a minimum-mass beam to fail solely due to core shear. As a result, the minimum mass trajectory exists along the boundary lines, where the mass and load index gradients are not parallel.

Solving for the minimum mass trajectory, the optimal $\bar{t}$ for the microbuckling and indentation failures regions is found to be the same as three point bending in Chapter 2 (Equations (2.24) and (2.27) respectively). Solving for $\bar{c}$ and $\hat{M}$ in the microbuckling failure region,

$$\bar{c}_{MMT} = (1-\bar{\rho})\left[\frac{(1-\bar{a})\hat{P}}{\phi\bar{\rho}(2-\bar{\rho})}\right]^{1/2}, \tag{3.45}$$

$$\hat{M}_{MMT} = \sqrt{\frac{\bar{\rho}(2-\bar{\rho})^2\hat{P}(1-\bar{a})}{(2\psi-\psi\bar{\rho}+\bar{\rho})\phi}}, \tag{3.46}$$

while for indentation

$$\bar{c}_{MMT} = 2(1-2\bar{\rho})\left[\frac{8\bar{\rho}(1-\bar{a})\hat{P}^3}{9\bar{\rho}^3(2-\bar{\rho})\pi^2\bar{\sigma}^2\bar{E}_f}\right]^{1/4}, \tag{3.47}$$

$$\hat{M}_{MMT} = \frac{4(2-\bar{\rho})}{(\bar{\rho}(3-4\psi)+2\psi)^{1/4}}\left[\frac{8\bar{\rho}(1-\bar{a})\hat{P}^3}{9\pi^2\bar{\sigma}^2\bar{E}_f}\right]^{1/4}. \tag{3.48}$$

For the boundary lines, mass index for indentation/microbuckling is

$$\hat{M}_{MMT} = \frac{\pi\bar{\sigma}\bar{\rho}(1-\bar{a})}{16\phi^3}\left(\frac{\bar{E}_f}{6}\right)^{1/2} + \frac{4(2\psi-\bar{\rho})}{\pi\bar{\sigma}(1-\bar{a})}\left(\frac{6}{\bar{E}_f}\right)^{1/2}\hat{P}, \tag{3.49}$$

while for core shear/indentation

$$\hat{M}_{MMT} = \left(\frac{\bar{\tau}^4(1-\bar{a})(2\psi-\bar{\rho}) + (\pi\bar{\sigma})^2\bar{E}_f\bar{\rho}\hat{P}}{72(1-\bar{a})^2\bar{\tau}^9}\right)(\pi\bar{\sigma})^2\bar{E}_f\hat{P}^2. \tag{3.50}$$

Figures 3.9 and 3.10 plot the change in beam geometry variables $\bar{t}$ and $\bar{c}$ with respect to the predicted load index.

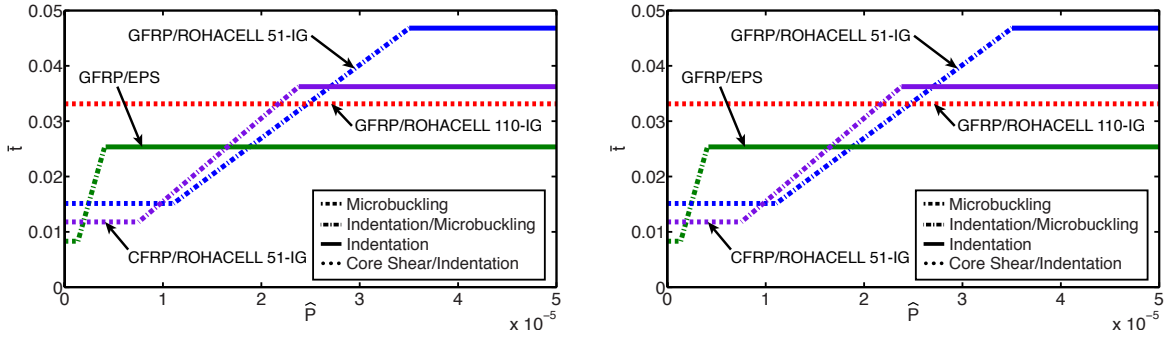

Figure 3.9: Plot of minimum mass trajectory in terms of $\bar{t}$ to load index for simply supported composite beams subject to four point bending, $\bar{a} = 0.2$ - within the chosen design space (left), for a small $\hat{P}$ (right)

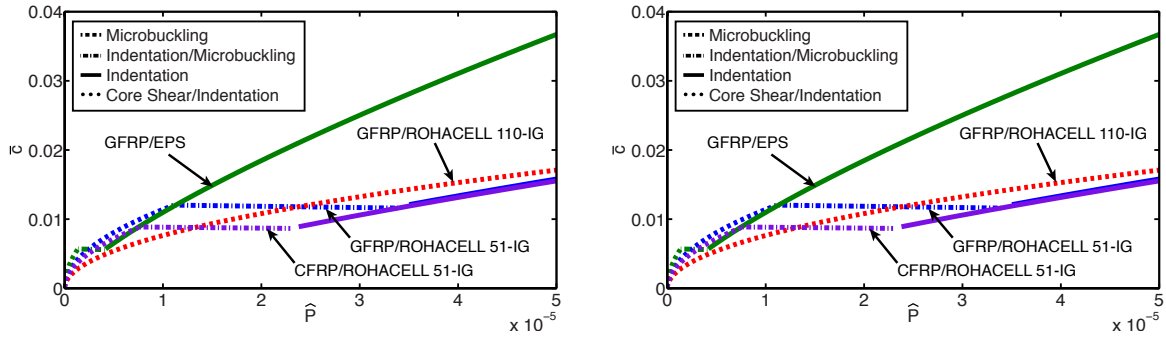

Figure 3.10: Plot of minimum mass trajectory in terms of $\bar{c}$ to load index for simply supported composite beams subject to four point bending, $\bar{a} = 0.2$ - within the chosen design space (left), for a small $\hat{P}$ (right)

Figure 3.11 plots the mass index in terms of the load index below.

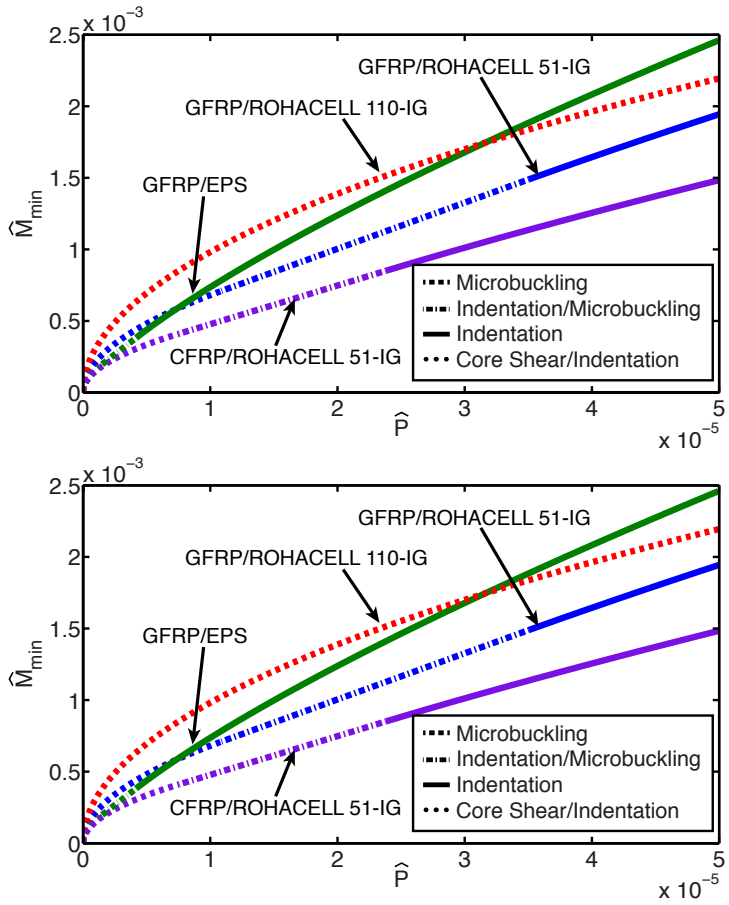

Figure 3.11: Plot of minimum mass trajectory in terms of mass index to load index for simply supported composite beams subject to four point bending, $\bar{a} = 0.2$ - within the chosen design space (left), for a small $\hat{P}$ (right)

Comparing Figures 3.9-3.11, results are shown to be similar to three point bending. Aside from the fewer optimal beam designs occurring within the indentation failure region, the main difference for four point bending is that the mass index for optimal beams is predicted to be smaller. Within the microbuckling and indention failure regions, the same $\bar{t}_{MMT}$ is used for three point bending, so the drop in mass index is attributed to an increase in beam length. For the boundary lines, the drop in mass index may be attributed to changes in all three beam dimensions.

To consider the full range of possible of $\bar{a}$, Figure 3.12 is a failure mechanism map GFRP/ROHACELL 51-IG beams, comparing the failure region boundary lines for $\bar{a} = [0.05, 0.1, 0.2, 0.5, 0.75]$.

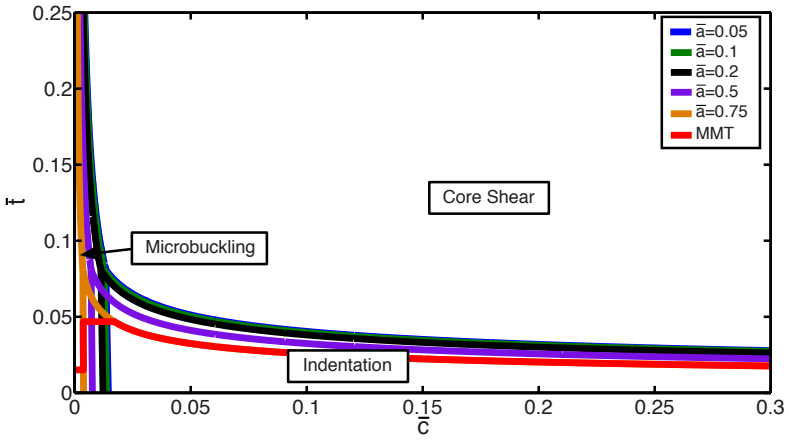

Figure 3.12: Failure mechanism map for a simply supported composite sandwich beam subject to four point bending, GFRP face sheets and ROHACELL 51-IG foam core - Varied $\bar{a}$

Figure 3.13 plots the $\hat{M} - \hat{P}$ curves for varying $\bar{a}$ below.

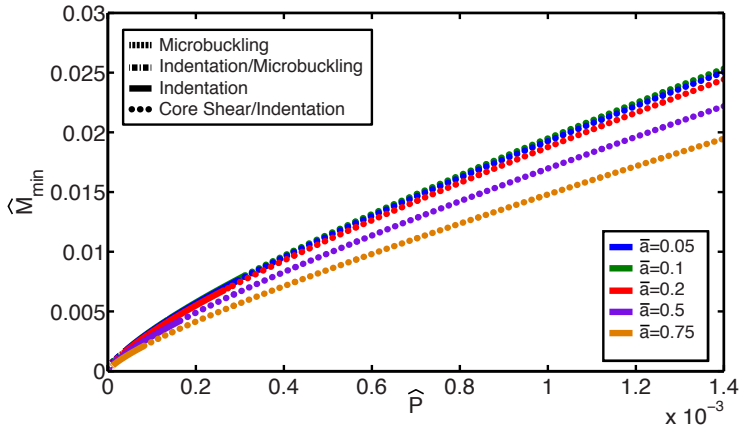

Figure 3.13: Plot of minimum mass trajectory in terms of mass to load index for simply supported composite beams subject to four point bending, GFRP face sheets and ROHACELL 51-IG foam core - varied $\bar{a}$

Seen above, as the load spacing becomes large in relation to the beam length, the decrease in mass index and $\bar{c}$ becomes more significant.

By adapting similar methods from three point bending, a new set of strength and stiffness equations are derived for four point bending. Though failure mechanism maps show similarities to three point bending, microbuckling and indentation failure regions are less dominant. By increasing load spacing factor $\bar{a}$, optimal beam designs of similar load index become more compliant, yielding a lower mass index.

3.2 Case B: Uniformly Distributed Load Case

For uniformly distributed loading, the applied load is replaced by a pressure $w = P/bL$, applied over the beam span (not the overhang), seen in Figure 3.14.

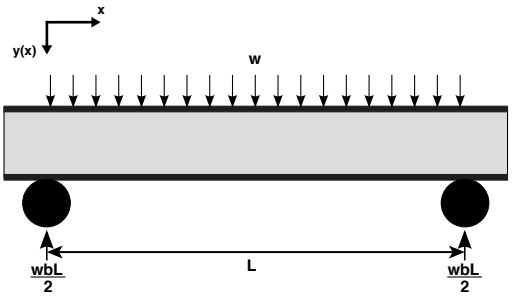

Figure 3.14: A simply supported composite sandwich beam subject to uniformly distributed loading

Figure 3.15 compares shear and bending moment diagrams for the following case.

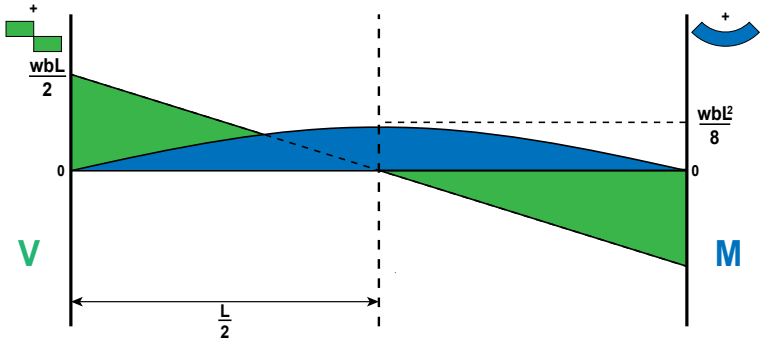

Figure 3.15: Shear and bending moment diagrams for a simply supported composite sandwich subject to uniformly distributed loading

3.2.1 Stiffness

Similar to the point loading cases, deflection is the sum of bending and shear stiffness components:

$$\delta = \delta_b + \delta_s. \tag{3.51}$$

The bending stiffness component deflection equation for the uniformly distributed loading case starts with

$$wb = dV dx = -EI\frac{d^4y}{dx^4}. \tag{3.52}$$

To solve for the expression, the following boundary conditions are used:

- Deflection at the end support is zero, $y(0) = 0$
- Bending moment at the end support is zero, $d^2y(0)/dx^2 = 0$
- Midspan slope is zero, $dy(L/2)/dx = 0$
- No shear across the beam, $d^3y(L/2)/dx^3 = 0$

The resultant deflection equation from bending is

$$y(x) = \frac{wbx}{24EI}(L^3 - 2Lx^2 + x^3), \tag{3.53}$$

where at the midspan, the deflection is

$$\delta_b = \frac{5wbL^4}{384EI}. \tag{3.54}$$

Taking into account the shear component of deflection

$$\delta_s = \left(\frac{wbL}{2}\right)\left(\frac{L}{2AG}\right) = \frac{wbL^2}{4AG}, \tag{3.55}$$

therefore, the total deflection for a simply supported sandwich composite beam is

$$\delta = \frac{5wbL^4}{384EI} + \frac{wbL^2}{4AG}, \tag{3.56}$$

where in terms of stiffness

$$\frac{w}{\delta} = \left[\frac{384(EI)_{eq}(AG)_{eq}}{96(EI)_{eq} + 5(AG)_{eq}L^2}\right]. \tag{3.57}$$

3.2.2 Strength

For uniformly distributed loading, the predicted failure mechanisms are microbuckling, core shear, indentation and core crushing.

Failure Mechanism #1: Microbuckling

From Figure (3.14) above, the maximum bending moment M is $wbL^2/8$. Recalling the bending stress equation from Equation (3.14),

$$\sigma_f = \frac{wL^2}{8td}. \tag{3.58}$$

Therefore the expression for predicting microbuckling in the case of a simply supported uniformly distributed load is

$$w_{MB} = \frac{8td\sigma_f}{L^2}. \tag{3.59}$$

Failure Mechanism #2: Core Shear

From Figure 3.14, the maximum shear load is $wbL/2$. Therefore, the core shear failure expression for uniformly distributed loading is

$$w_{CS} = \frac{2\tau_c d}{L}. \tag{3.60}$$

Failure Mechanism #3: Core Crush

Recalling work from Chapter 2, the core crushing peak pressure is equal to the compressive strength of the core

$$w_{CC} = \sigma_c. \tag{3.61}$$

Failure Mechanism #4: Indentation

Though indentation is generally considered as point load failure mechanism, it is of interest to determine its feasibility for a uniformly distributed load. The following indentation model assumes the corresponding localized core collapse occurs at the midspan of the beam.

Recalling Hetenyi [16], consider an elastic beam of infinite length resting on a foundation material, now subject to a transverse pressure w.

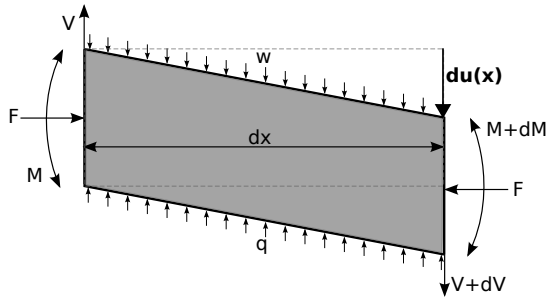

Figure 3.16: Free body diagram for an infinitely small section of a simply supported elastic beam, subject to uniformly distributed load

Taking moments around the left side of the element, equilibrium is

$$M - (M + dM) + (V + dV)dx + (w - \sigma_c)bdx^2 + F\frac{du}{dx}dx = 0, \tag{3.62}$$

where:

$$\frac{dV}{dx} = \frac{q - w}{2}. \tag{3.63}$$

Both the rigid-ideally plastic and elastic-ideally plastic foundations are analyzed.

Rigid-Ideally Plastic Core

To reiterate, in the case of the rigid-ideally plastic core case, the reaction pressure $q = \sigma_c$. Differentiating the expression yields the non-homogenous expression

$$\frac{d^4u}{dx^4} + \frac{F}{EI}\frac{d^2u}{dx^2} = \frac{w - \sigma_c}{2EI}. \tag{3.64}$$

Solving for the homogeneous left hand side of the expression yields the same $k = \sqrt{F/EI}$. However, the particular solution of the expression is only true when

$$u(x) = A_1 cos(kx) + A_2 sin(kx) + A_3 x + A_4 - \frac{(w - \sigma_c)bx^2}{4F}. \tag{3.65}$$

To solve for constants A_1, A_2, A_3 and A_4, the following boundary conditions are set:

- Slope at the beam at the midspan is zero, $u'(0) = 0$
- The shear component of u(x) is zero for pressure loading $u'''(0) = 0$
- $u(\lambda) = 0$
- $u'(\lambda) = 0$
- $u''(\lambda) = 0$

With the shear component of $u(0)$ at zero, constant A_2 is eliminated, thus simplifying the equation to

$$u(x) = \frac{(w - \sigma_c)b}{2Fk^2}\left[\frac{cos(kx)}{cos\mu} - 1 - \frac{\mu^2}{2}\right], \tag{3.66}$$

where at $u(0)$,

$$u(0) = u_{max} = -\frac{(w - \sigma_c)b}{2Fk^2}\left[1 + \frac{\mu^2}{2}\right] = \left[\frac{\sigma_c}{w^2} - \frac{1}{w}\right]\frac{2\pi E_f b^2 t d^4}{L^4}. \tag{3.67}$$

Solving for $du(0)/dw$ yields

$$u'(\lambda) = \frac{(w-\sigma_c)b}{2Fk^2}\left(\frac{-ksin\mu}{cos\mu}\right) = 0, \tag{3.68}$$

where for $\mu \approx \pi$,

$$w_{min} = \sigma_c = w_{CC}. \tag{3.69}$$

As Equation (3.71) is the equivalent of core crush, indentation cannot occur when a rigid-ideally plastic core is employed.

Elastic-Ideally Plastic Core

For an initially elastic core, the reaction pressure is $q = su(x)$, where s is foundation modulus of the core ($s = E_c/c$). When the indentation exceeds a critical point ($u_c = \sigma_c/E_c$), the indentation follows the traits of plastic collapse. For now, only the initial elastic indentation is of concern. Replacing the elastic expression for q for Equation 3.64 the expression for $u(x)$ becomes:

$$\frac{d^4u}{dx^4} + \frac{F}{EI}\frac{d^2u}{dx^2} + \frac{su(x)}{2EI} = \frac{w}{2EI} \tag{3.70}$$

With the addition of a $u(x)$ term to the homogenous portion of the following expression, the particular solution changes from above. Solving for $u(x)$ yields

$$u(x) = (B_1e^{\beta x} + B_2e^{-\beta x})cos(\alpha x) + (B_3e^{\beta x} + B_4e^{-\beta x})sin(\alpha x) + w/s, \tag{3.71}$$

where

$$\alpha^2 = \frac{F}{4EI} + \left(\frac{s}{8EI}\right)^{1/2};\ \beta^2 = -\frac{F}{4EI} + \left(\frac{s}{8EI}\right)^{1/2}. \tag{3.72}$$

Assuming the same slope, bending moment and shear boundary conditions as from the rigid-ideally plastic core case, Equation (3.71) becomes

$$u(x) = Bcos(\alpha x) + w/s, \tag{3.73}$$

where B is an indeterminate constant. As core indentation is indeterminate within the elastic region, a plastic collapse can never be attained. Indentation is instead a purely elastic response of the core from a buckling of the top face sheet, given by

$$F_{cr} = 2\sqrt{sb(EI)_{eq}} \tag{3.74}$$

where the indent size is equal to the beam length.

For this case, the peak pressure before failure is

$$w_I = \sqrt{\frac{128 E_f E_c t^3 d}{c L^4}}. \tag{3.75}$$

Failure Mechanism Mapping

Using the same non-dimensional relationships from Chapter 2, failure expressions for uniformly distributed loading are defined as:

$$\hat{w}_{MB} = 8\bar{t}(\bar{t}+1)\bar{c}^2\phi, \tag{3.76}$$

$$\hat{w}_{CS} = 2\bar{\tau}(\bar{t}+1)\bar{c}, \tag{3.77}$$

$$\hat{w}_{CC} = \bar{\sigma}, \tag{3.78}$$

and

$$\hat{w}_I = \sqrt{128 \bar{E}_f \bar{E}_c \bar{t}^3 (\bar{t}+1)^2 \bar{c}^4} \tag{3.79}$$

where $\hat{w}$ defines the peak pressure index.

Figures 3.17-3.20 plot the failure mechanism maps for simply supported beams subject to a uniformly distributed load for the same material selections as the previous two cases.

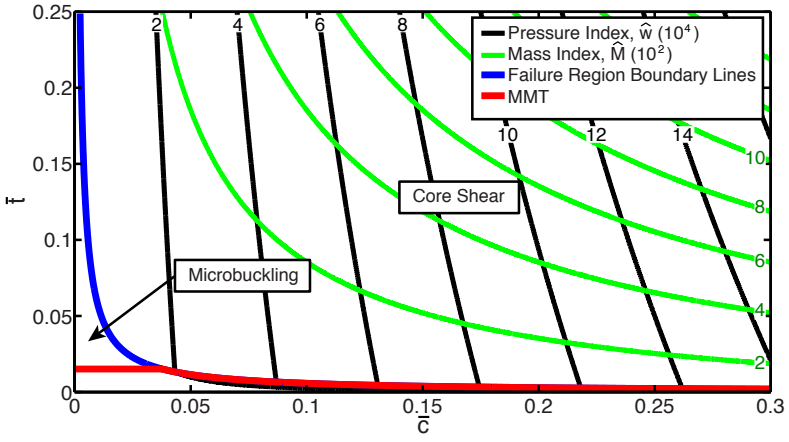

Figure 3.17: Failure mechanism map for a simply supported composite sandwich beam subject to uniformly distributed loading, GFRP face sheets and ROHACELL 51-IG foam core, comparing non-dimensional contour plots of load and mass, dividing regions of active failure mechanism and predicting minimum mass trajectory (in red)

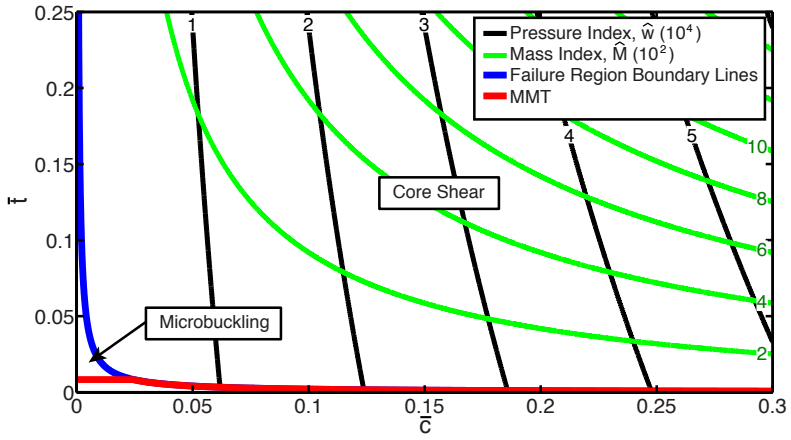

Figure 3.18: Failure mechanism map for a simply supported composite sandwich beam subject to uniformly distributed loading, GFRP face sheets and extruded polystyrene (EPS) foam core comparing non-dimensional contour plots of load and mass, dividing regions of active failure mechanism and predicting minimum mass trajectory (in red)

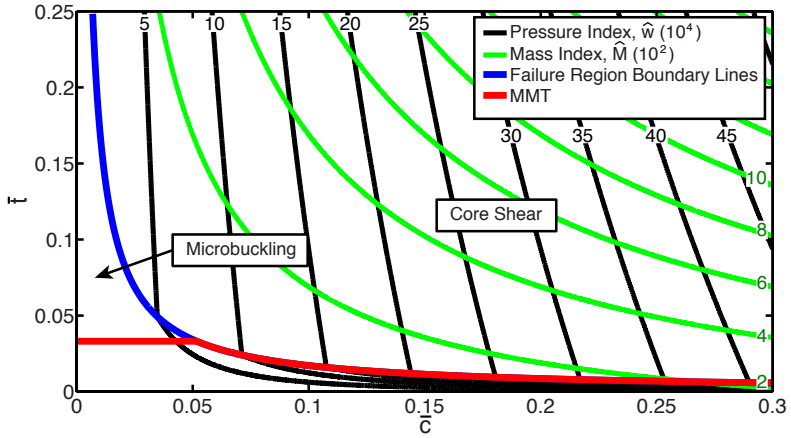

Figure 3.19: Failure mechanism map for a simply supported composite sandwich beam subject to uniformly distributed loading, GFRP face sheets and ROHACELL 110-IG foam core, comparing non-dimensional contour plots of load and mass, dividing regions of active failure mechanism and predicting minimum mass trajectory (in red)

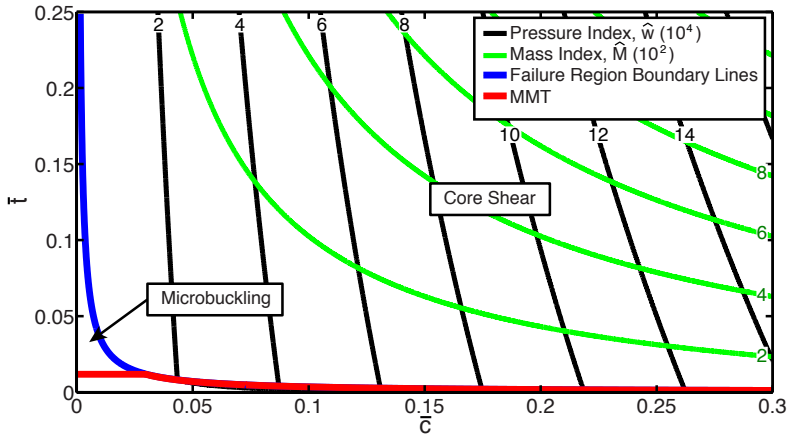

Figure 3.20: Failure mechanism map for a simply supported composite sandwich beam subject to uniformly distributed loading, CFRP face sheets and ROHACELL 51-IG foam core, comparing non-dimensional contour plots of load and mass, dividing regions of active failure mechanism and predicting minimum mass trajectory (in red)

Solving for each design space, only two of the four competing failure mechanisms are present: microbuckling and core shear. Microbuckling occurs in cases of small $\bar{c}$, while core shear is the dominant failure region in cases of higher $\bar{c}$. A stronger face sheet compressive strength or weaker core shear strength results in a larger core shear failure region.

The boundary line equations are:

i) Microbuckling/Core Shear

$$\bar{t} = \frac{\bar{\tau}}{4\bar{c}\phi} \tag{3.80}$$

ii) Core Shear/Indentation

$$\bar{t} = \left[\frac{3\bar{\tau}^2}{32\bar{E}_f\bar{E}_c\bar{c}^2}\right]^{1/3} \tag{3.81}$$

iii) Indentation/Core Crush

$$\bar{t}^3(\bar{t}+1)^2 = \frac{3\bar{\sigma}^2}{128\bar{E}_f\bar{E}_c\bar{c}^4} \tag{3.82}$$

iv) Microbuckling/Core Crush

$$\bar{t}(\bar{t}+1) = \left(\frac{\bar{\sigma}}{8\phi\bar{c}^2}\right)^{1/2} \tag{3.83}$$

v) Indentation/Microbuckling

$$\bar{t} = \frac{3\phi^2}{2\bar{E}_f\bar{E}_c} \quad (\in \bar{c}) \tag{3.84}$$

vi) Core Shear/Core Crush

$$\bar{t} = \frac{\bar{\sigma}}{2\bar{\tau}\bar{c}} - 1 \tag{3.85}$$

vii) Microbuckling/Core Shear/Indentation

$$\bar{t} = \frac{3\phi^2}{2\bar{E}_f\bar{E}_c} \tag{3.86}$$

$$\bar{c} = \frac{\bar{E}_f\bar{E}_c\bar{\tau}}{6\phi^3} \tag{3.87}$$

viii) Core Shear/Indentation/Core Crush

$$\frac{(\bar{t}+1)^2}{\bar{t}^3} = \frac{8\bar{E}_f\bar{E}_c\bar{\sigma}^2}{\bar{\tau}^4} \tag{3.88}$$

$$32\bar{E}_f\bar{E}_c\bar{c}^{*2} - \frac{16\bar{E}_f\bar{E}_c\bar{\sigma}\bar{c}}{3\sqrt{\bar{\tau}}} + 3\bar{\tau} \tag{3.89}$$

ix) Indentation/Core Crush/Microbuckling

$$\bar{t} = \frac{3\phi^2}{2\bar{E}_f\bar{E}_c} \tag{3.90}$$

$$\bar{c} = \left(\frac{\bar{E}_f\bar{E}_c}{3}\right)^3\left(\frac{\bar{\sigma}}{\phi^5}\right)(2\phi^2 + 3\bar{E}_f\bar{E}_c) \tag{3.91}$$

x) Core Crush/Microbuckling/Core Shear

$$\bar{t} = \frac{\bar{\tau}^2}{2\phi\bar{\sigma} - \bar{\tau}^2} \tag{3.92}$$

$$\bar{c} = \frac{2\bar{\sigma}\bar{\tau} - 1}{4\phi\sigma}. \tag{3.93}$$

Feasibility of Core Crush and Indentation Failures

As both indentation and core crush are not present in any of the above failure mechanism maps, it is of interest to determine if the failures can exist at all. For core crushing to exist,

$$\frac{\sigma_c}{\tau_c} < 2(\bar{t}+1)\bar{c}, \tag{3.94}$$

whereby the compressive strength must be less than the required pressure for core shear failure. Considering the maximum limits of the design space ($\bar{c} = 0.30$,$\bar{t} = 0.25$), the compressive strength of the core must be less than 75% of its own shear strength for core crush to exist. Though core crushing is not considered beyond here, it is still feasible to exist if the chosen core material satisfies above strength requirements.

Considering the feasibility of indentation, the easiest failure mechanism to surpass is microbuckling, seen by

$$\frac{2E_f E_c}{3\phi^2} < \frac{c}{t}. \tag{3.95}$$

For indentation to exist, the material properties parameter on the left must be less than the beam geometry parameter to the right. Even considering the largest design space dimensions, the required material properties must still be small. Unless face sheets with properties close to silicone are considered, indentation may be disregarded.

Minimum Mass Trajectory Analysis

For the minimum mass trajectories of uniformly distributed loading, optimal beams either lie within the microbuckling failure region for a set critical $\bar{t}$, where

$$\bar{t}_{MMT} = \frac{\bar{\rho}}{2(1-\bar{\rho})}, \tag{3.96}$$

$$\bar{c}_{MMT} = \left(\frac{(1-\bar{\rho})^2\hat{w}}{2\bar{\rho}(2-\bar{\rho})}\right)^{1/2}, \tag{3.97}$$

and

$$\hat{M} = \left(\frac{\bar{\rho}(2-\bar{\rho})^2\hat{w}}{2\phi(2\psi-\psi\bar{\rho}+\bar{\rho})}\right)^{1/2}, \tag{3.98}$$

or the optimal beam designs lie along the microbuckling/core shear boundary line, where

$$\hat{M} = \frac{(2\psi-\bar{\rho})}{4\phi} + \frac{\bar{\rho}\hat{w}}{2\bar{\tau}}. \tag{3.99}$$

Comparing the minimum mass trajectories from Figures 3.16-3.20, Figure 3.21 compares beam geometry variables $\bar{t}$ to $\bar{c}$ to the peak pressure index, while Figure 3.22 plots the resultant minimum mass index to peak pressure index.

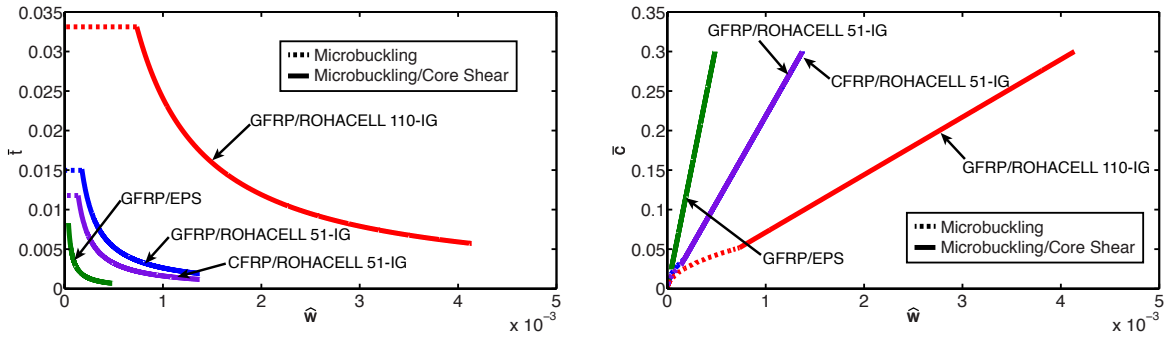

Figure 3.21: Plot of minimum mass trajectory in terms of $\bar{t}$ to peak pressure index for simply supported composite beams subject to uniform loading

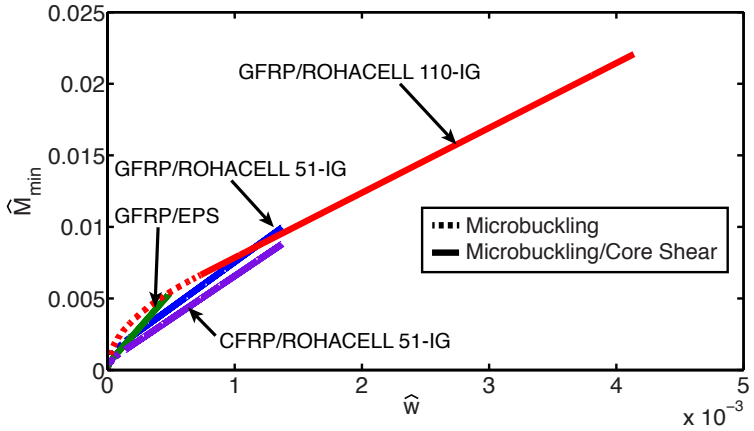

Figure 3.22: Plot of minimum mass trajectory in terms of mass to peak pressure index for simply supported composite beams subject to uniform loading

As the dominant failure region for uniform loading is core shear, considering a stronger core material has a significant effect on the range of possible $\hat{w}$. Though the proportionality of microbuckling and microbuckling-core shear optimal beam designs are subject to change, the difference that occurs in terms of peak pressure index is small.

In summary, a new set of strength and stiffness equations are derived for a simply supported composite beam subject to a uniform pressure. Though four failure mechanisms are considered, only two are likely to exist in general practice: microbuckling and core shear. The dominance of one failure mechanism over the other is dependant on core shear strength and face sheet compressive strength.

3.3 Stiffness Constraint

In engineering practice, compliant beams are undesirable due to their excessive deflection. To omit the design points that fall below a target stiffness, a stiffness constraint is implemented.

3.3.1 Three Point Bending

Recalling Chapter 2, beam stiffness is defined by P/δ. To impose a stiffness constraint, a fourth failure mechanism is derived by rewriting the beam stiffness equation for three point bending from Equation (2.2)

$$P = \left[\frac{48(EI)_{eq}(AG)_{eq}}{12(EI)_{eq} + (AG)_{eq}L^2}\right]\delta. \tag{3.100}$$

Converting the above expression into non-dimensional terms,

$$\hat{P} = \left[\frac{48\hat{EI}\hat{AG}}{12\hat{EI} + \hat{AG}}\right]\hat{\delta} \tag{3.101}$$

where

$$\hat{EI} = \frac{\bar{E}_f\bar{t}(\bar{t}+1)^2\bar{c}^3}{2} \tag{3.102}$$

and

$$\hat{AG} = \bar{G}_c(\bar{t}+1)\bar{c}. \tag{3.103}$$

Seen in Equation (3.101), the driving force behind an imposed stiffness constraint is $\hat{\delta}$, the ratio of failure deflection over beam length ($\hat{\delta} = \delta/L$). Beams are considered to have failed if deflection at the predicted peak load exceeds the maximum allowable deflection. For now, the range of $\hat{\delta} = [0.015, 0.02, 0.025, 0.05, 0.1]$ or $\hat{\delta} = [1.5\%, 2.0\%, 2.5\%, 5.0\%, 10.0\%]$ is investigated here.

Figure 3.23 plots the failure mechanism map for three point bending including the stiffness constraint. Only the boundary lines for each failure region are shown, as the mass and load index contour lines do not change from GFRP/ROHACELL 51-IG plot in Figure 2.7.

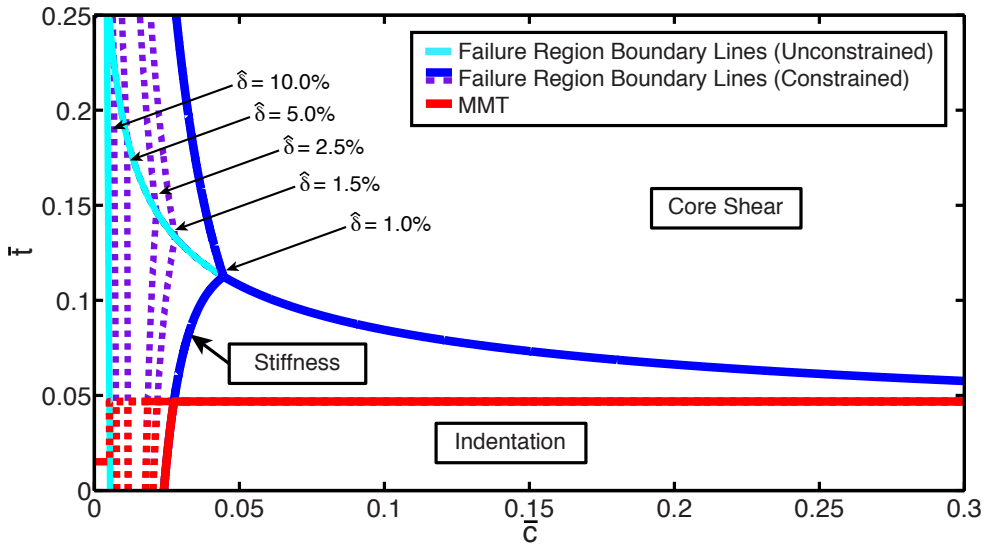

Figure 3.23: Failure mechanism map for a simply supported composite beam subject to three point bending, GFRP face sheets and ROHACELL 51-IG foam core - varied stiffness constraint, defined by $\hat{\delta}$

Below are the accompanying boundary lines related to stiffness for the three point bending model. The expressions are in terms of normalized equivalent bending and shear stiffness terms $\hat{EI}$ and $\hat{AG}$:

i) Microbuckling/Stiffness

$$\bar{t}(\bar{t}+1) = \left[\left(\frac{48\hat{EI}\hat{AG}}{12\hat{EI}+\hat{AG}}\right)\left(\frac{\hat{\delta}}{4\bar{c}^2\phi}\right)\right] \tag{3.104}$$

ii) Core Shear/Stiffness

$$\bar{t} = \left(\frac{48\hat{EI}\hat{AG}}{12\hat{EI}+\hat{AG}}\right)\frac{\hat{\delta}}{2\bar{\tau}\bar{c}} - 1 \tag{3.105}$$

iii) Indentation/Stiffness

$$\bar{t}^3(\bar{t}+1) = \left(\frac{48\hat{EI}\hat{AG}\hat{\delta}}{12\hat{EI}+\hat{AG}}\right)^{1/3}\left(\frac{3}{\pi^2\bar{\sigma}^2\bar{E}_f\bar{c}^4}\right) \tag{3.106}$$

iv) Microbuckling/Core Shear/Stiffness

$$\frac{(\bar{t}+1)}{\bar{t}} = \left(\frac{48\hat{EI}\hat{AG}}{12\hat{EI}+\hat{AG}}\right)\frac{\hat{\delta}}{\phi} \tag{3.107}$$

$$\bar{c} = \left(\frac{48\hat{EI}\hat{AG}}{12\hat{EI}+\hat{AG}}\right)\frac{\hat{\delta}}{2\bar{\tau}} - \frac{\bar{\tau}}{2\phi} \tag{3.108}$$

v) Core Shear/Indentation/Stiffness

$$\frac{(\bar{t}+1)^2}{\bar{t}^3} = \frac{2\hat{E}I\hat{A}G\hat{\delta}\pi^2\bar{\sigma}^2\bar{E}_f}{(12\hat{E}I+\hat{A}G)\bar{\tau}} \tag{3.109}$$

$$\left(\frac{48\hat{E}I\hat{A}G}{12\hat{E}I+\hat{A}G}\right)\frac{\hat{\delta}\bar{c}^3}{2\bar{\tau}} - \frac{3}{\pi^2\bar{\sigma}^2\bar{E}_f}\left(\frac{12\hat{E}I+\hat{A}G}{48\hat{E}I\hat{A}G}\right)^{2/3} + \bar{c}^4 \tag{3.110}$$

vi) Indentation/Microbuckling/Stiffness

$$\bar{t} = \left[\pi^2\bar{\sigma}^2\bar{E}_f\phi\left(\frac{2304\hat{E}I\hat{A}G\bar{\delta}}{12\hat{E}I+\hat{A}G}\right) - 1\right]^{-1} \tag{3.111}$$

$$\left(\frac{\pi^2\bar{\sigma}^2\bar{E}_f\bar{c}^*}{192\phi}\right)^{1/2} - \bar{c} = \left(\frac{2304\hat{E}I\hat{A}G\bar{\delta}}{12\hat{E}I+\hat{A}G}\right). \tag{3.112}$$

A point where all failure mechanisms boundaries intersect is a function of the material properties of the beam.

For larger deflection ratios (ie. 10%), the imposed stiffness constraint rules out a small fraction of the failure mechanism map design space. Every incremental decrease of the deflection ratio limit thereafter expands this territory. For the GFRP/ROHACELL 51-IG case, even with a 10% deflection ratio limit, beam designs that are predicted to fail by microbuckling are ruled out. Thus, the failure mechanisms that should realistically be considered for the following material case are core shear and indentation.

Figures 3.24 and 3.25 compare the constrained minimum mass trajectory from each deflection ratio limit through $\bar{t} - \hat{P}$ and $\bar{c} - \hat{P}$ plots respectively.

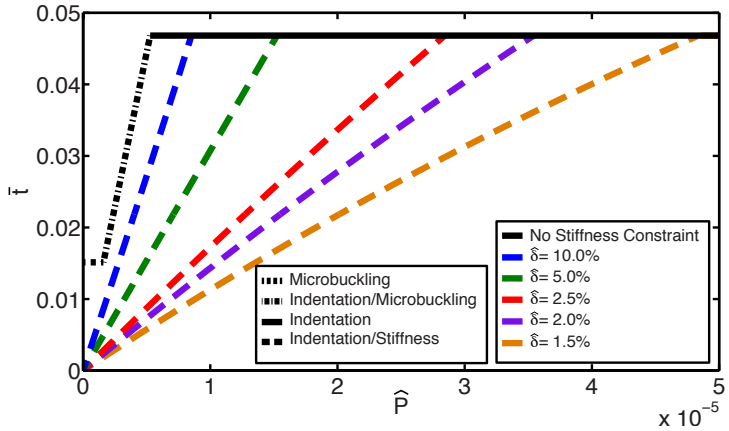

Figure 3.24: Plot of minimum mass trajectory in terms of $\bar{t}$ to load index for simply supported composite beams subject to three point bending, GFRP face sheets and ROHACELL 51-IG foam core - varied stiffness constraint, defined by $\hat{\delta}$, $\hat{P} \leq 5x10-5$

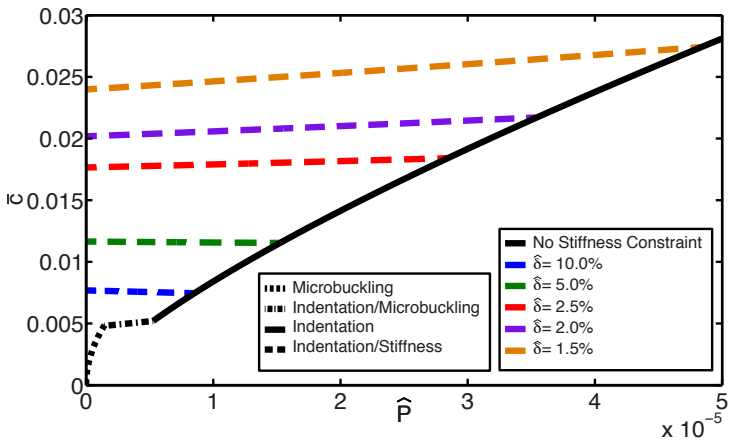

Figure 3.25: Plot of minimum mass trajectory in terms of $\bar{c}$ (right) to load index for simply supported composite beams subject to three point bending, GFRP face sheets and ROHACELL 51-IG foam core - varied stiffness constraint, defined by $\hat{\delta}$, $\hat{P} \leq 5x10 - 5$

As the maximum allowable deflection is constrained, optimal beams show a rise in $\bar{c}$ and drop in $\bar{t}$, meaning beams are recommended to be designed with a thicker core relative to face sheet thickness and beam length.

Figure 3.26 compares the mass index of the constrained minimum mass trajectory, varying $\hat{\delta}$.

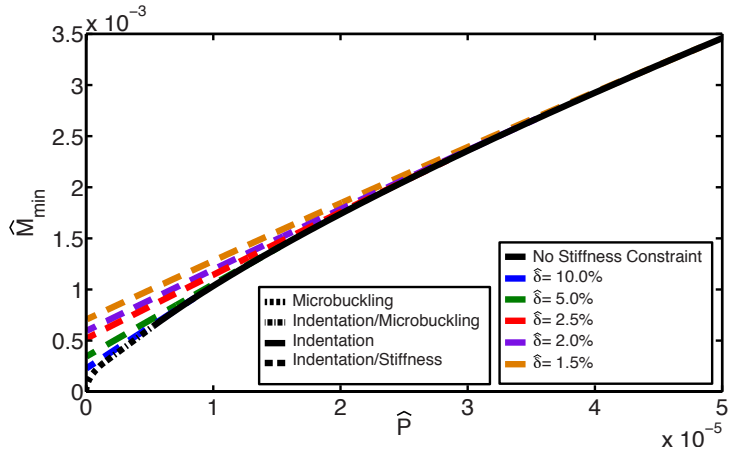

Figure 3.26: Plot of minimum mass trajectory in terms of mass index to load index for simply supported composite beams subject to three point bending, GFRP face sheets and ROHACELL 51-IG foam core - varied stiffness constraint, defined by $\hat{\delta}$, $\hat{P} \leq 5x10 - 5$

As the deflection ratio limit decreases the mass index rises.

3.3.2 Four Point Bending

Next, four point bending is considered, where:

$$\frac{\hat{P}}{\hat{\delta}} = \frac{96\hat{E}I\hat{A}G}{24(1-\bar{a})\hat{E}I + (1-\bar{a})(3-(1-\bar{a})^2)\hat{A}G} \tag{3.113}$$

and the supporting boundary line equations are:

i) Microbuckling/Stiffness

$$\bar{t}(\bar{t}+1) = \frac{24\hat{E}I\hat{A}G\hat{\delta}}{(24\hat{E}I + (3-(1-\bar{a})^2)\hat{A}G)\phi\bar{c}^2} \tag{3.114}$$

ii) Core Shear/Stiffness

$$\bar{t}(\bar{t}+1) = \left(\frac{48\hat{E}I\hat{A}G}{24\hat{E}I + (3-(1-\bar{a})^2)\hat{A}G}\right)\frac{\hat{\delta}}{(1-\bar{a})\bar{c}}, \tag{3.115}$$

iii) Indentation/Stiffness

$$\bar{t}^3(\bar{t}+1) = \left(\frac{48\hat{E}I\hat{A}G\hat{\delta}}{24\hat{E}I + (3-(1-\bar{a})^2)\hat{A}G}\right)^3\left(\frac{3}{\bar{E}_f\bar{,}\sigma^2\pi^2(1-\bar{a})^2\bar{c}^4}\right) \tag{3.116}$$

iv) Microbuckling/Core Shear/Stiffness

$$\frac{(\bar{t}+1)}{\bar{t}} = \frac{\bar{\phi}\hat{\delta}}{((1-\bar{a})\bar{\tau})^2}\left[\frac{96\hat{E}I\hat{A}G}{24\hat{E}I + (3-(1-\bar{a})^2)\hat{A}G}\right] \tag{3.117}$$

$$\bar{c}^* = \left[\frac{48\hat{E}I\hat{A}G}{24\hat{E}I + (3-(1-\bar{a})^2)\hat{A}G}\right]\frac{\hat{\delta}}{\bar{\tau}(1-\bar{a})} - \frac{\bar{\tau}(1-\bar{a})}{2\phi} \tag{3.118}$$

v) Core Shear/Indentation/Stiffness

$$\frac{(\bar{t}+1)}{\bar{t}} = \left[\frac{16\pi^2\bar{\sigma}^2\bar{E}_f\hat{E}I\hat{A}G\hat{\delta}}{(1-\bar{a})\bar{\tau}^4(\hat{A}G(3-(1-\bar{a})^2) + 24\hat{E}I)}\right]^{1/3} \tag{3.119}$$

$$(-1+\sqrt{1-4A})^3\left[\left(\frac{-1+\sqrt{1-4A}}{2}\right)+1\right] = \left(\frac{96\hat{E}I\hat{A}G}{24\hat{E}I + (3-(1-\bar{a})^2)\hat{A}G}\right)^3\left(\frac{3}{\bar{E}_f\bar{\sigma}^2\pi^2(1-\bar{a})^2\bar{c}^4}\right) \tag{3.120}$$

where:

$$A = \left(\frac{48\hat{E}I\hat{A}G}{24\hat{E}I + (3-(1-\bar{a})^2)\hat{A}G}\right)\frac{\hat{\delta}}{(1-\bar{a})\bar{\tau}\bar{c}} \tag{3.121}$$

vi) Indentation/Microbuckling/Stiffness

$$\frac{\bar{t}}{(\bar{t}+1)} = \frac{24\phi}{\bar{\sigma}\pi(1-\bar{a})}\left(\frac{\hat{EI}\hat{AG}\hat{\delta}}{\bar{E}_f(\hat{AG}(3-(1-\bar{a})^2)+24\hat{EI})}\right) \tag{3.122}$$

$$\left(\frac{\bar{E}_f}{48\phi^3}\left(\frac{\bar{\sigma}(1-\bar{a})}{\bar{c}}\right)^2 - 1\right)^2 = \frac{\hat{EI}\hat{AG}\hat{\delta}\phi^5}{(\hat{AG}(3-(1-\bar{a})^2+24\hat{EI})}\left(\frac{24\bar{c}}{\bar{E}_f\bar{\sigma}^2\pi^2(1-\bar{a})^2}\right)^2. \tag{3.123}$$

Figure 3.27 is the failure mechnanism map for simply supported GFRP/ROHACELL 51-IG beams subject to four point bending, $\bar{a} = 0.2$.

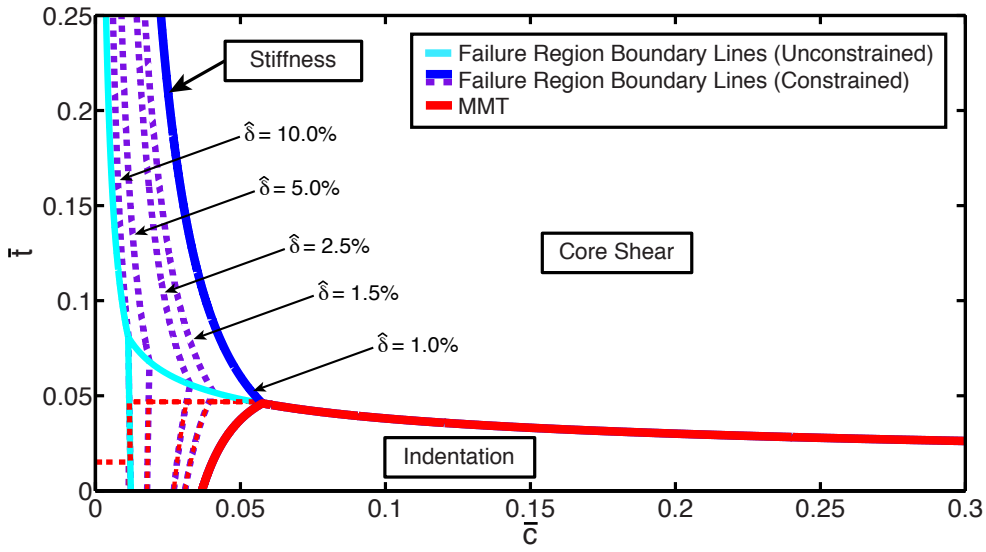

Figure 3.27: Failure mechanism map for a simply supported composite beam subject to four point bending, GFRP face sheets and ROHACELL 51-IG foam core - varied stiffness constraint, defined by $\hat{\delta}$, $\bar{a} = 0.2$

Similarly to three point bending, microbuckling is not feasible. As the deflection ratio limit decreases, the minimum mass trajectory eventually becomes comprised of boundary line design points.

To compare, Figures 3.28 and 3.29 show the $\bar{t} - \hat{P}$ and $\bar{c} - \hat{P}$ plots with a varied stiffness constraint, while Figure 3.30 shows the resultant mass index to peak load plot.

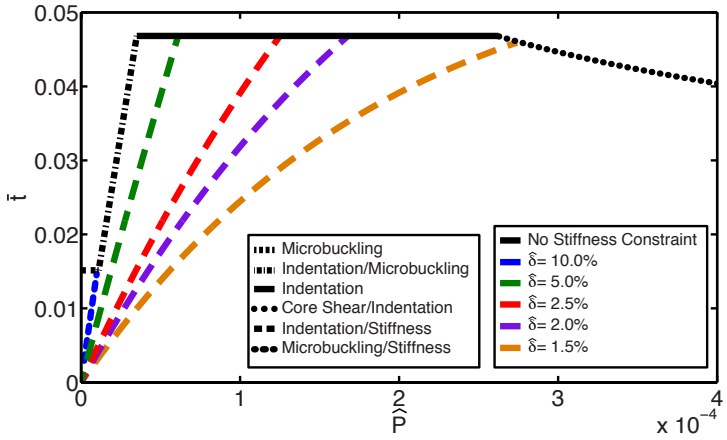

Figure 3.28: Plot of minimum mass trajectory in terms of $\bar{t}$ to load index for simply supported composite beams subject to four point bending, GFRP face sheets and ROHACELL 51-IG foam core, $\bar{a} = 0.2$ - varied stiffness constraint, defined by $\hat{\delta}$, $\hat{P} \leq 4x10 - 5$

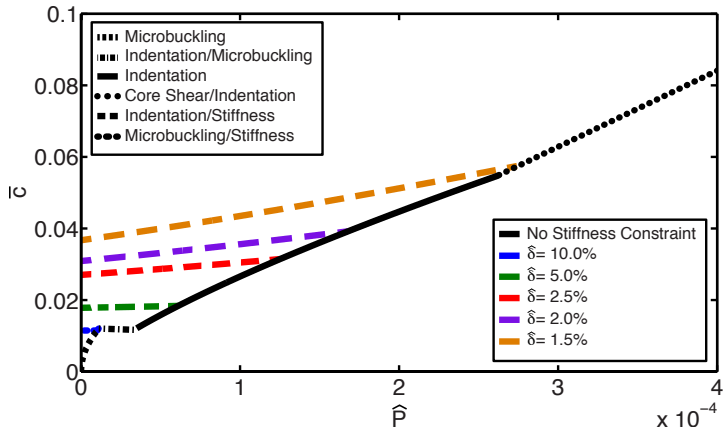

Figure 3.29: Plot of minimum mass trajectory in terms of $\bar{c}$ to load index for simply supported composite beams subject to four point bending, GFRP face sheets and ROHACELL 51-IG foam core, $\bar{a} = 0.2$ - varied stiffness constraint, defined by $\hat{\delta}$, $\hat{P} \leq 4x10 - 5$

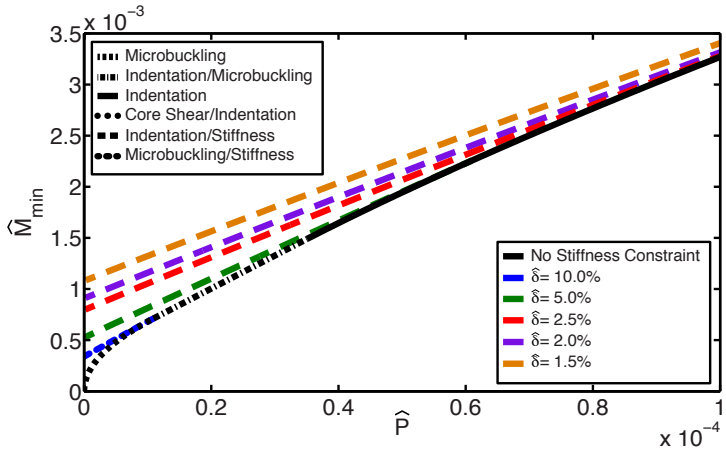

Figure 3.30: Plot of minimum mass trajectory in terms of mass index to load index for simply supported composite beams subject to four point bending, GFRP face sheets and ROHACELL 51-IG foam core, $\bar{a} = 0.2$ - varied stiffness constraint, defined by $\hat{\delta}$, $\hat{P} \leq 1x10-4$

As the design space is further constrained by stiffness in the indentation region, the minimum allowed core thickness increases. As stiffness further constrains the minimum mass trajectory along the core shear/indentation boundary line, $\bar{t}$ is suppressed to a smaller maximum value.

3.3.3 Uniformly Distributed Loading

For the third and final case, the effect of stiffness is studied on uniformly distributed loading. For this case, the stiffness constraint, now $\hat{w}/\hat{\delta}$ is defined by

$$\frac{\hat{w}}{\hat{\delta}} = \frac{384\hat{EI}\hat{AG}}{5\hat{AG} + 96\hat{EI}}. \tag{3.124}$$

Below are the respective equations required for failure mechanism mapping, with the addition of a stiffness constraint.

i) Stiffness/Microbuckling

$$\bar{t}(\bar{t}+1) = \left(\frac{48\hat{EI}\hat{AG}}{5\hat{AG} + 96\hat{EI}}\right)\frac{\hat{\delta}}{\phi\bar{c}^2} \tag{3.125}$$

ii) Core Shear/Stiffness

$$\bar{t} = \left(\frac{192\hat{EI}\hat{AG}}{5\hat{AG} + 96\hat{EI}}\right)\frac{\hat{\delta}}{\bar{\tau}\bar{c}} - 1 \tag{3.126}$$

v) Microbuckling/Core Shear/Stiffness

$$\frac{(\bar{t}+1)}{\bar{t}} = \left(\frac{3072\hat{EI}\hat{AG}}{5\hat{AG} + 96\hat{EI}}\right)\frac{\phi\bar{\delta}}{\bar{\tau}^2} \tag{3.127}$$

$$\bar{c} = \left(\frac{384\hat{EI}\hat{AG}}{5\hat{AG} + 96\hat{EI}}\right)\frac{\bar{\delta}}{\bar{\tau}} - \frac{\bar{\tau}}{8\phi} \tag{3.128}$$

Figure 3.31 is the modified failure mechanism map of uniformly distributed loading for simply supported GFRP/ROHACELL 51-IG beams, under varying stiffness constraints.

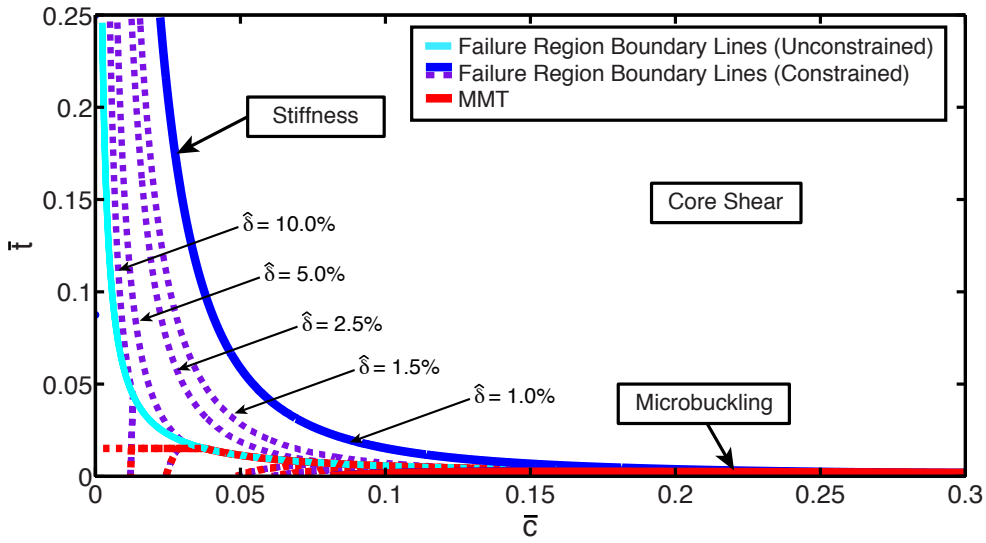

Figure 3.31: Failure mechanism map for a simply supported composite beam subject to uniformly distributed loading, GFRP face sheets and ROHACELL 51-IG foam core - varied stiffness constraint, defined by $\hat{\delta}$

By imposing a large enough stiffness constraint, microbuckling may be ruled out for the uniform loading case as well. Figures 3.32-3.34 plot $\bar{t}$, $\bar{c}$ and mass index of the constrained minimum mass trajectories to pressure index.

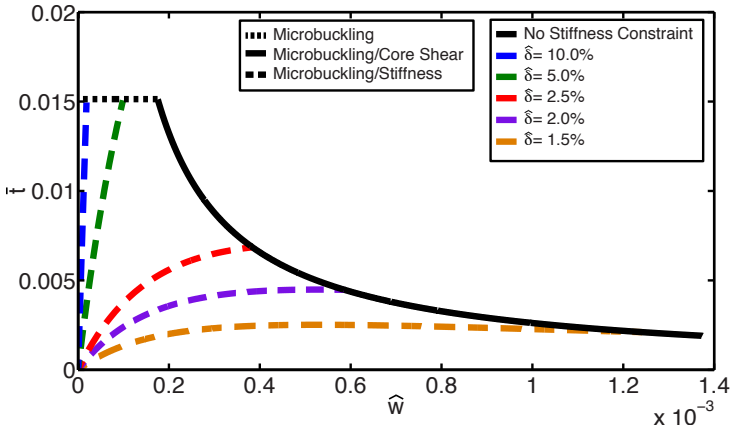

Figure 3.32: Plot of minimum mass trajectory in terms of $\bar{t}$ to load index for simply supported composite beams subject to uniformly distributed loading, GFRP face sheets and ROHACELL 51-IG foam core - varied stiffness constraint, defined by $\hat{\delta}$

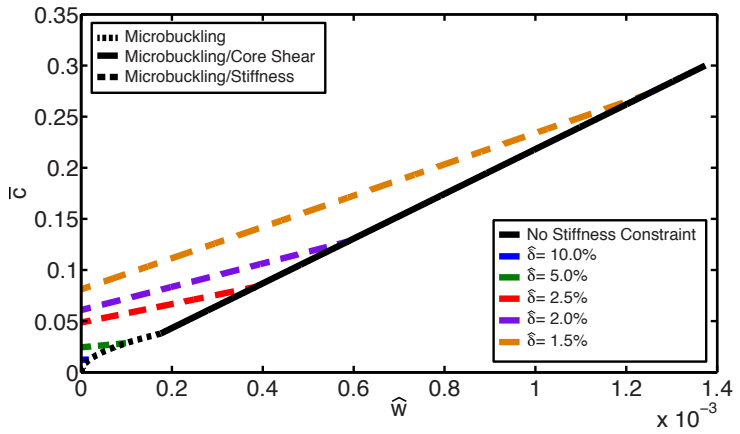

Figure 3.33: Plot of minimum mass trajectory in terms of $\bar{c}$ (right) to load index for simply supported composite beams subject to uniformly distributed loading, GFRP face sheets and ROHACELL 51-IG foam core - varied stiffness constraint, defined by $\hat{\delta}$

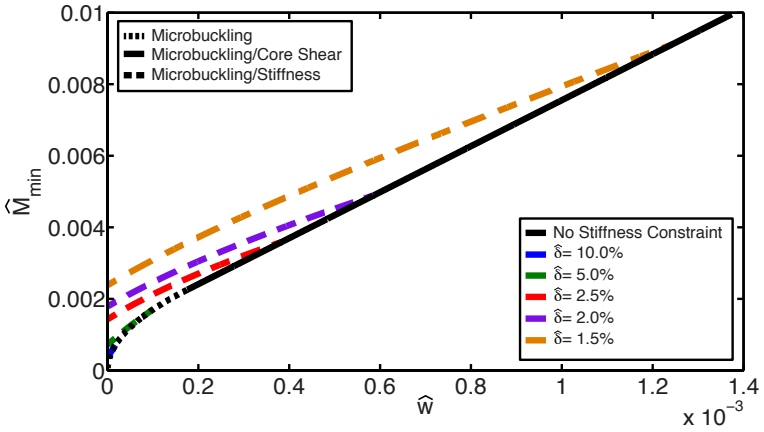

Figure 3.34: Plot of minimum mass trajectory in terms of mass index to load index for simply supported composite beams subject to uniformly distributed loading, GFRP face sheets and ROHACELL 51-IG foam core - varied stiffness constraint, defined by $\hat{\delta}$

In the event microbuckling is not feasible, the resultant minimum mass trajectory would be defined by the core shear/stiffness boundary line.

In general, when designing beams to be subject to pressure loading, the only plausible failure mechanism to exist is core shear. Though other failure mechanisms (microbuckling, indentation, core crush) may exist in extreme cases, core shear is the only active failure mechanism that both satisfies stiffness constraints and adheres to realistic material property assumptions.

Through failure mechanism identification and mapping, three point bending, four point bending and uniformly distributed loading are analyzed. To eliminate undesirable beam designs that fail under large deflections, a stiffness constraint is introduced. Only by introducing this constraint, is it determined that microbuckling is infeasible for all loading cases due to its higher compliance.

Chapter 4

Failure Mechanism Map Validation

To validate the stiffness and strength expressions derived in Chapter 3, a series of experiments are conducted. Though the following tests may overlap other work, three loading cases are considered for sake of continuity, allowing for a comparison of results afterward.

Experiments are performed on an MTS 550 Load Frame with a 100kN load cell. Various loading fixtures are installed to complete the required tensile, compressive and bending tests. Figure 4.1 is a summary of all loading fixtures used for three point bending, four point bending and uniformly distributed loading tests.

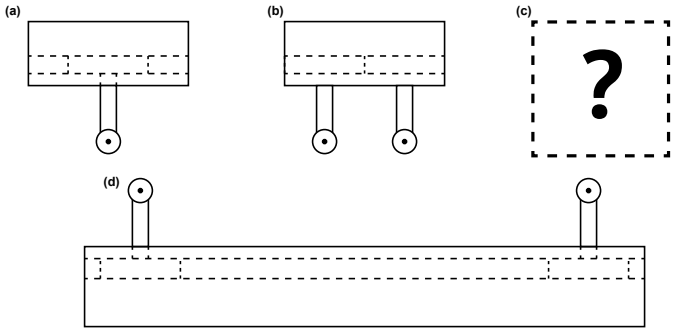

Figure 4.1: Summary of testing apparatus: (a) three point bending, (b) four point bending, (c) uniform loading (d) base unit

All three loading cases utilize the same base unit, Figure 4.1(d), a fully adjustable steel block with removable support arms of 55mm long contact rollers, 25mm in diameter. Governed by a track and set screws, the base unit spans 80-480mm in 20mm intervals. Load fixtures for three and four point bending are based on the same design as the base unit and are installed on the top cylinder of the load frame. As no testing standard currently exists for simply supported uniformly distributed loading testing, an alternate testing fixture is proposed later in the chapter.

4.1 Material Selection and Fabrication

4.1.1 Face Sheet Material - GFRP

Glass fibre reinforced polymer face sheets are constructed from 6oz. BGF plain weave fibreglass cloth [4], Huntsman Araldite LY8601 Resin and Aradur 8602 Hardener [18]. To ensure consistent face sheet quality, resin is applied on each glass fibre ply until saturation during the layering process. Face sheets are aligned in $0/90^o$ orientation and cured at room temperature using a vacuum resin infusion unit. During the curing and consolidation process, GFRP sheet thicknesses are reduced by 15%. Therefore, the estimated post-cure thickness of GFRP, t, is 85% of total fabric material.

Tensile tests are conducted on 150mm x 15mm x 3 ply glass fibre ((0.85) x 0.6mm) strips, supported by four aluminum tabs of 5mm. Figure 4.2 is the tensile stress-strain plot from the 50mm x 15mm x 0.51mm GFRP specimen, performed at a strain rate of 0.005mm/s.

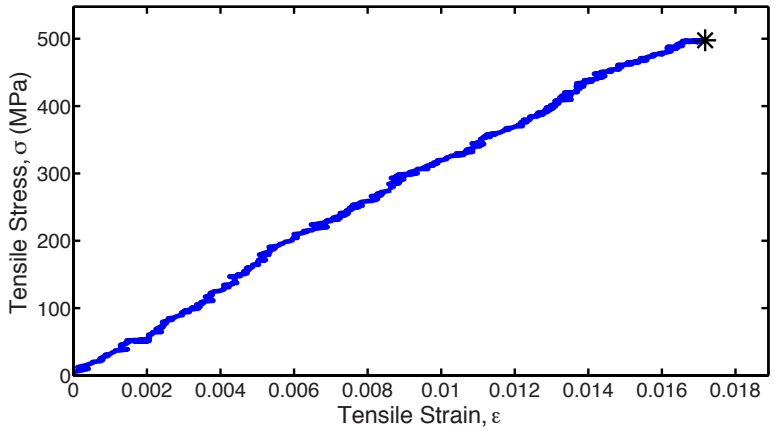

Figure 4.2: Tensile stress-strain plot of GFRP face sheet material

Though it would be ideal determine the corresponding compressive strength through experiments, fibre-reinforced materials require specific testing fixtures for compressive testing (ie. a Celanese compression fixture). As no such testing fixture is available, estimated compressive strength is cited from other works [36].

Table 4.1 summarizes material properties for GFRP.

Table: 4.1 Face sheet material properties - experiment results

Material Property	E-Glass Fibre Reinforced Plastic (GFRP)
Elastic Modulus, E_f (GPa)	31
Compressive Strength, σ_c (kPa)	350 [37]
Density, ρ_f (kg/m^3)	1592

4.1.2 Core Material - ROHACELL 51-IG, Extruded Polystyrene (EPS)

Of the three foams analyzed in previous chapters, two are used for the following experiments: Evonik Industries ROHACELL 51-IG (Industrial Grade) polymethacrylimide foam, and Foamular C-300 EPS (extruded polystyrene) insulation foam [20, 10].

Figure 4.3 compares the compressive strength of the two foams using the MTS 550 load frame and compressive platen. Test specimens of dimensions 30mm x 30mm x 30mm are compressed at 0.01mm/s. The compressive strength is taken to be the stress associated with the long yield plateau.

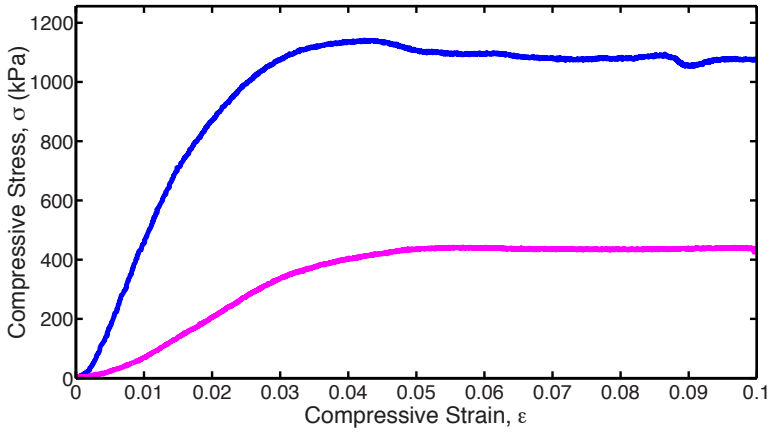

Figure 4.3: Compression stress-strain plot of core materials, EPS and ROHACELL 51-IG, plotted to 10% compression strain

Figure 4.4 compares the shear stress for each core. Shear test specimens comprised of 120mm x 45mm x 30mm foam pieces adhered to two 120mm x 45mm steel shear plates. Test specimens are compressed within the MTS 550 load frame at 0.005mm/s.

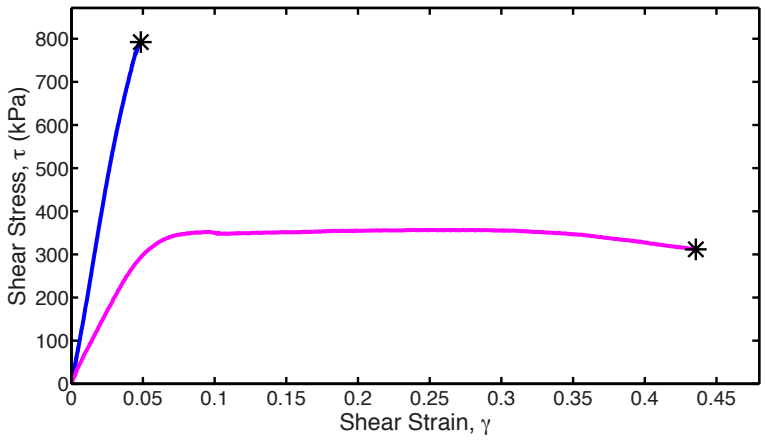

Figure 4.4: Shear stress-strain plot of core materials, EPS and ROHACELL 51-IG

The results of compression and shear testing for both ROHACELL 51-IG and EPS core materials are shown in Table 4.2.

Table: 4.2 Core material properties - experiment results

Material Property	Extruded Polystyrene (EPS)	ROHACELL 51-IG
Elastic Modulus, E_c (MPa)	13	67
Compressive Strength (10% Strain), σ_c (kPa)	422	1076
Shear Modulus, G_c (MPa)	7	19
Shear Yield Stress, τ_y (kPa)	282	-
Shear Strength, τ_c (kPa)	357	792
Density, ρ_f (kg/m^3)	28	50

Shear strength of the elastic-brittle ROHACELL 51-IG is 792kPa before fracture. For EPS, the foam undergoes considerable plastic deformation before separating from the shear plates; therefore, shear failure is assumed at yielding using 0.2% strain offset (τ_y=282.36kPa).

4.1.3 Beam Fabrication

Face and core components are cut to the specified dimension requirements of each test, then bonded together using Huntsman Araldite 2011Y epoxy adhesive [17]; the curing time is 24 hours.

4.2 Data Acquisition

Figure 4.5 summarizes the data acquisition tools used during the experiment phase.

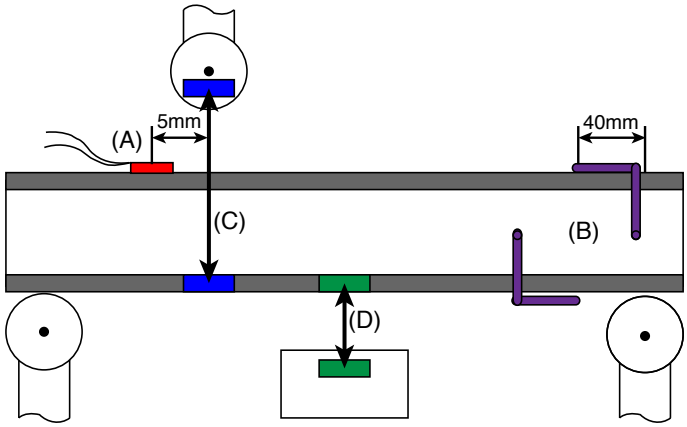

Figure 4.5: Placement summary of data acquisition instruments: (A) strain gauge, (B) core shear clip gauge, (C) core indentation, (D) midspan displacment

4.2.1 Strain Gauge (A)

TML strain gauges of length 2mm (TML FLA-2-11, [41]) are installed on the top face sheet of the beam, 5mm from the load roller to track compressive axial strain.

4.2.2 Core Shear Strain Gauge (B)

A core shear clip gauge, comprised of an MTS displacement gauge and two 14-gauge aluminum wires, are adhered to top and bottom face sheets 40mm inside the side support position, seen in Figure 4.6. The bonding of the aluminum wires to the face sheets use the same Huntsman Araldite 2011Y epoxy adhesive [17] and are applied after the initial beam construction.

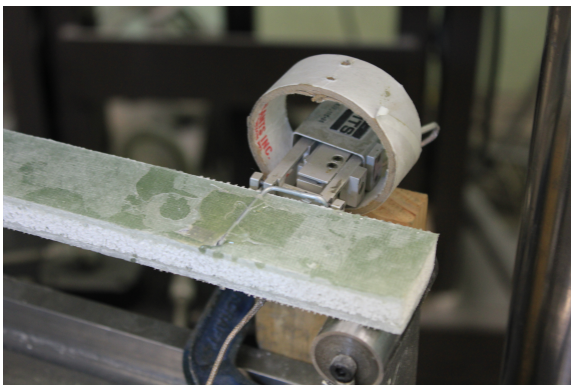

Figure 4.6: Test setup for clip gauge

4.2.3 Laser Extensometry (C)-(D)

A LE-05 laser extensometer measures the linear displacement of two points marked by reflective tape, shown in Figure 4.7.

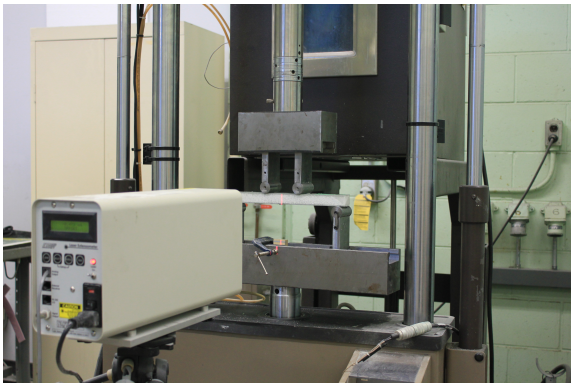

Figure 4.7: Test setup for laser extensometer

Core indentation (C) is measured from the displacement of the load roller to the bottom face sheet. Midspan displacement (D) is measured from the displacement of the bottom face sheet to a set marker on the base unit.

4.2.4 Data Acquisition and Output

During testing, MTS, laser extensometer, strain gauge and clip gauge test data are compiled through the use of a National Instruments 6325 signal conditioner and Labview 8.9 software. Each half-second iteration is the average of 100 data samples taken at 10kHz, sequentially extracted from each device.

4.3 Test Outline

The following section outlines tests conducted for each loading case, considering GFRP/ROHACELL 51-IG and GFRP/EPS beams. The goal each test series is to span as much of the design space as possible, within the constraints set by the testing apparatus and the chosen materials. Composite sandwich beam test specimens comprise of face sheets 5-ply (0.85mm) to 13-ply (2.26) thick, cores c=10mm to 30mm, and beam lengths L=80-460mm long. The chosen beam width is b=35mm.

In Chapter 3, a stiffness constraint omits potential beam designs of undesired compliance. For the following study, tested beam designs are selected within a projected deflection ratio limit of $\hat{\delta} = 0.03 = 3\%$.

4.3.1 Case A: Three Point Bending

Figures 4.8 and 4.9 plot the experiments on the corresponding failure mechanism maps, Figure 4.8 for GFRP/ROHACELL 51-IG beams and Figure 4.9 for GFRP/EPS.

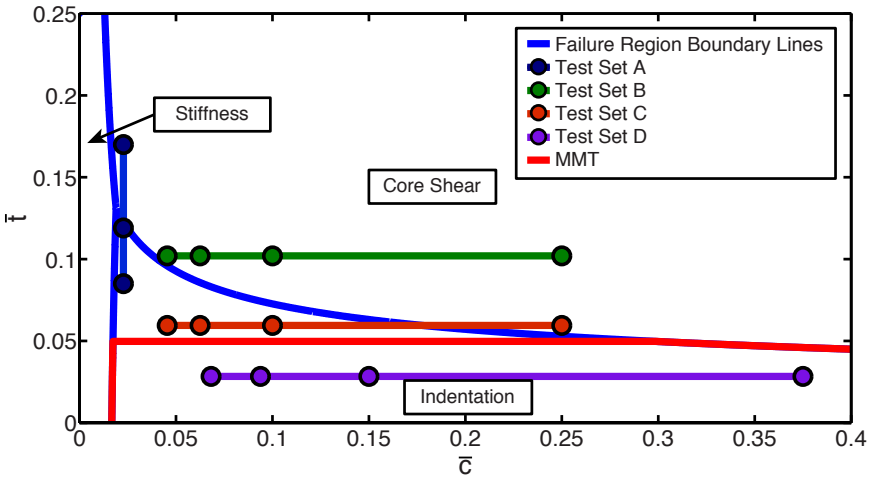

Figure 4.8: Test layout for simply supported three point bending case with respect to failure mechanism map - GFRP face sheets and ROHACELL 51-IG foam core, $\hat{\delta} = 3.0\%$

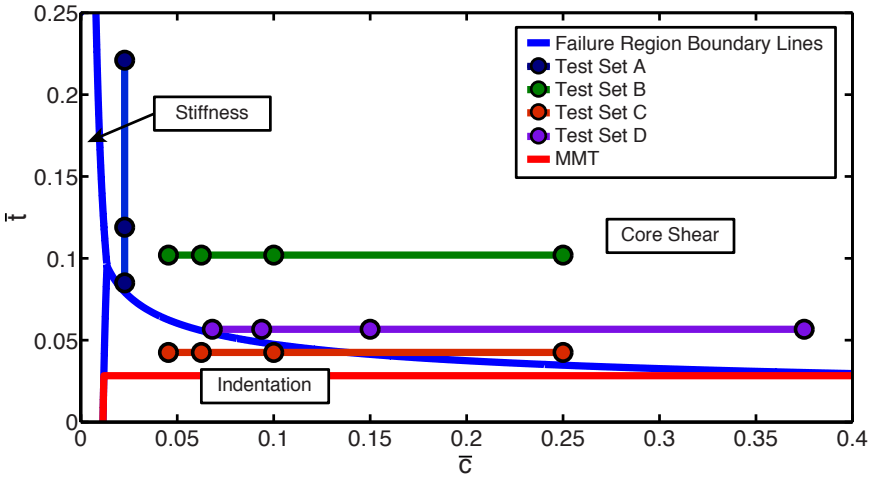

Figure 4.9: Test layout for simply supported three point bending case with respect to failure mechanism map - GFRP face sheets and extruded polystyrene (EPS) foam core, $\hat{\delta} = 3.0\%$

To relate each design point of $(\bar{c},\bar{t})$ from the failure mechanism maps, Tables 4.3 and 4.4 outline each test point in terms of chosen beam parameters. For both three and four point bending, beams are constructed with an overhang H=10mm. As the overhang is a fixed length rather than a set percentage of the beam length, failure mechanism maps for GFRP/EPS beams do not account for the overhang factor in core shear failure prediction. The predicted failure mechanism is calculated for each test geometry and given in Tables 4.3 and 4.4.

Table 4.3: Test summary for simply supported three point bending - GFRP/ROHACELL 51-IG

Test ID	$\bar{c}$	$\bar{t}$	t (mm)	c (mm)	L (mm)	Predicted Failure	Predicted $\hat{\delta}$ (%)	DAQ (A)	DAQ (B)	DAQ (C)	DAQ (D)
TRA1	0.023	0.085	0.85	10	440	I	2.16	Y	Y	Y	Y
TRA2	0.023	0.119	1.19	10	440	I	2.45	Y	Y	Y	Y
TRA3	0.023	0.170	1.7	10	440	CS	2.05		Y	Y	Y
TRB1	0.250	0.102	2.04	20	80	CS	1.04			Y	Y
TRB2	0.100	0.102	2.04	20	200	CS	1.12		Y	Y	Y
TRB3	0.063	0.102	2.04	20	320	CS	1.26		Y		Y
TRB4	0.045	0.102	2.04	20	440	I	1.47		Y	Y	Y
TRC1	0.250	0.060	0.85	20	80	CS	1.05			Y	Y
TRC2	0.100	0.060	0.85	20	200	I	0.98		Y	Y	Y
TRC3	0.063	0.060	0.85	20	320	I	1.03		Y		Y
TRC4	0.045	0.060	0.85	20	440	I	1.21		Y	Y	Y
TRD1	0.375	0.028	0.85	30	80	I	0.65			Y	Y
TRD2	0.150	0.028	0.85	30	200	I	0.54		Y	Y	Y
TRD3	0.094	0.028	0.85	30	320	I	0.56		Y		Y
TRD4	0.068	0.028	0.85	30	440	I	0.66		Y	Y	Y

Table 4.4: Test summary for simply supported three point bending - GFRP/EPS

Test ID	$\bar{c}$	$\bar{t}$	t (mm)	c (mm)	L (mm)	Predicted Failure	Predicted $\hat{\delta}$ (%)	DAQ (A)	DAQ (B)	DAQ (C)	DAQ (D)
TEA1	0.023	0.100	0.85	10	440	I	1.88	Y	Y	Y	Y
TEA2	0.023	0.140	1.19	10	440	CS	1.73	Y	Y	Y	Y
TEA3	0.023	0.260	2.21	10	440	CS	1.38		Y	Y	Y
TEB1	0.250	0.120	2.04	20	80	CS	1.22			Y	Y
TEB2	0.100	0.120	2.04	20	200	CS	1.17		Y	Y	Y
TEB3	0.063	0.120	2.04	20	320	CS	1.29		Y		Y
TEB4	0.045	0.120	2.04	20	440	CS	1.25		Y	Y	Y
TEC1	0.250	0.050	0.85	20	80	I *	1.39			Y	Y
TEC2	0.100	0.050	0.85	20	200	I	1.01		Y	Y	Y
TEC3	0.063	0.050	0.85	20	320	I	0.98		Y		Y
TEC4	0.045	0.050	0.85	20	440	I	1.00		Y	Y	Y
TED1	0.375	0.067	1.7	30	80	CS	1.51			Y	Y
TED2	0.150	0.067	1.7	30	200	CS	1.13		Y	Y	Y
TED3	0.094	0.067	1.7	30	320	I *	1.32		Y		Y
TED4	0.068	0.067	1.7	30	440	I *	1.23		Y	Y	Y

* - Predicted to fail by indentation when overhang factor is applied

Four common beam cases are considered: long compliant beams of thin cores (Test Set A), beams comprised of thick face sheets (Test Set B), thin face sheets (Test Set C) and thick cores (Test Set D).

Strain gauges are installed on Test Set A beams as they are the mostly likely to promote microbuckling failure and core shear strain gauges are installed on all tests with the exception of short beams (ie. L=80mm) as the clips interfere with the load contacts. Although the MTS load frame provides crosshead displacement data, midspan deflection is measured by the laser extensometer. Using a second beam specimen, select tests are repeated using the laser extensometer to measure core indentation.

4.3.2 Case B: Four Point Bending

For four point bending tests, the considered load roller spacing, a, is 80mm. As the load spacing is fixed for a range of beam lengths, the experiments cannot be plotted with respect to a single set of failure region boundary lines. Figures 4.10 and 4.11 uses the method seen in Figure 3.12, comparing failure region boundary lines for a range of $\bar{a}$. As reference, the $\bar{a}$ of each test point is displayed in brackets.

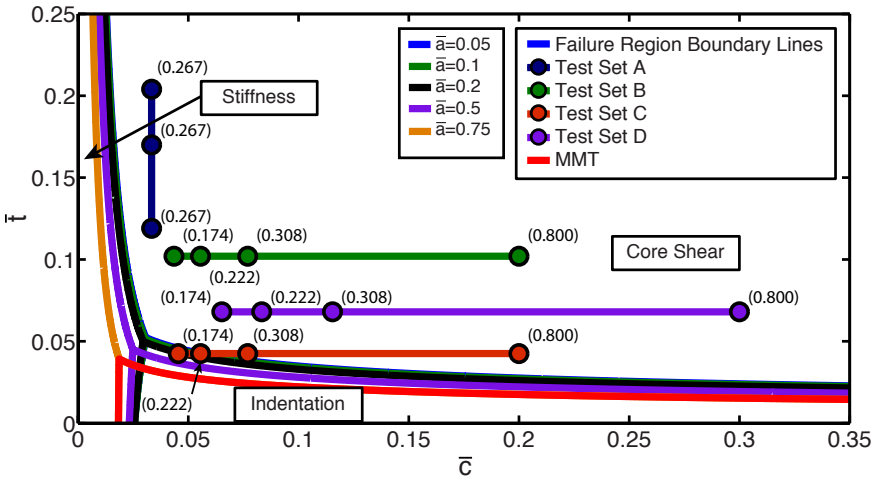

Figure 4.10: Test layout for simply supported four point bending case with respect to failure mechanism map - GFRP face sheets and ROHACELL 51-IG foam core, $\hat{\delta} = 3.0\%$, varied $\bar{a}$

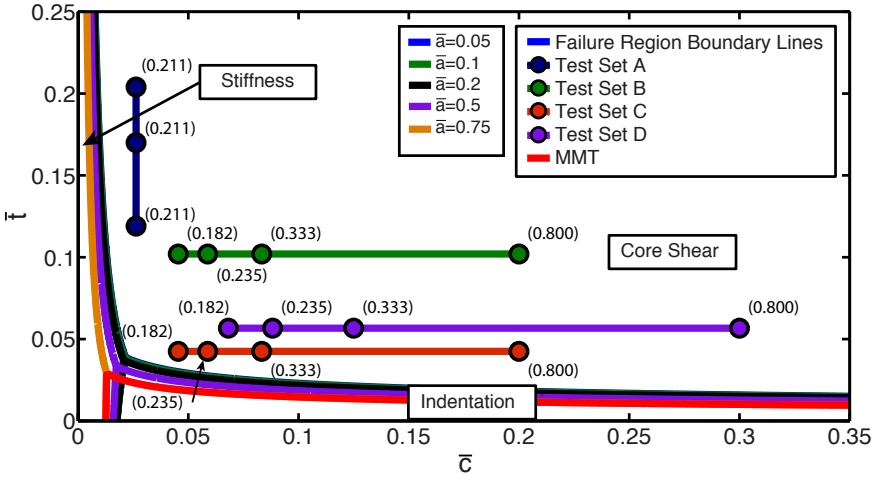

Figure 4.11: Test layout for simply supported four point bending case with respect to failure mechanism map - GFRP face sheets and extruded polystyrene (EPS) foam core, $\hat{\delta} = 3.0\%$, varied $\bar{a}$

Table 4.5 lists the tests for GFRP/ROHACELL 51-IG beams, Table 4.6 for GFRP/EPS beams. For the considered range of face sheet and core thicknesses, tests cannot be selected within the predicted indentation failure region, only core shear.

Table 4.5: Test summary for simply supported four point bending - GFRP/ROHACELL 51-IG

Test ID	$\bar{c}$	$\bar{t}$	t (mm)	c (mm)	L (mm)	Predicted Failure	Predicted $\hat{\delta}$ (%)	DAQ (A)	DAQ (B)	DAQ (C)	DAQ (D)
FRA1	0.033	0.119	0.19	10	300	CS	1.37	Y	Y	Y	Y
FRA2	0.033	0.170	1.7	10	300	CS	1.19	Y	Y		Y
FRA3	0.033	0.204	2.04	10	300	CS	1.09		Y	Y	Y
FRB1	0.200	0.102	2.04	20	100	CS	0.21			Y	Y
FRB2	0.077	0.102	2.04	20	260	CS	0.85		Y		Y
FRB3	0.056	0.102	2.04	20	360	CS	1.09		Y	Y	Y
FRB4	0.043	0.102	2.04	20	460	CS	1.32		Y		Y
FRC1	0.200	0.043	0.85	20	100	CS	0.22			Y	Y
FRC2	0.077	0.043	0.85	20	260	CS	1.06		Y		Y
FRC3	0.056	0.043	0.85	20	360	CS	1.51		Y	Y	Y
FRC4	0.043	0.043	0.85	20	460	I	2.05		Y		Y
FRD1	0.300	0.068	2.04	30	100	CS	0.22			Y	Y
FRD2	0.115	0.068	2.04	30	260	CS	0.81		Y		Y
FRD3	0.083	0.068	2.04	30	360	CS	0.99		Y	Y	Y
FRD4	0.065	0.068	2.04	30	460	CS	1.18		Y		Y

Table 4.6: Test summary for simply supported four point bending - GFRP/EPS

Test ID	$\bar{c}$	$\bar{t}$	t (mm)	c (mm)	L (mm)	Predicted Failure	Predicted $\hat{\delta}$ (%)	DAQ (A)	DAQ (B)	DAQ (C)	DAQ (D)
FEA1	0.026	0.119	0.19	10	300	CS	1.26	Y	Y	Y	Y
FEA2	0.026	0.170	1.7	10	300	CS	1.18	Y	Y		Y
FEA3	0.026	0.204	2.04	10	300	CS	1.07		Y	Y	Y
FEB1	0.200	0.104	2.04	20	100	CS	0.30			Y	Y
FEB2	0.083	0.104	2.04	20	240	CS	0.90		Y		Y
FEB3	0.059	0.104	2.04	20	340	CS	1.00		Y	Y	Y
FEB4	0.045	0.104	2.04	20	440	CS	1.10		Y		Y
FEC1	0.200	0.043	0.85	20	100	CS	0.22			Y	Y
FEC2	0.083	0.043	0.85	20	240	CS	0.87		Y		Y
FEC3	0.059	0.043	0.85	20	340	CS	1.10		Y	Y	Y
FEC4	0.045	0.043	0.85	20	440	CS	1.36		Y		Y
FED1	0.300	0.057	1.7	30	100	CS	0.24			Y	Y
FED2	0.125	0.057	1.7	30	240	CS	0.79		Y		Y
FED3	0.088	0.057	1.7	30	340	CS	0.92		Y	Y	Y
FED4	0.068	0.057	1.7	30	440	CS	1.08		Y		Y

4.3.3 Case C: Uniformly Distributed Loading

A test fixture to simulate uniform loading must be constructed. The loading apparatus must adhere to the three design criteria, defined below:

- The transmitted pressure must maintain its uniformity as the beam deflects
- The loading fixture must follow the natural curvature of the beam and cannot force an alternate form of deformation
- All energy transmitted from the load frame to the beam is conserved

Seen in previous literature, a common strategy has been to use an airbag testing system [42, 21]. The pressure load is distributed across the beam via a flat plate compressing on the top of a thick polymer airbag, lying across the entire beam length. As the beam defects, the airbag deforms to the curvature of the beam.

The following study proposes an alternative approach, considering that the uniform load can be simplified to a finite number of point loads.

Prototype Testing Method: Whippletree Loading Apparatus

Figure 4.12 below shows the proposed texting fixture for simulating uniform loading. Based on a whippletree design, the point loads splay outward evenly as midspan deflection increases. Figure 4.12 is a picture of the final product, machined by Lilex Industries.

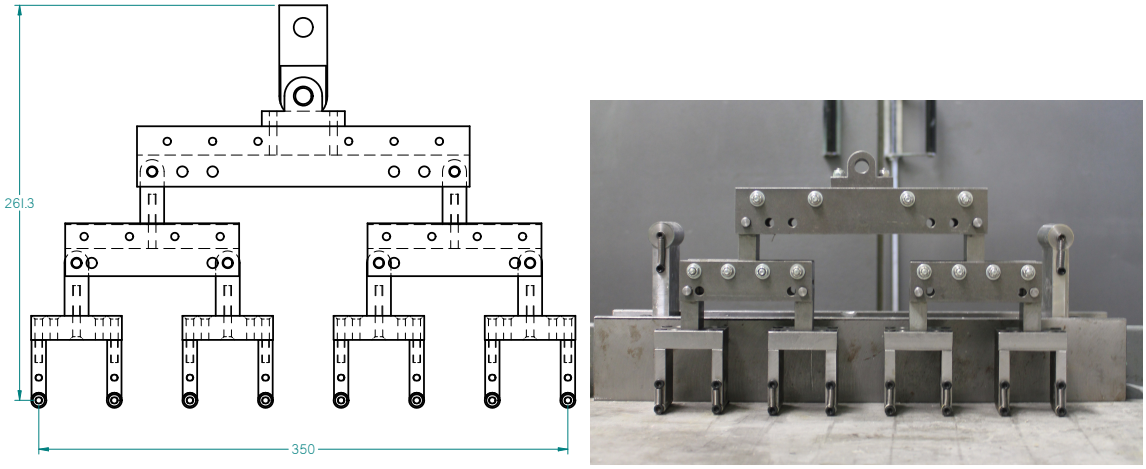

Figure 4.12: Schematic of whippletree loading apparatus

Ideally, an infinite number of roller contacts would accurately represent a uniform pressure. For the purpose of the following experiments, eight load rollers are considered acceptable for uniform pressure simulation. The above design is comprised of three branch levels (1 primary, 2 secondary, and 4 tertiary), each allowed to freely pivot on lubricated pins. Eight contact rollers are installed to arms on the tertiary branches by set screws and springs. Parts were machined using machine steel with exception for the contact rollers made from stainless steel.

To stay within the size constraints of the MTS load frame, the test fixture length is set at 350mm, having each roller contact of radius 10mm distance of 50mm apart.

Initial Composite Sandwich Beam Testing and Modification

A series of initial tests are conducted to determine what modifications, if any, are required to ensure the applied load simulates a uniform pressure. The tests also determines the ideal beam length that best coincide with stiffness and strength prediction. It is assumed here that when both analytical predictions and experiment data show similar results, both methods are valid. The following series of tests use 25mm wide beams, comprising of 1.19mm GFRP face sheets and 30mm ROHACELL 51-IG core material.

After the first set of tests, two challenges are noted. First, due to the significant surface roughness of the GFRP, the intended splay-out motion of the whippletree branches is frequently restricted. Once halted, the branches lift up from the beam and any rollers still in contact become concentrated point loads. Secondly, all preliminary beams fail prematurely due to indentation occurring at the side supports.

To provide a friction-free surface, the first challenge is solved by inserting a thin strip of PVC between the top face sheet and roller contacts. The track and roller contacts are lubricated to minimize surface roughness. PVC is chosen over other materials due to its elastic modulus being significantly lower than the estimated GFRP stiffness. Figure 4.13 shows a simply supported composite sandwich beam subject to the whippletree loading fixture with the PVC track installed.

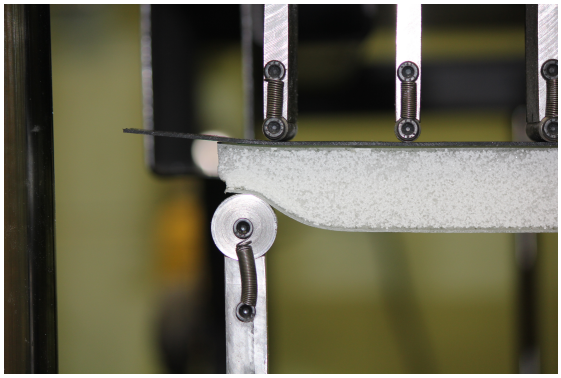

Figure 4.13: Uniformly distributed loading test using the whippletree loading rig with PVC track, no side support tabs - subject to indentation

To eliminate side support indentation, tabs comprised of two different materials (PVC and steel) are placed underneath the beams at the side supports. Varying beam length between 380mm and 400mm, Figures 4.14(a) and 4.15(b) compare the observed results of each tab material at the side supports, while Figure 4.15 plots the results of each in terms of pressure-displacement curves. For continuity, overhang is held at $H = 10$mm.

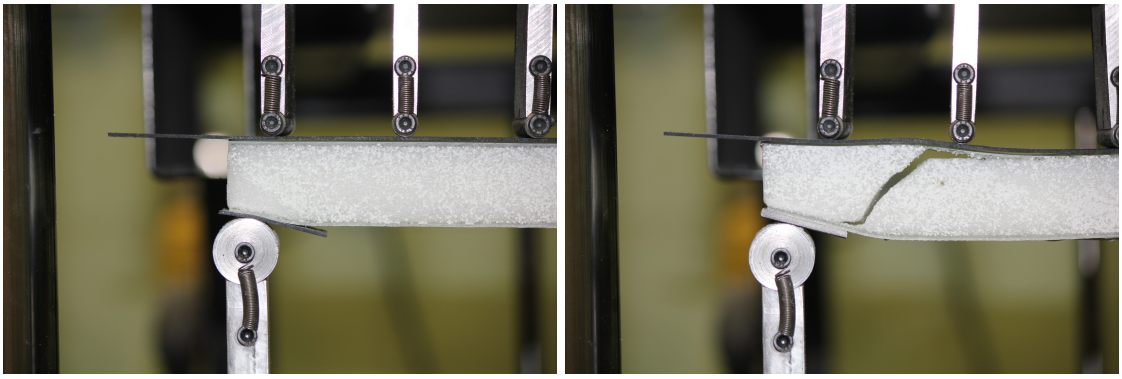

Figure 4.14: Whippletree loading apparatus side support modification - side support comparison, PVC, subject to indentation (left), steel, subject to crush (right)

Similar to the case of having no tab, adding PVC yields no improvement in reducing side support indentation, however, it is prevented using the steel tabs. With initial performance issues resolved, the next objective is to determine the optimal beam length that best correlates both analytical and experiment results. To determine the best option, three beam lengths are considered: 360mm, 380mm and 400mm. The results of the following tests are summarized in Table 4.7 below:

Table 4.7: Whippletree loading apparatus calibration testing - results summary

Tab	Beam Length, L (mm)	Overhang, H (mm)	Stiffness Predicted/Observed	Failure Pressure Predicted/Observed	Discrepancies
None	400	10	1.38	1.39	[1]
Plastic	380	10	0.87	1.22	[1]
Plastic	400	10	1.02	1.35	[1]
Metal	380	10	1.07	1.15	[2]
Metal	400	10	1.14	1.20	[2]
Metal	360	10	0.90	0.98	[3]
Metal	380	40	0.94	0.94	None

[1] Side Support Indentation, [2] Side Support Crush, [3] WTLR roller contacts exceed beam length

In comparing the results of the three different beam lengths, both the 360mm and 380mm test beams performed close to their predicted values. Though either beam length could be chosen from these results alone, prior to failure the whippletree roller contacts splayed beyond the side supports during the $L = 360$mm test. Therefore, the only suitable beam length for testing is 380mm.

Seen in Figure 4.14, due to the chosen short overhang being relatively short, all metal-tabbed beams incurred minor core crushing at the side support prior to core shear failure. By extending the overhang to 40mm, core crush at the side supports is eliminated and experiment results come within 6% error to both stiffness and strength predictions.

In summary, to simulate uniform pressure loading a whippletree testing fixture is machined and tested. By providing a friction-free surface for the point loads, a larger surface area for side supports, in addition to ideal beam length and overhang considerations, uniformly distributed loads are simulated using the whippletree testing fixture design.

Experiment Failure Mechanism Maps and Test Lists

Figures 4.15 and 4.16 display the tests for the uniform loading case on terms of failure mechanism maps, while Tables 4.8 and 4.9 list the beam geometry and data acquisition tools assigned.

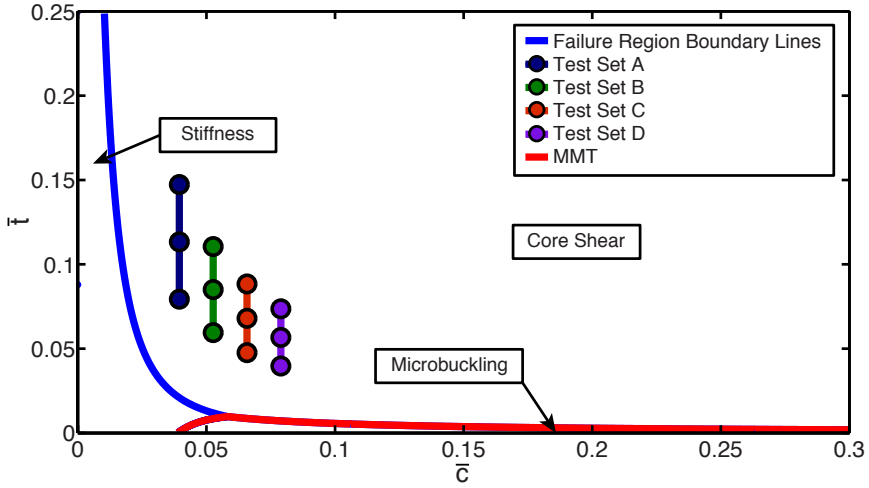

Figure 4.15: Test layout for simply supported uniformly distributed load case with respect to failure mechanism map - GFRP face sheets and ROHACELL 51-IG foam core, $\hat{\delta} = 3.0\%$

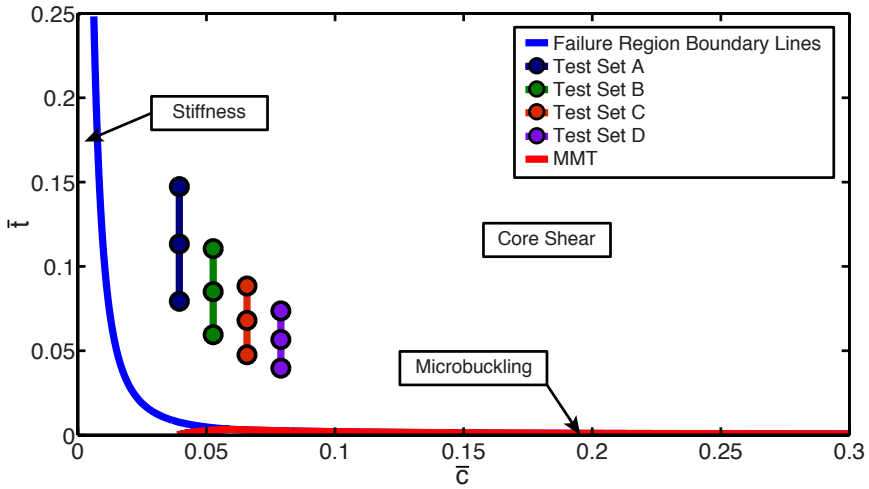

Figure 4.16: Test layout for simply supported uniformly distributed load case with respect to failure mechanism map - GFRP face sheets and extruded polystyrene (EPS) foam core, $\hat{\delta} = 3.0\%$

Table 4.8: Test summary for simply supported uniformly distributed loading - GFRP/ROHACELL 51-IG

Test ID	$\bar{c}$	$\bar{t}$	t (mm)	c (mm)	L (mm)	Predicted Failure	Predicted $\hat{\delta}$ (%)	DAQ (A)	DAQ (B)	DAQ (C)
URA1	0.039	0.073	1.19	15	380	CS	1.52	Y	Y	Y
URA2	0.039	0.113	1.7	15	380	CS	1.35	Y	Y	Y
URA3	0.039	0.147	2.21	15	380	CS	1.27		Y	Y
URB1	0.053	0.060	1.19	20	380	CS	1.41	Y	Y	Y
URB2	0.053	0.085	1.7	20	380	CS	1.28		Y	Y
URB3	0.053	0.111	2.21	20	380	CS	1.22		Y	Y
URC1	0.066	0.048	1.19	25	380	CS	1.33		Y	Y
URC2	0.066	0.068	1.7	25	380	CS	1.23		Y	Y
URC3	0.066	0.088	2.21	25	380	CS	1.18		Y	Y
URD1	0.079	0.040	1.19	30	380	CS	1.29		Y	Y
URD2	0.079	0.057	1.7	30	380	CS	1.20		Y	Y
URD3	0.079	0.074	2.21	30	380	CS	1.16		Y	Y

Table 4.9: Test summary for simply supported uniformly distributed loading - GFRP/EPS

Test ID	$\bar{c}$	$\bar{t}$	t (mm)	c (mm)	L (mm)	Predicted Failure	Predicted $\hat{\delta}$ (%)	DAQ (A)	DAQ (B)	DAQ (C)
UEA1	0.039	0.073	1.19	15	380	CS	1.46	Y	Y	Y
UEA2	0.039	0.113	1.7	15	380	CS	1.40	Y	Y	Y
UEA3	0.039	0.147	2.21	15	380	CS	1.43		Y	Y
UEB1	0.053	0.060	1.19	20	380	CS	1.43	Y	Y	Y
UEB2	0.053	0.085	1.7	20	380	CS	1.36		Y	Y
UEB3	0.053	0.111	2.21	20	380	CS	1.33		Y	Y
UEC1	0.066	0.048	1.19	25	380	CS	1.41		Y	Y
UEC2	0.066	0.068	1.7	25	380	CS	1.36		Y	Y
UEC3	0.066	0.088	2.21	25	380	CS	1.31		Y	Y
UED1	0.079	0.040	1.19	30	380	CS	1.38		Y	Y
UED2	0.079	0.057	1.7	30	380	CS	1.33		Y	Y
UED3	0.079	0.074	2.21	30	380	CS	1.33		Y	Y

To account for a fixed beam length of 380mm, each test set considers a set core thickness range of 15-30mm, and face sheet thickness range of 1.4mm-2.6mm respectively. Strain gauges are reserved to those tests nearest to the microbuckling failure region. As core indentation has been analytically disregarded, the laser extensometer is only used to measure midspan displacement.

4.4 Experiment Results

Tables 4.10-4.15 list the results from all conducted experiments. The four parameters compared are: stiffness, observed failure mechanism, failure load, and observed deflection ratio. The observed deflection ratio is the predicted failure load over the observed stiffness. Tests that incorrectly predicted the active failure mechanism or exceeded the projected deflection ratio limit of $\hat{\delta} = 3\%$ are highlighted in red.

Stiffness results are analyzed in Section 4.5, followed by failure analysis in Section 4.6.

4.4.1 Three Point Bending

Table 4.10: Summary of three point bending tests - GFRP/ROHACELL 51-IG

Test ID	Observed Stiffness (N/mm)	Observed Failure Type	Observed Failure Load (N)	**Stiffness Prediction/ Observed**	**Failure Load Prediction/ Observed**	**Observed Deflection Ratio (%)**
TRA1	32	I	429	**1.45**	**0.87**	**3.12**
TRA2	35	CS	579	**1.60**	**1.05**	**3.92**
TRA3	69	CS	733	**1.05**	**0.88**	**2.15**
TRB1	809	CS	1293	**1.68**	**0.87**	**1.74**
TRB2	426	CS	1207	**1.22**	**0.97**	**1.37**
TRB3	292	CS	1486	**1.01**	**0.80**	**1.28**
TRB4	203	I	1311	**0.93**	**0.93**	**1.37**
TRC1	406	CS	745	**3.47**	**1.55**	**3.63**
TRC2	386	CS	762	**1.26**	**1.25**	**1.24**
TRC3	305	I	858	**0.78**	**0.91**	**0.80**
TRC4	132	I	785	**1.05**	**0.94**	**1.27**
TRD1	1254	I	1219	**1.63**	**0.87**	**1.06**
TRD2	516	I	719	**1.40**	**1.09**	**0.76**
TRD3	330	I	681	**1.13**	**0.99**	**0.64**
TRD4	207	I	699	**1.00**	**0.86**	**0.66**

Table 4.11: Summary of three point bending tests - GFRP/EPS

Test ID	Observed Stiffness (N/mm)	Observed Failure Type	Observed Failure Load (N)	**Stiffness Prediction/ Observed**	**Failure Load Prediction/ Observed**	**Observed Deflection Ratio (%)**
TEA1	24	I	203	**1.14**	**1.12**	**2.14**
TEA2	33	CS	270	**0.94**	**0.87**	**1.63**
TEA3	51	CS	313	**0.80**	**0.79**	**1.10**
TEB1	654	CS	590	**0.79**	**0.86**	**0.97**
TEB2	210	CS	488	**0.92**	**0.92**	**1.07**
TEB3	136	CS	504	**0.88**	**0.98**	**1.14**
TEB4	96	CS	424	**0.86**	**1.08**	**1.08**
TEC1	205	CS	465	**2.36**	**1.08**	**3.05**
TEC2	167	I	361	**1.11**	**1.17**	**1.13**
TEC3	91	I	301	**1.07**	**1.10**	**1.05**
TEC4	59	I	273	**1.08**	**1.05**	**1.09**
TED1	896	CS	745	**0.82**	**1.20**	**1.24**
TED2	297	CS	617	**0.97**	**1.05**	**1.09**
TED3	166	I	679	**1.00**	**1.24**	**1.32**
TED4	108	I	539	**1.09**	**1.19**	**1.34**

4.4.2 Four Point Bending

Table 4.12: Summary of four point bending tests - GFRP/ROHACELL 51-IG

Test ID	Observed Stiffness (N/mm)	Observed Failure Type	Observed Failure Load (N)	**Stiffness Prediction/ Observed**	**Failure Load Prediction/ Observed**	**Observed Deflection Ratio (%)**
FRA1	88	CS	779	**1.75**	**0.81**	**2.40**
FRA2	99	CS	843	**1.79**	**0.75**	**2.13**
FRA3	177	CS	1050	**1.16**	**0.65**	**1.27**
FRB1	1534	CS	1857	**3.84**	**0.67**	**0.81**
FRB2	543	CS	1784	**1.00**	**0.67**	**0.85**
FRB3	286	CS	1486	**1.06**	**0.79**	**1.15**
FRB4	158	CS	1020	**1.25**	**1.17**	**1.64**
FRC1	2567	CS	1074	**1.90**	**1.01**	**0.42**
FRC2	240	CS	1023	**1.72**	**1.11**	**1.82**
FRC3	173	I	1012	**1.16**	**1.08**	**1.75**
FRC4	88	A*	664	**1.31**	**1.54**	**2.70**
FRD1	1283	CS	1617	**6.27**	**0.99**	**1.31**
FRD2	767	CS	1551	**1.10**	**1.13**	**0.88**
FRD3	478	CS	1850	**1.02**	**0.94**	**1.01**
FRD4	299	CS	1957	**0.95**	**0.88**	**1.12**

Table 4.13: Summary of four point bending tests - GFRP/EPS

Test ID	Observed Stiffness (N/mm)	Observed Failure Type	Observed Failure Load (N)	**Stiffness Prediction/ Observed**	**Failure Load Prediction/ Observed**	**Observed Deflection Ratio (%)**
FEA1	39	CS	264	**1.29**	**0.90**	**1.62**
FEA2	61	CS	278	**0.84**	**0.83**	**0.99**
FEA3	69	CS	325	**0.88**	**0.76**	**0.95**
FEB1	1792	CS	1077	**1.02**	**0.50**	**0.30**
FEB2	254	CS	571	**0.97**	**0.93**	**0.87**
FEB3	166	CS	560	**0.78**	**0.79**	**0.78**
FEB4	100	CS	565	**0.98**	**0.85**	**1.08**
FEC1	1472	CS	586	**1.30**	**0.70**	**0.28**
FEC2	200	CS	455	**1.07**	**0.97**	**0.93**
FEC3	100	CS	446	**1.13**	**0.95**	**1.24**
FEC4	70	CS	414	**1.03**	**1.05**	**1.40**
FED1	1558	CS	672	**1.79**	**1.00**	**0.43**
FED2	333	CS	720	**1.02**	**0.89**	**0.80**
FED3	167	CS	725	**1.18**	**0.86**	**1.10**
FED4	171	CS	615	**0.78**	**1.03**	**0.84**

4.4.3 Uniformly Distributed Loading

Table 4.14: Summary of uniformly distributed loading tests - GFRP/ROHACELL 51-IG

Test ID	Observed Stiffness (kPa/mm)	Observed Failure Type	Observed Failure Pressure (kPa)	**Stiffness Prediction/ Observed**	**Failure Pressure Prediction/ Observed**	**Observed Deflection Ratio (%)**
URA1	9.8	CS	75	**1.19**	**0.89**	**1.81**
URA2	15.0	CS	98	**0.92**	**0.72**	**1.24**
URA3	17.5	CS	109	**0.86**	**0.67**	**1.09**
URB1	13.5	CS	100	**1.20**	**0.86**	**1.69**
URB2	18.1	CS	93	**1.03**	**0.97**	**1.32**
URB3	26.1	CS	149	**0.73**	**0.59**	**0.89**
URC1	23.1	CS	136	**0.94**	**0.80**	**1.25**
URC2	26.5	CS	127	**0.92**	**0.90**	**1.13**
URC3	26.5	CS	108	**1.09**	**1.04**	**1.28**
URD1	31.7	CS	139	**0.81**	**0.91**	**1.05**
URD2	34.7	CS	140	**0.84**	**0.94**	**1.00**
URD3	29.6	CS	130	**0.98**	**0.99**	**1.14**

Table 4.15: Summary of uniformly distributed loading tests - GFRP/EPS

Test ID	Observed Stiffness (kPa/mm)	Observed Failure Type	Observed Failure Pressure (kPa)	**Stiffness Prediction/ Observed**	**Failure Pressure Prediction/ Observed**	**Observed Deflection Ratio (%)**
UEA1	6.7	CS	32	**0.80**	**0.94**	**1.18**
UEA2	8.0	CS	38	**0.70**	**0.78**	**0.98**
UEA3	7.8	CS	30	**0.77**	**1.08**	**1.09**
UEB1	7.1	CS	42	**0.98**	**0.91**	**1.40**
UEB2	10.1	CS	42	**0.74**	**0.92**	**1.00**
UEB3	8.7	CS	35	**0.90**	**1.11**	**1.19**
UEC1	9.1	CS	37	**1.00**	**1.31**	**1.40**
UEC2	13.3	CS	48	**0.70**	**1.00**	**0.95**
UEC3	14.3	CS	57	**0.68**	**0.84**	**0.89**
UED1	11.6	CS	48	**0.90**	**1.15**	**1.25**
UED2	13.0	CS	57	**0.88**	**1.01**	**1.17**
UED3	15.1	CS	61	**0.75**	**0.93**	**0.99**

4.5 Stiffness Validation

Figures 4.17 and 4.18 are three dimensional surface plots of predicted stiffness index, with respect to the $[\bar{c}\text{-}\bar{t}]$ design space. Observed stiffness results from each test are converted to stiffness index terms and are shown as diamond, vertical line represent the observed error margin. The following plots serve as a visual representation for noting trends in stiffness prediction error. For quantitative results, refer back to Tables 4.10-4.15.

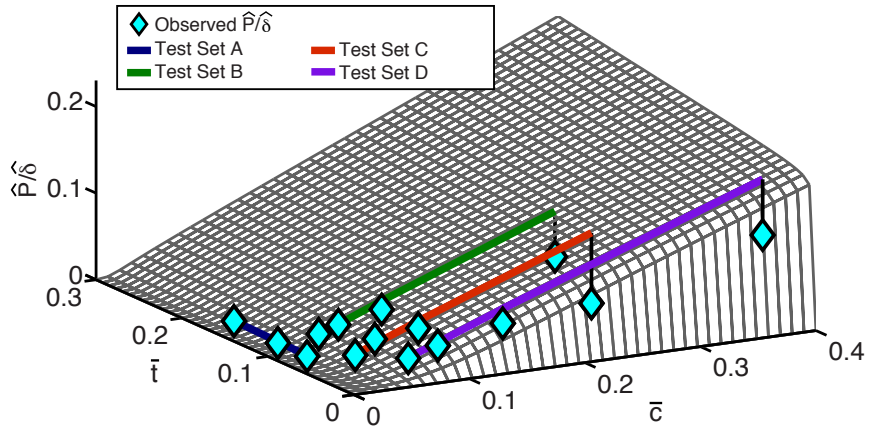

Figure 4.17: 3D comparison of observed stiffness to analytical predictions for simply supported composite sandwich beams subject to three point bending with respect to design space $[\bar{c}, \bar{t}]$ - GFRP face sheets and ROHACELL 51-IG foam core, $\hat{\delta} = 3.0\%$

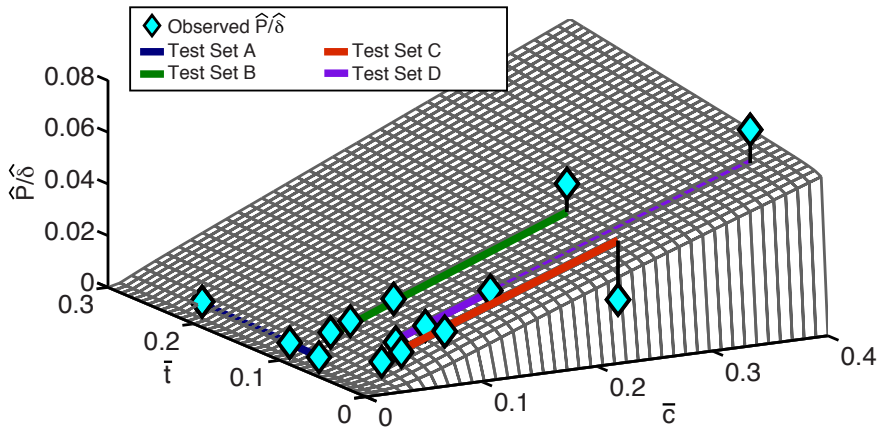

Figure 4.18: 3D comparison of observed stiffness to analytical predictions for simply supported composite sandwich beams subject to three point bending with respect to design space $[\bar{c}, \bar{t}]$ - GFRP face sheets and extruded polystyrene (EPS) foam core, $\hat{\delta} = 3.0\%$

Considering the effect of $\bar{t}$, beams of thin face sheets (Test Set C) are well predicted for both material cases. As thicker faces are tested for GFRP/EPS beams (tests TEA3, TEB1-TEB4), stiffness predictions are shown to be smaller than experiment results. As noted in Chapter 2, equivalent bending and shear stiffness terms are simplified assuming face sheets are relatively thin to the core material ($d \approx c$). For the case of tests TEA3-TEB4, if the full expressions for both bending and shear stiffness terms are used, predictions are improved by an average of $\sim 9\%$. Comparatively, GFRP/ROHACELL 51-IG tests with thick face sheets were originally well-predicted, so using the full stiffness expressions would only lead to larger error.

Considering the effect of $\bar{c}$, large errors are shown to occur when very long or short beams are compared.

Recalling the shear force diagram for three point bending in Figure 2.3, the transmitted shear load at the midspan occurs over an infinitely small length (represented by a piecewise function). As shorter beams are tested, the change is much more apparent. As stubby beams are tested (in this case, L=80mm), the maximum intended shear load of $P/2$ is never attained, resulting in indentation at the side supports. As the added deflection does not represent either bending or shear effects, analytical models become unreliable.

For the case of long beams, tests TRA1 and TRA2 are shown to drastically over-predict stiffness. The following error is presumed to occur due to beam sliding, where beyond a given compliance, the applied load simply pushes the beam through the side supports. The resulting error of stiffness prediction is not solely attributed to the analytical expressions, but due a noticeable flaw apparent in the simply supported beams.

Next, the stiffness results from all four point bending tests are detailed. Due to four point bending tests having a varied $\bar{a}$ term, predicted stiffness results cannot be visually represented as a 3D mesh. Alternatively, Figures 4.19 and 4.20 compare stiffness index results in terms of prediction-to-observed ratios.

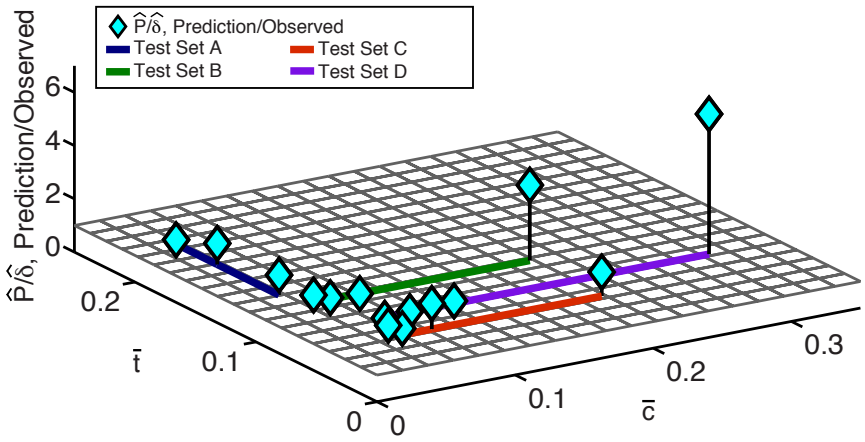

Figure 4.19: 3D comparison of observed stiffness to analytical predictions for simply supported composite sandwich beams subject to four point bending with respect to design space $[\bar{c}, \bar{t}]$ - GFRP face sheets and ROHACELL 51-IG foam core, $\hat{\delta} = 3.0\%$

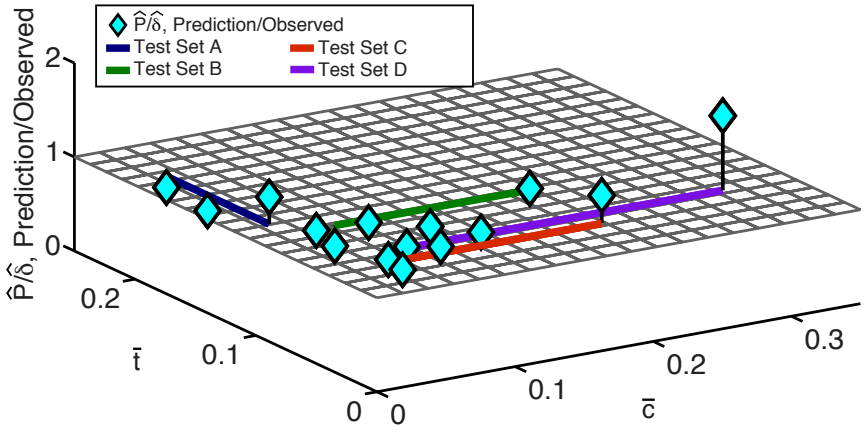

Figure 4.20: 3D comparison of observed stiffness to analytical predictions for simply supported composite sandwich beams subject to four point bending with respect to design space $[\bar{c}, \bar{t}]$ - GFRP face sheets and extruded polystyrene (EPS) foam core, $\hat{\delta} = 3.0\%$

Similar to three point bending, FRA1, FRA2 and FEA1 all have large errors in stiffness prediction due to the occurrence of beam sliding, short beams (for this case L=100mm) generally over-predict stiffness test results, and beams comprised of thick face sheets and EPS cores under-predict stiffness results due to simplifications made in equivalent bending and shear stiffness terms.

Finally, Figures 4.21 and 4.22 compare stiffness experiment results for uniformly distributed loading tests.

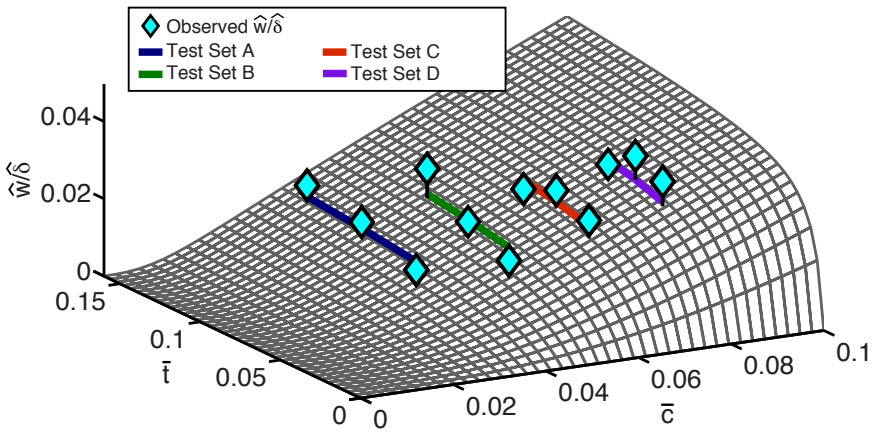

Figure 4.21: 3D comparison of observed stiffness to analytical predictions for simply supported composite sandwich beams subject to uniformly distributed loading with respect to design space $[\bar{c}, \bar{t}]$ - GFRP face sheets and ROHACELL 51-IG foam core, $\hat{\delta} = 3.0\%$

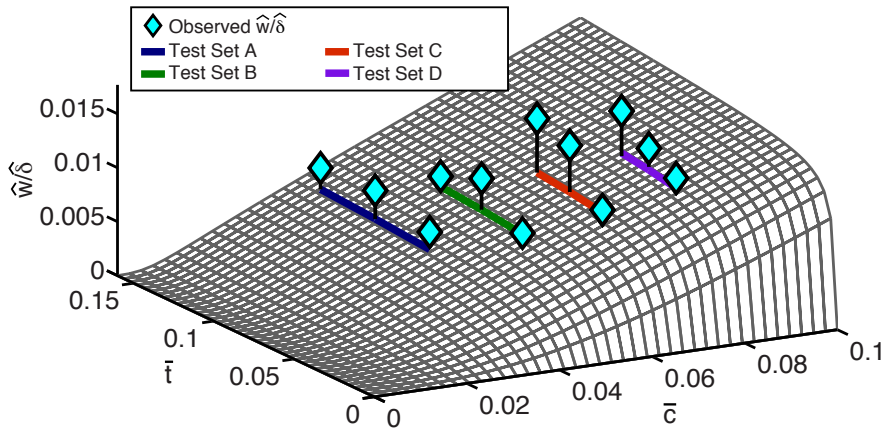

Figure 4.22: 3D comparison of observed stiffness to analytical predictions for simply supported composite sandwich beams subject to uniformly distributed loading with respect to design space $[\bar{c}, \bar{t}]$ - GFRP face sheets and extruded polystyrene (EPS) foam core, $\hat{\delta} = 3.0\%$

For uniformly distributed loading tests, any significant increase seen in Figures 4.21 and 4.22 in error are accounted to higher $\bar{t}$ tested (ie. thicker face sheets). Though different core thicknesses are tested over the fixed beam length, the change in stiffness prediction error is negligible.

For the three and four point bending tests, GFRP/ROHACELL 51-IG beams were generally well-predicted in stiffness as GFRP face sheets of 2.04mm were considered. Only during uniform loading tests, the first occurrences of stiffness under-prediction are noted. As URA3 and URB3 comprised of the thickest face sheets (t=2.21mm) of all the conducted experiments, it is shown that even ROHACELL must account for the full stiffness equation as face sheet thickness increases.

In summary, by comparing stiffness results of three point bending, four point bending and uniform loading tests, similar trends in accuracy are noted. Though the analytical models generally predict stiffness within a $\sim 15\%$ error for most beam designs, they become unreliable as either short or compliant beams are considered. Though beams of thick face sheets are originally under-predicted, error is reduced by using the unsimplified expressions for bending and shear stiffness. For EPS beams, the higher core compliance provides little contribution to the overall beam stiffness. In order to properly predict stiffness for beams comprised of complaint cores, full stiffness expressions are required even for thin face sheet designs. As more rigid cores are considered, a significantly face sheet thickness is required to show a similar effect.

4.6 Strength Validation

The following section analyzes failure prediction results for all loading cases. Core shear and indentation failures are identified using experiment results, then compared to predictions in terms of the $[\bar{c}\text{-}\bar{t}]$ design space.

4.6.1 Core Shear

Identifying failure in terms of three point bending tests, Figure 4.23 compares ROHACELL 51-IG and EPS beams failing by core shear.

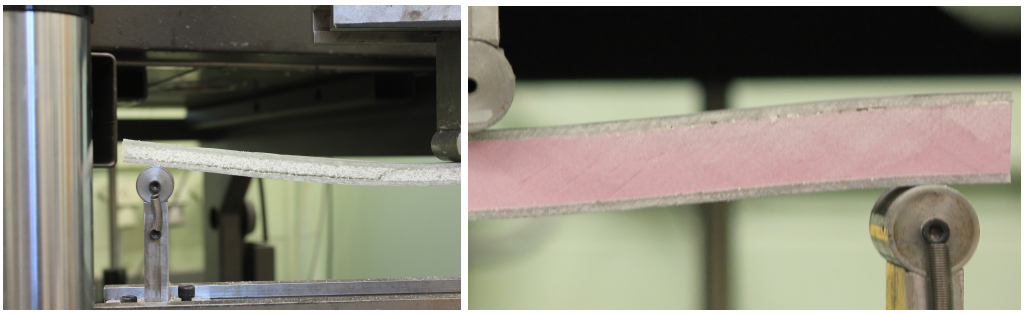

Figure 4.23: Observed core shear failure from simply supported three point bending tests - GFRP/ROHACELL 51-IG (left), GFRP/EPS (right)

Figure 4.24 compares stiffness and strength predictions for two beams failing by core shear, with respect to force-deflection curves.

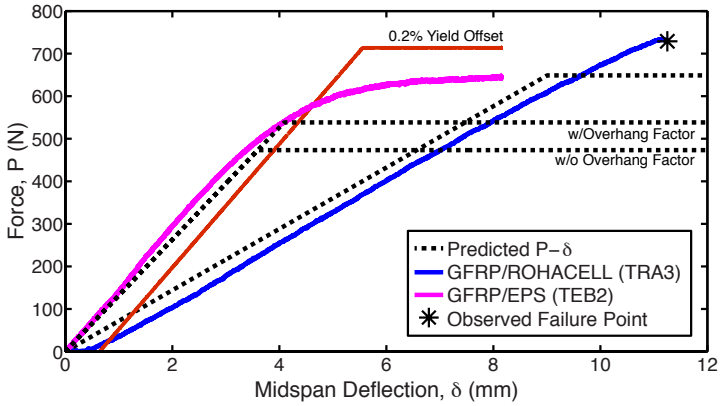

Figure 4.24: Force-deflection curves from simply supported three point bending tests, failing by core shear - results from TRA3 and TEB2

For beams comprised of ROHACELL 51-IG, core shear failure is identified by an instantaneous fracture of the core. In Figure 4.23, failure is seen as an oblique crack across the core and (in some cases) possible separation from the face sheet.

For EPS cores, core shear is harder to identify as the beam continues to sustain load even after failure (seen by Figure 4.24). After EPS yields in shear, the beam compresses, resembling the behaviour (and

visual appearance) of a more complaint beam. As failure for EPS beams is defined earlier as the shear yield stress, core shear failure is presumed to occur at the transition point between the elastic and plastic (or compliant) states. The considered 0.2% strain offset is the midspan deflection over total beam length.

Figure 4.25 and 4.26 shows the pressure-deflection curves for four point bending and uniformly distributed loading respectively, both yielding similar results.

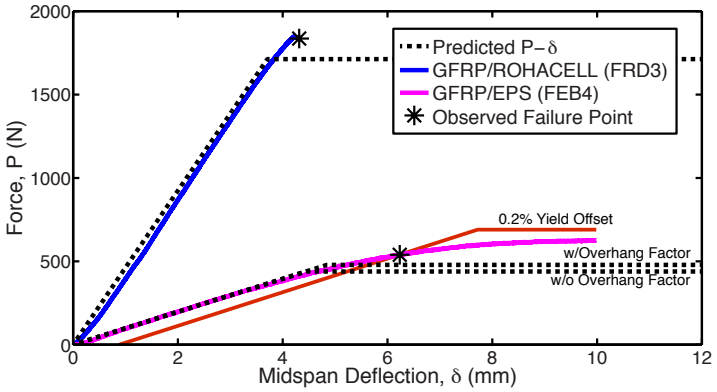

Figure 4.25: Force-deflection curves from simply supported four point bending tests, failing by core shear- results from FRD3 and FEB4

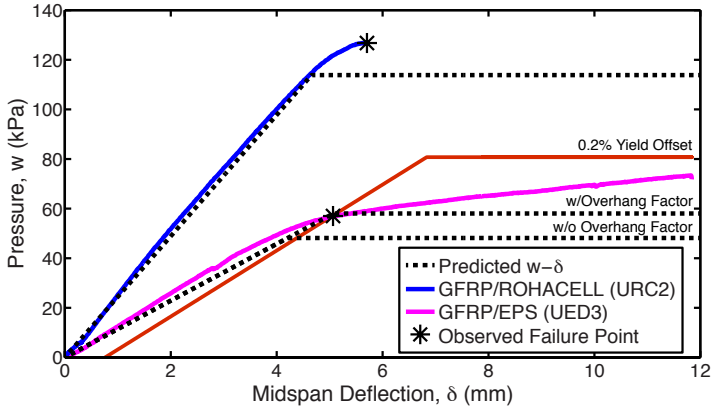

Figure 4.26: Force-deflection curves from simply supported uniformly distributed loading tests, failing by core shear - results from URC2 and UED3

Comparing core shear failure results in Tables 4.9-4.14, most experiments over-predict core shear failure. As most of these tests comprise of thick face sheets, prediction error may be reduced if the face sheet stiffening property is considered from Equation (2.9). In terms of three point bending tests, EPS beams benefit from the stiffening property, as predictions are improved by $> 1\%$. However, as ROHACELL is a stiffer core material than EPS, the improvement is less significant ($< 1\%$). Similar results are predicted to occur for the other two loading cases.

Using results from core shear strain data, Figures 4.27 compares force-core shear strain plots for GFRP/ROHACELL 51-IG tests and GFRP/EPS tests respectively.

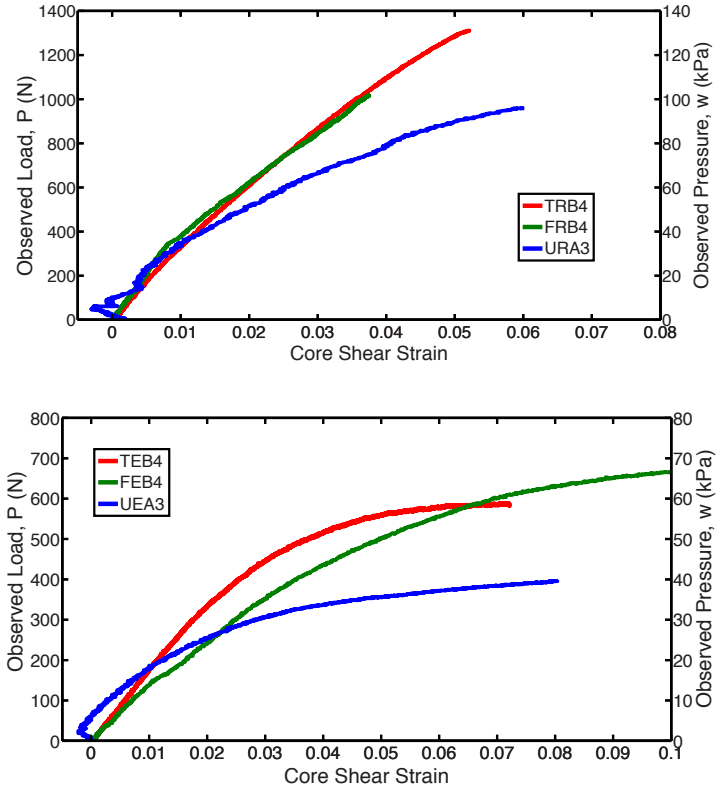

Figure 4.27: Force/pressure vs. core shear strain plots for tests failing by core shear - TRB4, FRB4 and URA3 (top), TEB4, FEB4 and UEA3 (bottom)

From Figure 4.27, core shear testing estimates ROHACELL 51-IG fails at $\sim 5\%$ strain while EPS yields at the 0.2% proof strain. Though different loading cases are compared above, similar trends are shown in comparing core shear strain data. As noted in the figure, interference between the track and core shear clips is observed during the initial movement of the point load rollers.

In summary, for composite sandwich beams, core shear failure is best predicted using the core shear strength for elastic-brittle cores and core shear yield stress for elastic-plastic cores. Though the classification of failure is different, both core failures can still be well-predicted using the same core shear failure load equation.

4.6.2 Indentation

Figure 4.28 compares visual identification of indentation failure for both GFRP/ROHACELL 51-IG and GFRP/EPS beams, while Figures 4.29 and 4.30 compare the respective force-deflection curves for three and four point bending cases.

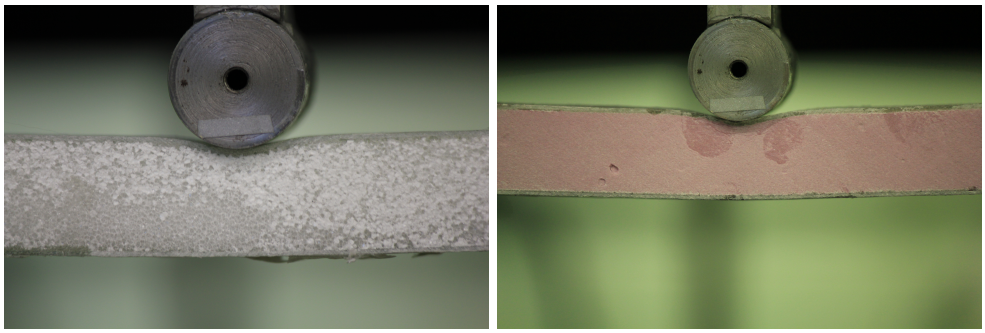

Figure 4.28: Observed indentation failure from simply supported three point bending tests - GFRP/ROHACELL 51-IG (left), GFRP/EPS (right)

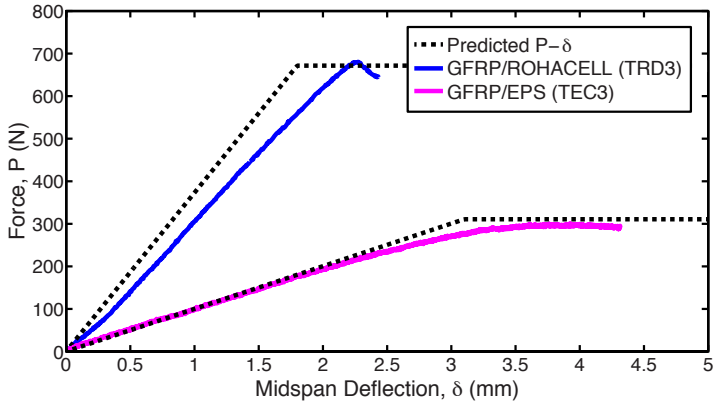

Figure 4.29: Force-displacement curves from simply supported three point bending tests, failing by indentation - results from TRD3 and TEC4

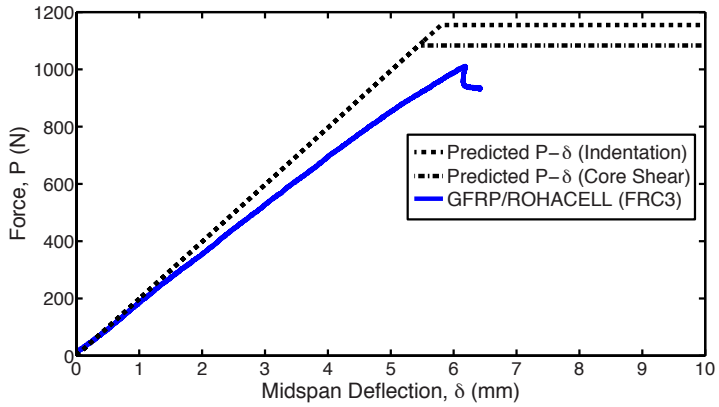

Figure 4.30: Force-displacement curves from simply supported four point bending tests, failing by indentation - results from FRC3

For both core materials, drop-off in load-carrying capacity is associated with an observed plastic collapse of the core. Though multiple occurrences of indentation failure are observed during three point bending tests, only one indentation failure is observed for four point bending: FRC3. Though FRC3 was predicted to fail by core shear, the difference between failure core shear and indentation failure loads is $\sim 2\%$. As the difference between failure load predictions are relatively small, it is shown that the active failure mechanism becomes increasingly harder to predict as beam are designed closet to or along failure region boundary lines.

Figure 4.31 compares indentation failure between three and four point bending tests in terms of force-core indentation curves.

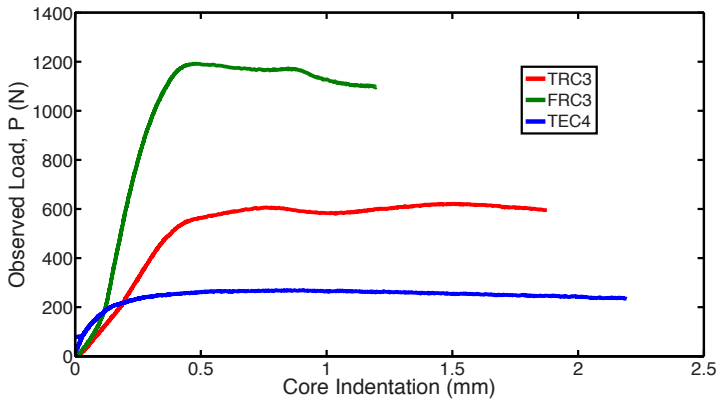

Figure 4.31 Force-core indentation curve plots - TRC4, TEC4 and FRC3 failing by indentation

From the above plots, core indentation results for long beams are compared (320mm$\leq$L$\leq$440). Similar to results shown in core compression tests, both ROHACELL 51-IG and EPS core plastically collapse at a critical plateau stress.

In summary, core indentation is observed as a drop-off in load-carrying capacity, associated with the plastic collapse of the core. Though two different polymer cores are tests, both exhibit a plateau stresses in compressive testing, thus, experiments are well-predicted using the derived expressions for three and four point bending cases.

4.6.3 Microbuckling

Figure 4.32 compares force-axial strain plots for GFRP/ROHACELL 51-IG and GFRP/EPS beams respectively.

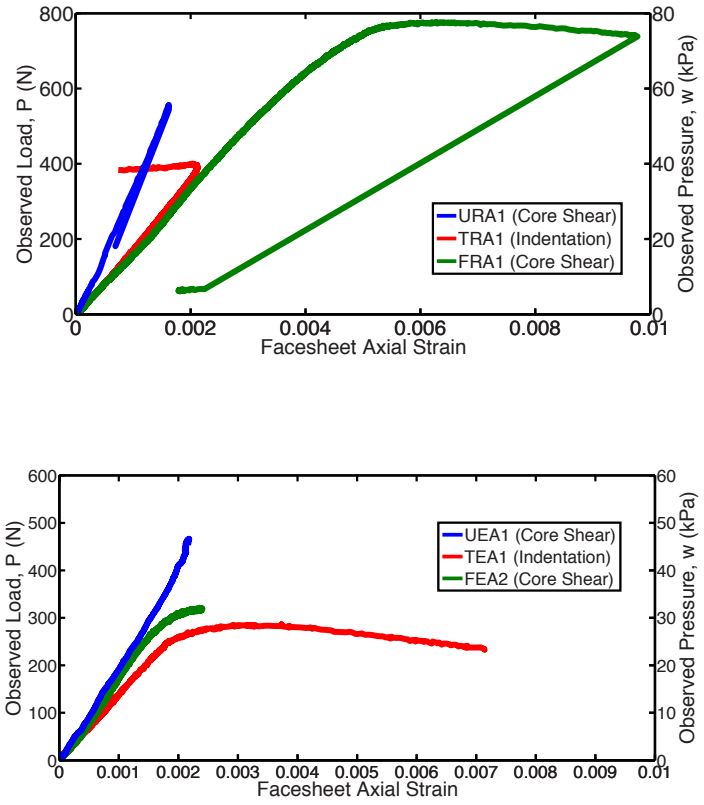

Figure 4.32: Force-face sheet axial strain plots for GFRP/ROHACELL 51-IG beams - FRA1 and URA1 failing by core shear, TRA1 failing by indentation (top), TEA2, FEA2 and UEA1 failing by core shear (bottom)

Though microbuckling does not occur in any test, it is still worth noting the effect of the face sheet in response core shear and indentation failures. In comparing several test results, face sheet axial strain does not exceed 1.7% strain in any test, as it assumed compressive and tensile failure strains are relatively similar in size [9]. After core shear failure for ROHACELL beams, the observed recovery in axial strain is instantaneous, while for EPS core shear, face sheet axial strain continues to increase until the test is stopped. For indentation failure, the formation of a localized indentation region results in a decrease in compressive strain for TRA1. For TEA1 and FRA1, rapid progression in axial strain is noted just prior to their respective indentation and core shear failures. As the predicted microbuckling failure for TEA1 and FRA1 are both well beyond the observed failure load, the rise in axial strain is presumed to be an aftereffect of beams sliding, whereby the increase in beam length momentarily increases the compressive stress on the face sheet before failure occurs.

4.6.4 Adhesion Failure

During experiments, tests from design point FRC4 failed well below the predicted indentation failure load. Though multiple iterations of the same beam design were run, similar results were observed: a localized buckling and separation of the top face sheet from the core at the midspan of the beam. Although adhesion failure was disregarded during the early stages of the study, it is clear a buckling-induced adhesion failure occurred during experiments. For FRC4, the required load for indentation failure is twice that to the three point bending case. As the beam is comprised of the thinnest considered face sheet thickness, any gaps evident between the face and core due to fabrication defects became a critical stress point for delamination, regardless of the adhesive strength considered. Possible reasoning for bond gaps are due to air bubbles being trapped in between the face and core prior to curing. Therefore, as the demand for maximum load capacity increases for beams comprised of thin face sheets, it is important to not only consider a strong adhesive for beam fabrication, but to also ensure a consistent bond exists between the face and core components.

4.6.5 Results Summary - 3D Failure Mechanism Mapping

Using the failure mechanism map as the x-y plane, a three-dimensional visual representation of failure load results are plotted below. As failure mechanism maps are plotted in terms of non-dimensional load and pressure indices in Chapters 2 and 3, results are converted to $\hat{P}$ and $\hat{w}$ respectively. For three point bending tests, Figures 4.33 shows results GFRP/ROHACELL 51-IG beams and Figure 4.34 refers to GFRP/EPS beams. Core shear predictions for EPS including overhang are denoted by squares.

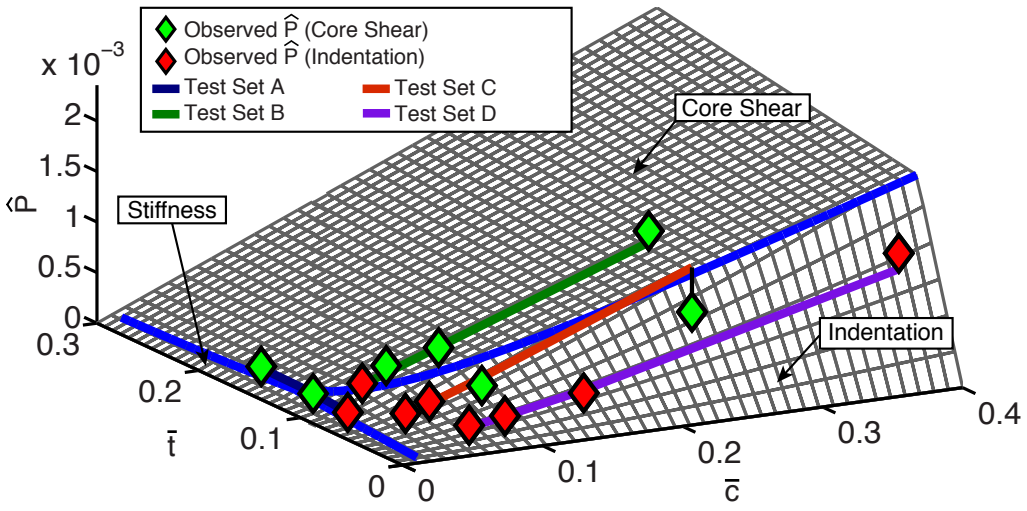

Figure 4.33: Comparison of observed failure load index to analytical predictions for simply supported composite sandwich beams subject to three point bending, represented by a 3D failure mechanism map - GFRP face sheets and ROHACELL 51-IG foam core, $\hat{\delta} = 3.0\%$

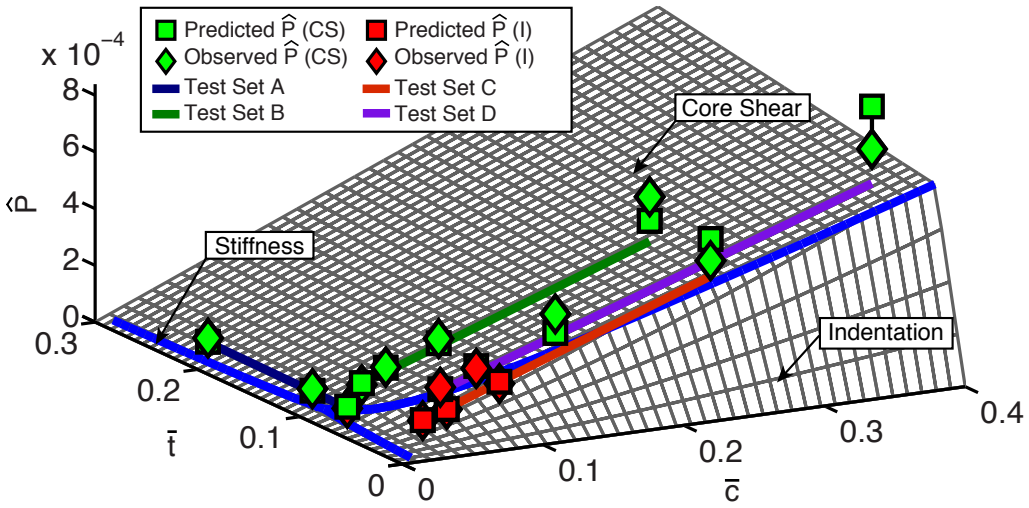

Figure 4.34 Comparison of observed failure load index to analytical predictions for simply supported composite sandwich beams subject to three point bending, represented by a 3D failure mechanism map - GFRP face sheets and extruded polystyrene (EPS) foam core, $\hat{\delta} = 3.0\%$

For both core shear and indentation failures, the most significant errors were observed in all short beam tests. As detailed earlier, short beams experience either core crushing or side support indentation due to a loss of shear force transmitted from the applied load. For both cases, the active failure mechanism cannot be directly identified as a core crush or core indentation as neither achieves the required plastic collapse of the core. Instead, the core is still elastic and merely weakens the beam, preventing it from sustaining the required design load. Though including the overhang factor for EPS beams greatly improves core shear prediction for longer beams, it is difficult to justify it as contributing factor in failure load prediction of short beams due to the observed core crush or side support indentation being the primary factor for failure load prediction error.

For core shear failure load predictions, most tests are well predicted. As mentioned earlier, the stiffening property for thick face sheets improves the under-predictions of GFRP/EPS beams, however as ROHACELL is a more rigid core, the improvement is negligible.

In comparing all indentation failure predictions for three point bending, results show small error margins for all tests with the exception of short beams. As beams expected to fail by indentation comprised of thin face sheets, short beam tests were prone to side support indentation.

Though compliant beams TEA1, TRA1 and TRA2 were noted to under-perform in stiffness due to beam sliding, the corresponding observed failure loads were surprisingly close to their predictions. As core shear is neither dependent on deflection or beam length, failure prediction does not change on account of beam sliding. For indentation failure, it is noted that with a small increase in beam length, the change in predicted failure load is insignificant, so the increase in error is minimal, even after beam sliding.

For four point bending tests, Figure 4.35 plots failure load results for GFRP/ROHACELL 51-IG tests, while Figure 4.36 plots failure load results for GFRP/EPS tests. Similar to the stiffness results, failure load prediction results are in terms of prediction-observed ratios, due to a varied $\bar{c}$ term across the test set.

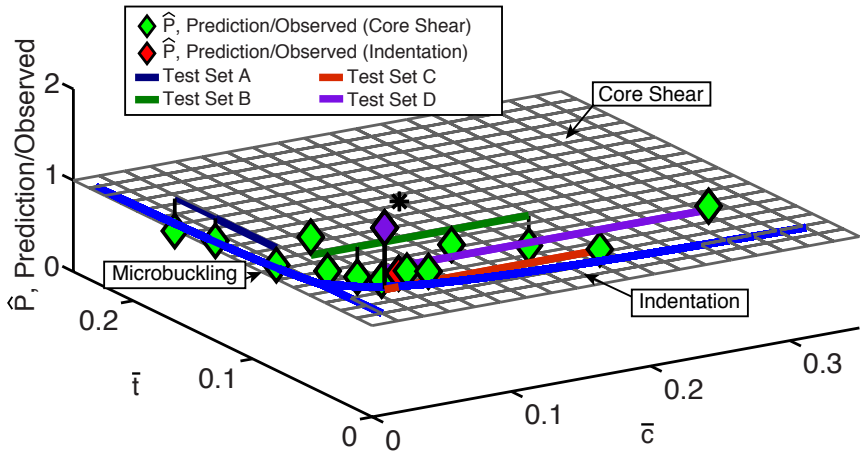

Figure 4.35: Comparison of observed failure load index to analytical predictions for simply supported composite sandwich beams subject to four point bending, represented by a 3D failure mechanism map - GFRP face sheets and ROHACELL 51-IG foam core

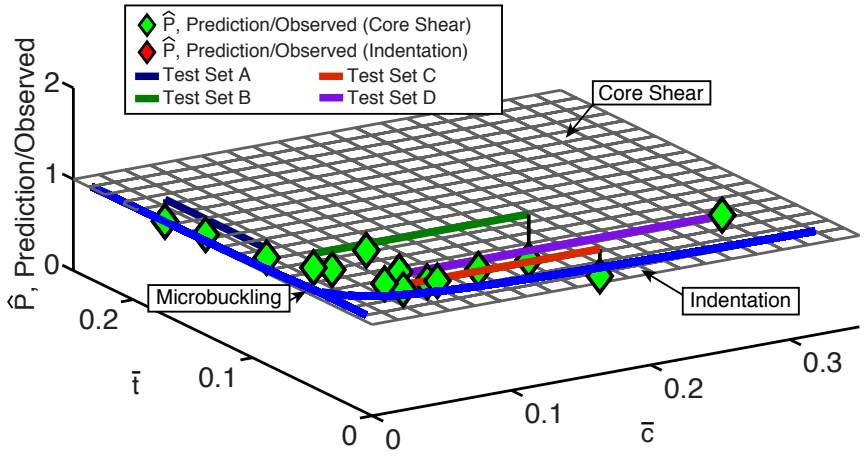

Figure 4.36: Comparison of observed failure load index to analytical predictions for simply supported composite sandwich beams subject to four point bending, represented by a 3D failure mechanism map - GFRP face sheets and extruded polystyrene (EPS) foam core

Comparing four point bending test results in terms of failure load, similar observations are noted from the three point bending case. As most tests failed by core shear, the primary source of prediction error is accounted to not including a thick face sheet stiffening property. Though short beams tests of L=100mm still over-predicted experiment results, the predictions were better than three point bending

tests. Referring to the shear force diagram of four point bending in Figure 3.3, it is presumed that less shear load is lost during four point bending as change in shear load is over in two half steps of $P/2$ as opposed to one full step of P for three point bending.

In addition to each respective failure region, it is also important to note the accuracy of the core shear/indention failure region boundary for both three and four point bending cases. During experiments, three tests predicted to fail by indentation, failed by core shear (TRA2, TRC2 and TEC1) while two core shear tests failed by indentation (TRB4 and FRC3) . Similar to the results of FRC3, the average difference between predicted failures along the core shear/indentation boundary line is small ($< 6\%$), except for short and compliant beam). As prediction error may be accounted from a list of possible test specimen faults to small errors in material strength estimation, the reality of predicting the active failure mechanism becomes increasing difficult as beam designs exist within a failure region boundary line.

For the final set of 3D failure region mechanism maps, Figures 4.37 and 4.38 compare failure pressure index results from the completed uniformly distributed loading tests.

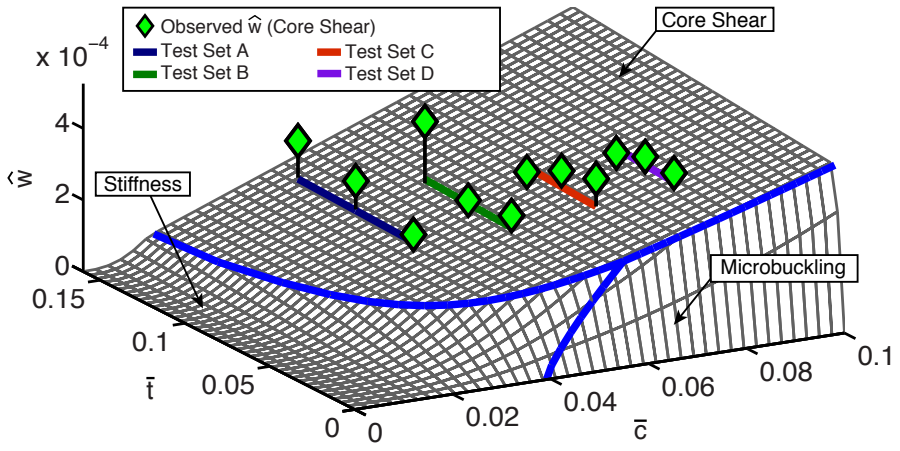

Figure 4.37: Comparison of observed failure pressure index to analytical predictions for simply supported composite sandwich beams subject to uniformly distributed loading, represented by a 3D failure mechanism map - GFRP face sheets and ROHACELL 51-IG foam core, $\hat{\delta} = 3.0\%$

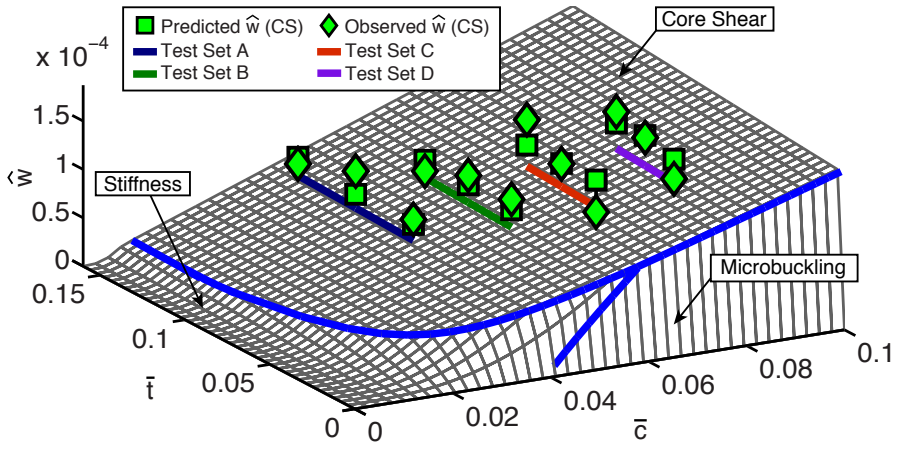

Figure 4.38: Comparison of observed failure pressure index to analytical predictions for simply supported composite sandwich beams subject to uniformly distributed loading, represented by a 3D failure mechanism map - GFRP face sheets and extruded polystyrene (EPS) foam core, $\hat{\delta} = 3.0\%$

For both GFRP/ROHACELL 51-IG and GFRP/EPS tests, results are more sporadic compared to the three and four point bending cases. Though the average error in pressure load prediction is $\sim 13.5\%$ over both material cases, select tests are either over or under-prediction to experiment results by $\sim 20-30\%$.

It is therefore to note the reality of whippletree loading. As the shear force for whippletree loading increases as a stepwise function, as compared to a linear increase for pressure loading shown in Figure 3.15, variations in load simulation may occur. As such, the sporadic performance of the whippletree loading tests may be attributed to the loading fixture itself, not the predictions. The following is especially noted GFRP/ROHACELL tests as a higher pressure index is the required from whippletree loading fixture to attain the same predicted shear load applied by a pressure. However, as GFRP/EPS beams distribute core shear over the entire beam length, the discrepancy in shear load distribution is not evident.

4.7 Summary of Experiments

After conducting the following experiments, stiffness results are shown to be well-predicted for all loading cases, so long as they are not overly compliant or stubby. While the full stiffness equations significantly improved most stiffness predictions for EPS cores, the full stiffness expressions were not required for GFRP/ROHACELL 51-IG beams, as they were already well-predicted.

In regards to strength prediction, Figure 4.39 compares observed load indices to the predicted failure line for core shear, with respect of non-dimensional beam geometry term $(\bar{t}+1)\bar{c}$, peak load index $\hat{P}$ and peak pressure index $\hat{w}$. Each test point is identified by its the respective loading and material case; the predicted failure for EPS with overhang is noted by the dot.

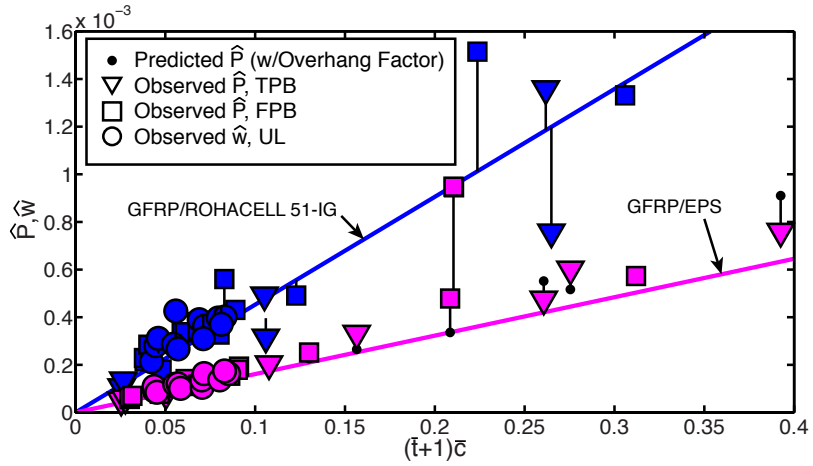

Figure 4.39: Comparison of observed and predicted load index values for core shear failure in terms of non-dimensional beam geometry term related to the core shear failure equation

For thin beams, core shear failure occurs within predicted values. However, as beams comprised of thicker face sheets are tested, error is more significant, but it easily corrected with the addition of a face sheet stiffening property. The difference between EPS and ROHACELL 51-IG results is that beams comprising of EPS cores show a better prediction of failure if a face sheet strengthening term is added. Uniformly distributed loading tests were more sporadic in strength prediction on account of assuming an eight-point load whippletree loading model yields similar results to a pressure load. Though the following statement is true for EPS core (whereby failure is seen across the entire beam length), localized core shear failures are harder to compare as the finer differences between the two models is more apparent.

Figure 4.40 shows all observed indentation failures with respect to the beam geometry term of the indentation failure equation and load index.

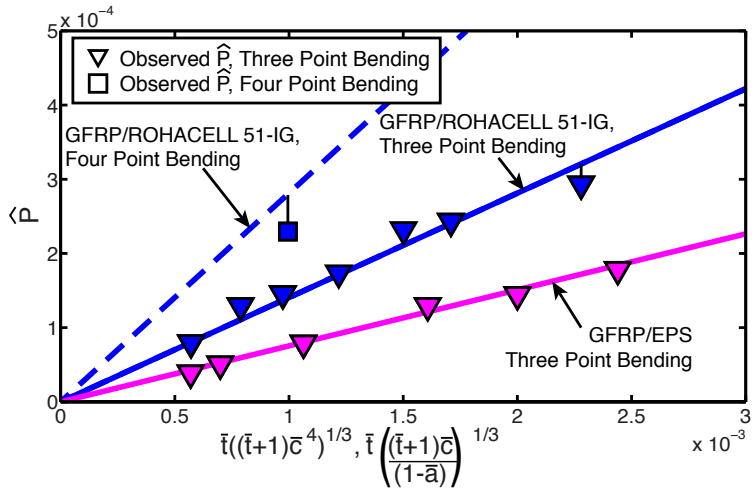

Figure 4.40: Comparison of observed and predicted load index values for indentation failure in terms of non-dimensional beam geometry term related to indentation failure equations

For most cases of indentation failure, predictions are excellent as the ideal beam for indentation failure best satisfy the assumptions made in analytical models: long beams of thin face sheets relative to core thickness. Though failure load error may increases as beams become short or faces become thick, the active failure mechanism is eventually replaced by core shear.

4.7.1 Stiffness Constraint Validation

Throughout the following experiments, a stiffness limit is applied to each loading model; the goal being to avoid testing beams that deflect beyond the limits of the test frame. Of the 84 design points tests, 4 beam designs exceeded $\hat{\delta} = 3\%$: TRA1, TRA2, TRC1, and TEC1. From all tests, the primary reasoning for poor deflection prediction is not based on the derived stiffness expressions, but instead due undesired anomalies that occurred in stubby and compliant beam cases. Though stiffness predictions for simply supported beams become unreliable in beam designs of small $\bar{c}$ due to the potential of sliding, the stiffness constraint is proven to be a valid testing method.

Chapter 5

Conclusion and Future Recommendations

Utilizing previous works in sandwich beam theory, strength and stiffness models for two new load cases are investigated: four point bending and uniformly distributed loading. To validate the new models, an extensive experiment phase is conducted, involving the design, fabrication and testing of 84 different tests, spanning across three different loading cases, comprising of GFRP face sheets and two different core materials. To simulate uniformly distributed loading, a whippletree loading fixture is also introduced.

After comparing analytical predictions to experiment results, it is found that stiffness and strength models both four point bending and uniformly distributed loading are all valid, despite errors that arise for certain beam geometry cases. For short beams, shear force transmitted by the applied load is lost, resulting in side support indentation. As the accompanying deflection does not represent either bending or shear shear effects, stiffness prediction is unreliable. Specific to simply supported beam testing, if beams are designed to be compliant, there is the potential risk of beam sliding; at a given curvature, the applied load simply pushes the beam through the side supports.

Stiffness and strength expressions may be simplified if it face sheet thickness of the considered beam design is small to the core, however, are dependent on the relative face sheet and core material properties. For compliant cores, face sheet thickness must be accounted for most cases of stiffness and strength predictions, as GFRP dominates the overall beam behaviour. As ROHACELL is comparatively a more rigid core, a thicker face sheet must be considered in order to create a similar face sheet-dominant design.

By introducing the stiffness constraint to analytical models, eligible beam designs that were deemed overly compliant were removed from the considered design space. As design space regions were omitted, all beams predicted to fail by microbuckling were removed as well. During experiments, the same stiffness constraint was used to omit beam designs that were projected to deflect beyond the capabilities of the testing area. Of the 84 design points tests that were built around this constraint, only 3 exceeded the set deflection ratio limit. The root cause for these discrepancies was related to the error in predicting stiffness for either compliant or short beams. Although simply supported beams are prone to sliding, the implemented stiffness limit is proven to be a valid testing method.

For uniformly distributed load experiments, a whippletree loading testing fixture is constructed and tested. Though experiments were shown to correlate well with stiffness predictions, noticeable error margins were observed during failure analysis of GFRP/ROHACELL 51-IG beams. As ROHACELL 51-IG core shear occurs within a localized region (as opposed to EPS where shear yielding occurs over the entire beam length), the subtle differences in shear force distribution is more apparent. Beam geometry aside, failure pressure prediction error is well-predicted but sporadic on account of the whippletree loading fixture performing above or below the intended simulated pressure load.

While deriving analytical models for all loading cases, buckling-induced adhesion failure is never considered. However, during four point bending tests, a single design point produced multiple occurrences of buckling-induced adhesion failure. Although beams were constructed with an strong adhesive, the underlying cause for the observed adhesion failure is accounted to flaws in fabrication, whereby air trapped in between the face sheet and core during curing lead to the development of bond gaps. To prevent adhesion failure from occurring, beams are recommend to be fabricated with adhesive of considerable strength compared to the face and core components. Secondly, alternate fabrication techniques are recommended so that the presence of air bubbles between the face and core is prevented (ie. vacuum bagging).

As a final mention, minimum mass trajectories for three point bending, four point bending and uniformly distributed loading are investigated. By comparing the observed mass and load indices from all conducted experiments to the minimum mass trajectories or each respective loading case, it is suggested that only the designs existing on the line may exhibit minimal mass for a given design load.

As stiffness and strength expressions for uniformly distributed loading have been introduced here, further research is recommended for composite sandwich research, including beams comprised metal face sheets and metal foam, truss or honeycomb cores. To perform uniform loading experiments, several modifications are recommended for the whippletree loading fixture design, including a higher number of point load rollers or making the unit fully adjustable for different beam lengths. A final consideration for future research would be to investigate continuous (or fixed-end) composite sandwiches composed of fibre reinforced polymer faces and polymer foam cores. By determining stiffness and strength expressions for continuous beams, composite sandwich panels supported by wireframe structures may be properly analyzed.

In conclusion, by providing new analytical models for stiffness and strength prediction, more complex loading cases may be considered, allowing for failure analysis and mass reduction methods to further improve structural performance.

Bibliography

[1] H Allen. *Analysis and Design of Structural Sandwich Panels*. Oxford: Pergamon Press, first edition, 1969.

[2] MF Ashby, AG Evans, NA Fleck, LJ Gibson, JW Hutchison, and HNG Wadley. *Metal Foams: A Design Guide*. London: Butterworth and Heinemann, 2000.

[3] MF Ashby and PM Weaver. Material limits for shape efficiency. *Progress in Material Science*, 41:61–128, 1997.

[4] BGF. 6oz. Fibreglass Cloth (Style 3733). `http://www.freemansupply.com/6oz.FiberglassClot.htm`, 2001.

[5] B Budiansky. Micromechanics. *Computers and Structures*, 16(1–4):3–12, 1983.

[6] P Casari, D Cartie, and P Davies. Characterisation of Novel K-Cor sandwich structures. *Sandwich Structures 7: Advancing with Sandwich Structures and Materials*, pages 865–874, 2005.

[7] C Chen, A-M Harte, and NA Fleck. The plastic collapse of sandwich beams with a metallic foam core. *International Journal of Mechanical Sciences*, 43:1483–1506, 2001.

[8] S Chiras, D Mumm, A Evans, N Wicks, J Hutchinson, H Dharmasena, H Wadley, and S Fichter. The structural performance of near-optimized truss core panels. *International Journal of Mechanical Sciences*, 39:4093–4115, 2002.

[9] Performance Composites. Mechanical properties of carbon fibre composite materials. `http://www.performance-composites.com/carbonfibre/mechanicalproperties_2.asp`, July 2009.

[10] Owens Corning. *FOAMULAR C-300 Extruded Polystryene Rigid Insulation*, 2010.

[11] AG Evans and JW Hutchinson. On the mechancis of delamination and spalling in compressed films. *International Jounrnal of Solids and Structures*, 20(5):455–466, 1984.

[12] S Faulhaber, C Mercer, M-W Moon, JW Hutchinson, and AG Evans. Buckling delamination in compressed mulitlayers on curved substrates with accompanying ridge cracks. *Journal of the Mechanics and Physics of Solids*, 54:1004–1028, 2006.

[13] EE Gdoutos, IM Daniel, and KA Wang. Indentation failure in composite sandwich structures. *Experimental Mechanics*, 42(4):426–431, 2001.

[14] LJ Gibson and MF Ashby. *Cellular Solids: Structures and Properties*. Cambridge: Cambridge University Press, second edition edition, 1988.

[15] RF Gibson. A simplified analysis of deformations in shear-deformable composite sandwich beams. *Sandwich Structures and Materials*, 13(5):579–588, 2011.

[16] M Hetenyi. *Beams on Elastic Foundation*. Ann Arbor: University of Michigan Press, first edition, 1946.

[17] Hunstman. *Araldite 2011 Epoxy Adhesive - Technical Data Sheet*, 2007.

[18] Huntsman and Renshape Solutions. *Araldite LY 8601 / Aradur 8601 Epoxy Infusion System (Ren-Infusion 8601/Ren 8601)*, 2010.

[19] JW Hutchinson. Delamination of compressed films on curved substrates. *Journal of the Mechanics and Physics of Solids*, 49:1847–1864, 2001.

[20] Evonik Industries. *ROHACELL IG Product Information*, January 2011.

[21] MM Islam and T Aravinthan. Behaviour of fibre composite sandwich panels under uniformly distributed loading. *Incorporating sustainable practice in mechanics of structures and materials*, pages 433–437, 2011.

[22] JW Hutchinson J and Suo. Mixed mode cracking in layered materials. *Advances in Applied Mechanics*, 29:63–191, 1992.

[23] HM Jensen J Clausen and KD Sorensen. Delamination of compressed thin layers at corners. In *International Congress of Theoretical and Applied Mechanics*, 2008.

[24] S Kazemahvazi, D Tanner, and D Zenkert. Corrugated all-composite sandwich structures. part 2: Failure mechanisms and experimental programme. *Composite Science and Technology*, 69:920–925, 2009.

[25] TS Lim, CS Lee, and DG Lee. Failure modes for foam core sandwich beams under static and impact loads. *Journal of Composite Materials*, 38(18):1639–1662, 2004.

[26] D Lukkassen and A Meidell. *Advanced Materials and Structures and their Fabrication Processes*. Narvik University College, manuscript edition, 2007.

[27] S Madhi, AJ Kinloch, FL Matthews, and MA Crisfield. The static mechanical performance of repaired composite sandwich beams: Part I Experimental characterisation. *Journal of Sandiwch Structures and Materials*, 29(5):179–202, 2003.

[28] K Mohan, TH Yip, I Sridhar, and HP Seow. Design of hybrid sandwich panel with aluminum foam core and carbon fiber reinforced face sheets under three point-bending. *Solid State Phenomena*, 111:63–66, 2006.

[29] F Plantema. *Sandwich Construction*. New York: Wiley, 1996.

[30] V Rizov. Non-linear indentation behaviour of foam core sandwich composite materials - a 2d approach. *Computational Materials Science*, 35:107–115, 2006.

[31] V Rizov. Indentation of foam-based polymer composite sandwich beams and panels under static loading. *Journal of Material Engineering and Performance*, 18:351–360, 2009.

[32] M Sadighi, H Pouriayevali, and M Saadati. A study of indentation energy in three points bending of sandwich beams with composite laminate faces and foam core. *World Academy of Science, Engineering and Technology*, 36:214–220, 2007.

[33] SJ Sharp, MF Ashby, and NA Fleck. Material response under static and sliding indentation loads. *Acta Metali*, 41(3):685–692, 1993.

[34] JK Sorensen and H Jensen. Buckling-driven delamination in layered spherical shells. *Journal of the Mechanics and Physics of Solids*, 56:230–240, 2008.

[35] CA Steeves. Optimising sandwich beams for strength and stiffness. To appear in *Journal of Sandwich Structures and Materials*, 2012.

[36] CA Steeves and NA Fleck. Collapse mechanisms of sandwich beams with composite faces and a foam core, loaded in three-point bending, Part I: Analytical models and minimum weight design. *International Journal of Mechanical Sciences*, 46:561–583, 2004.

[37] CA Steeves and NA Fleck. Collapse mechanisms of sandwich beams with composite faces and a foam core, loaded in three-point bending, Part II: Experimental investigation and numerical modelling. *International Journal of Mechanical Sciences*, 46:585–608, 2004.

[38] CA Steeves and NA Fleck. Material selection in sandwich beam construction. *Scripta Materials*, 50:1335–1339, 2004.

[39] VL Tagarielli and NA Fleck. A comparison of the structural response of clamped and simply supported sandwich beams with aluminum faces and metal foam core. *Journal of Applied Mechanics*, 72:408–417, 2005.

[40] MD Thouless. Decohesion of films. *Acta Metali*, 36(12):3131–3135, 1988.

[41] Tokyo Sokki Kenyujo Co. Ltd. (TML). F series leadwire-integrated foil strain gauge. `http://www.tml.jp/e/product/strain_gauge/gauge_list/flead_list.html`.

[42] BS White. Measurement of wood pallet performance subjected to uniform loading in racked, fork tine, and floor stacked support conditions. Master's thesis, Virginia Polytechnic Institute and State University, 2008.

[43] D Zenkert. *An Introduction to Sandwich Construction*. Engineering Material Advisory Services, 1995.